# The Sun and heliosphere explorer - the Interhelioprobe mission

V. D. Kuznetsov, L. M. Zelenyi, I. V. Zimovets, K. Anufreychik, V. Bezrukikh, I. V. Chulkov, A. A. Konovalov, G. A. Kotova, R. A. Kovrazhkin, D. Moiseenko, et al.

## ▶ To cite this version:

V. D. Kuznetsov, L. M. Zelenyi, I. V. Zimovets, K. Anufreychik, V. Bezrukikh, et al.. The Sun and heliosphere explorer - the Interhelioprobe mission. Geomagnetism and Aeronomy, 2016, 56, pp.781-841. 10.1134/S0016793216070124 . hal-03645020

**HAL Id: hal-03645020**
**https://hal.science/hal-03645020v1**

Submitted on 8 Jun 2022

# The Sun and Heliosphere Explorer – The Interhelioprobe Mission[1]

V. D. Kuznetsov[a], L. M. Zelenyi[b], I. V. Zimovets[b, *], K. Anufreychik[b], V. Bezrukikh[b], I. V. Chulkov[b], A. A. Konovalov[b], G. A. Kotova[b], R. A. Kovrazhkin[b], D. Moiseenko[b], A. A. Petrukovich[b], A. Remizov[b, †], A. Shestakov[b], A. Skalsky[b], O. L. Vaisberg[b], M. I. Verigin[b], R. N. Zhuravlev[b], S. E. Andreevskyi[a], V. S. Dokukin[a], V. V. Fomichev[a], N. I. Lebedev[a], V. N. Obridko[a], V. P. Polyanskyi[a], V. A. Styazhkin[a], E. A. Rudenchik[a, †], V. M. Sinelnikov[a], Yu. D. Zhugzhda[a], A. P. Ryzhenko[c], A. V. Ivanov[c], A. V. Simonov[c], V. S. Dobrovolskyi[c], M. S. Konstantinov[d], S. V. Kuzin[e], S. A. Bogachev[e], A. A. Kholodilov[e], A. S. Kirichenko[e], E. N. Lavrentiev[e], A. A. Pertsov[e], A. A. Reva[e], S. V. Shestov[e], A. S. Ulyanov[e], M. I. Panasyuk[f], A. F. Iyudin[f], S. I. Svertilov[f, g], V. V. Bogomolov[g], V. I. Galkin[g], B. V. Marjin[g], O. V. Morozov[g], V. I. Osedlo[g], I. A. Rubinshtein[g], B. Ya. Scherbovsky[g, †], V. I. Tulupov[g], Yu. D. Kotov[g], V. N. Yurov[h], A. S. Glyanenko[h], A. V. Kochemasov[h], E. E. Lupar[h], I. V. Rubtsov[h], Yu. A. Trofimov[h], V. G. Tyshkevich[h], S. E. Ulin[h], A. S. Novikov[h], V. V. Dmitrenko[h], V. M. Grachev[h], V. N. Stekhanov[h], K. F. Vlasik[h], Z. M. Uteshev[h], I. V. Chernysheva[h], A. E. Shustov[h], D. V. Petrenko[h], R. L. Aptekar[i], V. A. Dergachev[i], S. V. Golenetskii[i], K. S. Gribovskyi[i], D. D. Frederiks[i], E. M. Kruglov[i], V. P. Lazutkov[i], V. V. Levedev[i], F. P. Oleinik[i], V. D. Palshin[i], A. I. Repin[i], M. I. Savchenko[i], D. V. Skorodumov[i], D. S. Svinkin[i], A. S. Tsvetkova[i], M. V. Ulanov[i], I. E. Kozhevatov[j], J. Sylwester[k], M. Siarkowski[k], J. Bąkała[k], Ż. Szaforz[k], M. Kowaliński[k], O. V. Dudnik[l], B. Lavraud[m], F. Hruška[n], I. Kolmasova[n], O. Santolik[n], J. Šimůnek[n], V. Truhlík[n], H.-U. Auster[o], M. Hilchenbach[p], Yu. Venedictov[q], and G. Berghofer[r]

[a] *Pushkov Institute of Terrestrial Magnetism, Ionosphere and Radio Wave Propagation of the Russian Academy of Sciences (IZMIRAN), Troitsk, Moscow, 142190 Russia*

[b] *Space Research Institute (IKI), Russian Academy of Sciences, Profsoyuznaya ul. 84/32, Moscow, 117997 Russia*

[c] *Lavochkin Association, Leningradskaya ul. 24, Khimki, Moscow oblast, 141400 Russia*

[d] *Research Institute of Applied Mechanics and Electrodynamics (RIAME), Moscow Aviation Institute (National Research University), Leningradskoe sh. 5, Moscow, 125993 Russia*

[e] *Lebedev Physical Institute (LPI) of the Russian Academy of Sciences, Leninskii pr. 53, Moscow, 119991 Russia*

[f] *Skobeltsyn Institute of Nuclear Physics, Moscow State University (SINP MSU), Moscow, 119991 Russia*

[g] *Faculty of Physics, Moscow State University, Moscow, 119991 Russia*

[h] *National Research Nuclear University (NRNU) "MEPhI" (Moscow Engineering Physics Institute), Kashirskoe sh. 31, Moscow, 115409 Russia*

[i] *Ioffe Physical Technical Institute (IPTI) of the Russian Academy of Sciences, Politechnicheskaya ul. 26, St. Petersburg, 194021 Russia*

[j] *Radiophysical Research Institute (NIRFI), Bolshaya Pecherskaya ul. 25/12a, Nizhny Novgorod, 603950 Russia*

[k] *Space Research Centre, Polish Academy of Sciences, Solar Physics Division (CBK PAN ZFS), ul. Kopernika 11, Wroclaw, 51-622 Poland*

[l] *Institute of Radio Astronomy, National Academy of Sciences of Ukraine (IRA NASU), Chervonopraporna Str. 4, Kharkiv, 61002 Ukraine*

[m] *Institute de Recherche en Astrophysique et Planetologie (IRAP), 9 avenue du Colonel Roche, BP 44346, Toulouse Cedex 4, 31028 France*

[n] *Institute of Atmosheric Physics (IAP), Academy of Sciences of the Czech Republic, Bocni II 1401, Prague, 14131 Czech Republic*

[o] *Institute for Geophysics and Extraterrrestrial Physics (IGEP), Techische Universitat Braunschweig (TUB), Mendelssohnstr. 3, Braunschweig, D-38106 Germany*

[p] *Max Planck Institute for Solar System Research (MPS), Justus-von-Liebig-Weg 3, Göttingen, 37077 Germany*

[q] *Odessa National Polytechnic University (ONPU), Tarasa Shevchenka Pr. 1, Odessa, 65000 Ukraine*

[r] *Space Research Institute (IWF), Austrian Academy of Sciences, Schmiedlstrasse 6, Graz, 8042 Austria*

**e-mail: ivanzim@iki.rssi.ru*

**Abstract**—The Interhelioprobe mission aims to investigate the inner heliosphere and the Sun from close distances (up to 0.3 AU) and from out of the ecliptic plane (up to 30°). In this paper we present the relevance of the mission and its main scientific objectives, describe the scientific payload, ballistic scenario and orbits of the spacecraft. Possibilities of scientific cooperation with other solar and heliospheric space missions are also mentioned.

*Keywords:* Sun, heliosphere, Interhelioprobe space mission, solar physics, heliospheric physics, solar-terrestrial relations

**DOI:** 10.1134/S0016793216070124

## 1. INTRODUCTION

The heliosphere is filled with radiation, plasma and magnetic field flowing from the Sun. They permanently influence interplanetary space, magnetospheres and atmospheres of the planets. However, since the Sun is a magnetically active star, this influence is not constant. It changes with characteristic period of approximately 11 years. In general, we already understand the structure of the Sun and how it works. Due to its proximity to the Earth, the Sun is the most studied astrophysical object in the sky. It plays the role of a natural laboratory for investigation of plasma processes and serves as a "litmus paper" in testing theories and models of stellar activity.

The Sun is comprehensively studied by the ground based and space based observatories and instrumentations. Over the past half century, starting from the beginning of the "space age", there were a lot of space projects, which helped to collect a large amount of important information about our nearest star. Among them are: SOLRAD, IMP, PROGNOZ, Skylab, Helios, GOES, SMM, Hinotori, Ulysses, Yohkoh, CORONAS-I, WIND, INTERBALL, SOHO, ACE, TRACE, CORONAS-F, RHESSI, STEREO, Hinode, CORONAS-PHOTON, PROBA-2, SDO, IRIS. However, despite the great contributions of these numerous missions to our knowledge of the Sun and its nearest space environment, many important and interesting problems in solar and heliospheric physics remain unsolved yet. In particular, we do not yet understand in details mechanisms of the solar dynamo and solar cycle, heating of the solar corona and formation of the solar wind, acceleration of charged particles to high (relativistic) energies and their transport in the heliosphere, triggering of the most powerful phenomena of the solar activity such as flares and coronal mass ejections (CMEs). These and many other problems of solar physics is of general astrophysical interest, since analogous phenomena take place in distant stars, while the detailed study of these problems is only possible on our parent star – the Sun. Practical interest in studying these problems is related to the strong impact of the Sun to the Earth, where we live, and to the near Earth and interplanetary space, where our presence is increasingly enhancing.

To achieve further progress in understanding the solar activity and solar-terrestrial relations the next generation of solar-heliospheric space missions is required (see, for example, (Kuznetsov, 2015)). One of the most promising routes of progress is to organically combine remote sensing observations of the Sun with high angular and spectral resolution in different wavelength ranges and local measurements in the interplanetary space at small heliocentric distances and out of the ecliptic plane. The synergy between remote sensing observations and local measurements onboard the same spacecraft placed at vantage points in the inner heliosphere, which were never achieved before, will definitely allow to obtain new important scientific information.

Currently, two such space missions are in preparation. The first one is the Solar Orbiter – a medium-class mission developed by ESA with participation of NASA (e.g., (Mueller et al., 2013)). The second one is the Interhelioprobe – a mission sponsored by the Russian Federal Space Agency. Both these missions are successors of the Interhelios mission proposed in the nineties of the last century (e.g., (Oraevsky et al., 2001); and references therein). Our paper aims to summarize scientific objectives of the Interhelioprobe mission, to describe its scientific payload, and to give some up-to-date information about the ballistic scenario and orbits. The brief summary of the mission is given in Table 1.

## 2. GENERAL CONCEPT OF THE MISSION

To achieve progress in understanding solar and heliospheric physics we need to make new more precise observations of the Sun and to conduct new experiments in the regions of the inner heliosphere that have never been achieved before. The inner heliosphere (up to 0.3 AU) was already visited by the Helios 1 and 2 spacecraft (1974–1985). These space trips gave a lot of useful information (e.g., (Schwenn and Marsch, 1990, 1991)). However, the spacecraft orbits were restricted by the ecliptic plane. Another shortage of that, surely outstanding, mission was a lack of telescopes with spatial resolution for remote sense observations of the solar atmosphere. The spacecraft were

---

[1] The article is published in the original.

[†] Deceased.

**Table 1.** Brief summary of the Interhelioprobe mission

| | |
|---|---|
| Funding | Russian Federal Space Agency (Roscosmos) |
| Leading scientific organization | Space Research Institute (IKI) of Russian Academy of Sciences |
| Principal Investigators | L.M. Zeleny (IKI), V.D. Kuznetsov (IZMIRAN) |
| General Concept | —Multi-wavelength solar observations at short distances from the Sun (up to $60R_S$)<br>—Out-of-ecliptic solar observations (up to 30°) and observations of the Sun's opposite side<br>—In situ measurements in the inner heliosphere (and) out of the ecliptic plane |
| Main scientific objectives | —Solar dynamo and solar cycle<br>—Thin structure and dynamics of solar atmosphere<br>—Corona heating and acceleration of solar wind<br>—Solar flares, coronal mass ejections (CMEs)<br>—Acceleration and transport of solar cosmic rays in the corona and inner heliosphere<br>—Solar-terrestrial relations and space weather |
| Spacecraft design | Lavochkin Association, Russia |
| Number of Spacecraft | 2 |
| Spacecraft | 3-axis stabilized platform, circle-shaped shield with windows, sizes $3.7 \times 5.2 \times 3.7$ m$^3$ |
| Orientation | Sun-pointing |
| Launcher | "Soyuz-2/1b" rocket with "Fregat" upper stage |
| Cosmodrome | Baikonur, Republic of Kazakhstan |
| Launch date | 2026–2027 |
| Orbit | Heliocentric, elliptical, Venus-resonance orbits with multiple gravity assists, perihelion 60–70 $R_S$, aphelion 250–260 $R_S$, inclination up to 30° to the ecliptic |
| Mission active operation time | 5 years |
| Total mass of scientific payload | 160 kg |
| Scientific payload | 10 instruments for remote sense observations + 9 instruments for local measurements = 19 instruments totally |
| Cooperation in scientific payload development | Russia, Poland, France, Czech Republic, Austria, Germany, Ukraine, UK |
| Flight Operation Center | Lavochkin Association, Russia |
| Ballistic Operation Center | Keldysh Institute of Applied Mathematics, Moscow, Russia |
| Science Operation Center | IKI, Moscow, Russia |
| Ground stations | "Medvezgyi Ozera" (64-m antenna), Moscow Region, Russia<br>"Ussuriysk" (70-m antenna), Primorsky Krai, Russia |
| Scientific traffic | Up to 1 Mbit/s, 1 GB/day |
| Telemetry band | X-band |

equipped with instrumentations suitable for in situ measurements only. The out-of-ecliptic regions of the heliosphere were later visited by Ulysses (1990–2009). However, Ulysses did not approach the Sun closer than at 1 AU, and as Helios, Ulysses, unfortunately, did not have any telescopes to observe the Sun and to investigate spatial structure of its atmosphere. There were no other solar missions after Helios and Ulysses that would visited the very inner heliosphere and left the ecliptic plane. All other solar missions observed the Sun and/or made in situ measurements at around 1 AU in the ecliptic.

The major concept of the Interhelioprobe mission is to perform:

- detailed multi-wavelength solar observations with high spatial resolution at small distances from the Sun (up to 0.3 AU);
- out-of-ecliptic solar observations (up to 30°) and observations of the Sun's opposite side, which is not visible from the Earth at a given time;

- in situ measurements in the inner heliosphere (and) out of the ecliptic plane of electric and magnetic fields, and particles onboard the same spacecraft.

Proximity to the Sun will enable imaging of the solar atmosphere with spatial resolution improved with respect to the resolution available at 1 AU. Out-of-ecliptic observations of the Sun from small heliocentric distances will allow to investigate solar polar regions in details. Changing of the spacecraft position with respect to the Sun-Earth line will allow stereoscopic observations of the solar atmosphere, flare sources and CMEs, if observations of Interhelioprobe will be coordinated with the Earth-orbit and ground-based observations. Observations of the solar side, which is invisible from the Earth, will allow to better imagine three-dimensional structure of the solar magnetic field and the solar atmosphere. Precision local measurements in the inner heliosphere (within 1 AU) in and out of the ecliptic plane will allow to obtain new detailed information, in particular, about physical processes in the slow and fast solar wind, about interplanetary CMEs, magnetic bubbles, shock waves, corotation interaction regions (CIRs) and other agents of the "space weather", about acceleration and propagation of high energy charged particles (solar cosmic rays). The scientific value of such observations and measurements, if made together onboard a single spacecraft, will be increased in comparison with the same measurements and observations made separately within the frames of different projects, in different places and times.

## 3. SCIENTIFIC GOALS AND TASKS OF THE MISSION

The general concepts and ballistics scenarios of the Interhelioprobe and Solar Orbiter missions are similar due to historical reasons. Therefore, their scientific objectives and spectra of scientific tasks, in general, are also similar. Since the major objectives of Solar Orbiter are already well described in details by Mueller et al. (2013), here we just briefly summarize the goals and corresponding main tasks of the Interhelioprobe mission.

*The goal I is to contribute to understanding of the solar dynamo mechanisms and solar cycle.*

Corresponding tasks are:

- to investigate structure of magnetic field in the solar polar regions,
- to investigate meridional flows and magnetic field transport to the solar poles,
- to measure the solar constant and its variations at different heliolatitudes.

*The goal II is to better imagine fine structure and dynamics of the solar atmosphere.*

Corresponding tasks are:

- to investigate fine magnetic and plasma structures at the photosphere and in the solar atmosphere at various heliolatitudes,
- to study their dynamics and role in formation of the solar atmosphere and initiation of energy release at small scales.

*The goal III is to achieve progress in finding mechanisms of solar corona heating and acceleration of the solar wind.*

Corresponding tasks are:

- to investigate energy release processes at different scales and their role in heating of the solar corona and acceleration of the solar wind,
- to investigate wave and turbulent processes in the solar wind, their role in acceleration of the solar wind,
- to investigate properties of the solar wind at different heliographic latitudes and distances,
- to investigate structure of the heliospheric magnetic field.

*The goal IV is further understanding of the nature and global dynamics of the most powerful manifestations of the solar activity – solar flares and CMEs – and their influence on the heliosphere and "space weather".*

Corresponding tasks are:

- to investigate trigger mechanisms of solar flares and CMEs,
- to investigate links between flares and CMEs,
- to investigate effects of solar flares and CMEs on the inner and outer corona, and the heliosphere (magnetic clouds, shock waves),
- to investigate heliolongitude and heliolatitude spread and dynamics of CMEs.

*The goal V is to better recognize processes of generation and transport of energetic particles (solar cosmic rays) at the Sun and in the heliosphere.*

Corresponding tasks are:

- to investigate acceleration processes of charged particles and processes of generation of neutrons, hard X-ray and gamma-ray emission in solar flares,
- to investigate acceleration processes of charged particles related with the formation and propagation of CMEs,
- to investigate relations between active processes at the Sun and energetic particles in the inner heliosphere,
- to study transport processes of energetic charged particles in the corona and inner heliosphere.

## 4. BALLISTIC SCENARIO OF THE MISSION

### *4.1. Variant with One Spacecraft*

Flight to the inner region of Solar System with approach to Sun at 60–70 solar radii (0.28–0.33 AU) requires huge energy costs. Direct flight from Earth to this space region requires asymptotic spacecraft speed of around 10.5 km/s, while only 3 km/s is enough for a flight to Mars or Venus, and 6 km/s – to Jupiter. Due to this reason a long-lasting flight scheme with the return to Earth and gravity assist maneuver in its gravitational field, as well as with subsequent multiple gravity assist maneuvers with Venus is chosen for the Interhelioprobe mission. Moreover, an additional work of the spacecraft Electric Propulsion System (see Section 5) with reserve of characteristic speed of around 4.5 km/s is required on the Earth-Earth part of the flight.

Scheme of the Interhelioprobe spacecraft (SC) flight includes the main following phases:

1. injection of the spacecraft to the parking orbit with the use of "Soyuz-2/1b" rocket and "Fregat" Upper Stage, finishing by the spacecraft separation;

2. Earth-Earth heliocentric flight with the use of the Electric Propulsion System;

3. gravity assist maneuver with Earth;

4. Earth-Venus heliocentric flight;

5. sequence of passive gravity assist maneuvers with Venus, each resulting in access to orbits with reduced radius of perihelion or increased inclination to the ecliptic.

Each passive part of the phases 4 and 5 can require one or two corrections of the spacecraft trajectory.

The Electric Propulsion System will be used only during the Earth-Earth phase to increase asymptotic speed of spacecraft approaching to Earth and subsequent departure to Venus. The Electric Propulsion System will not be used for formation of the spacecraft orbit after the gravity assist maneuver with Earth, although the System can be used sometimes during the subsequent phases for duplication of the Orientation and Stabilization System work on trajectory correction.

Earth-Earth part of the flight (phases 1–2), when the spacecraft orbit lies almost in the ecliptic plane, is called the ecliptic phase. It is designed for formation of the heliocentric trajectory, which will allow to approach Venus, after the gravity assist maneuver with Earth, with the asymptotic speed sufficient to subsequent formation of the working orbits with small perihelion radius (of 60–70 solar radii) or with relatively high inclination to the ecliptic plane.

Orbit with the smallest perihelion radius is realized already after the second gravity assist maneuver with Venus. Subsequent gravity assist maneuvers with Venus are intended to increase the orbit inclination to the ecliptic plane. However, the perihelion radius will also increase during these maneuvers without additional energy costs. The liquid propulsion engines of the Orientation and Stabilization System are nominally have small energetic and will be used only for trajectory correction and also for the spacecraft attitude control (for unloading of the angular momentum of the governing flywheels).

To realize the series of subsequent gravity assist maneuvers with Venus the spacecraft has to be placed each time on heliocentric orbit with orbital resonance $k : m$ with the planet. This means that the spacecraft makes $k$ revolutions around Sun on such orbit for the time, which is required for Venus to make $m$ revolutions around Sun (orbital period of Venus is around 224.7 earth days). Minimization of the spacecraft injection to high heliolatitudes requires orbital resonances of low order. The orbital resonances 1 : 1 and 4 : 3 are selected. The subsequent gravity assist maneuvers are used to shift the spacecraft orbit from one resonance to another in order to change perihelion radius or inclination to the ecliptic. As a result of the latest gravity assist maneuver with Venus the spacecraft is shifted to the non-resonant heliocentric orbit with maximal possible inclination to the ecliptic.

The spacecraft launch windows are repeated in the Venus synodic period, which is around 1.6 year. Below we present characteristics of an example spacecraft orbit, which are calculated for the launch on 18 April 2022. Characteristics of the spacecraft orbit for the later launch windows should be similar to the presented one. General view of the spacecraft trajectory is shown in Fig. 1. Main characteristics of the spacecraft flight are summarized in Table 2.

Figure 2 shows graphics of the Sun-Interhelioprobe-Earth and Sun-Earth-Interhelioprobe angles during the flight. It can be seen that both angles change within 0°–180° range during the ecliptic phase of the flight (until 474 days). The Sun-Interhelioprobe-Earth angle reaches 170° during the out-of-ecliptic phase of the flight, however the Sun-Earth-Interhelioprobe angle is not larger than 75° during this phase.

Figure 3 shows distances from the Interhelioprobe spacecraft to Sun and Earth during the flight. Distance to Sun is within $50–180 \times 10^6$ km (0.33–1.20 AU) range. Maximal distance to Earth is around $130 \times 10^6$ km (0.87 AU) during the ecliptic phase of the flight and reaches almost $300 \times 10^6$ km (2.01 AU) in the out-of-ecliptic phase.

Figure 4 shows projection of the Interhelioprobe spacecraft trajectory to the ecliptic plane during the heliocentric Earth-Earth-Venus phase of the orbit. Dark grey circle E0 is the Earth position during the launch of the spacecraft. Dark grey rhomb E1 is the Earth position during the spacecraft gravity assist maneuver with it. Light grey circle V1 is the Venus position during the spacecraft first gravity assist maneuver with it. Dark and light grey dots are the Earth and Venus orbits respectively. Grey arrows show directions of the Electric Propulsion System thrust during its active phase.

Spatial view of the Earth-Earth-Venus part of the spacecraft flight is shown in Fig. 5. The scale of the Z-axis is increased.

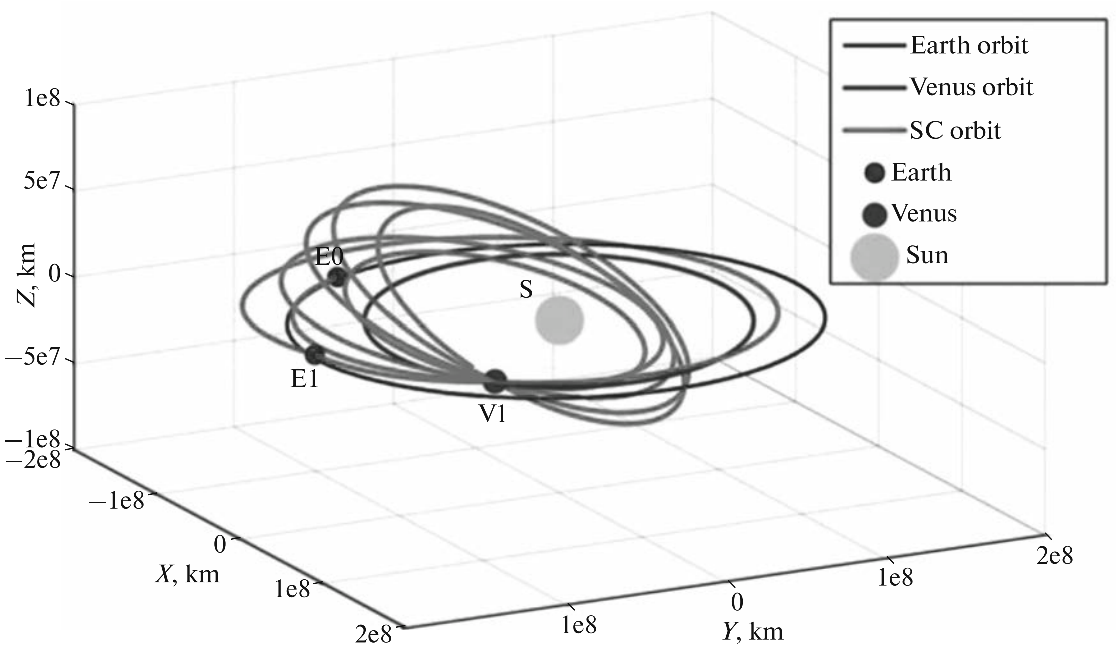

**Fig. 1.** Spatial view of an example Interhelioprobe spacecraft trajectory.

### *4.2. Variant with Two Spacecraft*

In the end of 2015 it was decided that the Interhelioprobe mission will have two identical spacecraft with the same sets of scientific payload. Two spacecraft will allow continuous out-of-ecliptic observations and measurements, greatly extend the possibility of solving scientific tasks, increase the overall reliability of the mission, and preserve uniqueness of the mission with respect to the Solar Orbiter mission, which will be launched earlier but with a single spacecraft. The main idea is to have always one spacecraft out of the ecliptic plane. The orbit of the spacecraft-1 (SC-1) will be the same as described in the previous subsection 4.1. The launch windows of the SC-2 will be, most probably, delayed by about 4 months with respect to the launch windows of the SC-1. In general, the orbit of the SC-2 will be similar to the orbit of the SC-1. There will be the Earth-Earth-Venus part of the orbit (Fig. 6) and a series of gravity assist maneuvers with the Venus as well (Table 3). Heliocentric distances and heliographic latitudes of the SC-1 and SC-2 are shown in dynamics in Fig. 7. The information is given for the SC-2 launch date on 24 August 2022. The Earth-Earth-Venus part of the SC-2 orbit will last for 1.36 years.

## 5. SPACECRAFT

The Interhelioprobe spacecraft (SC) is designed and constructed by the Lavochkin Research and Production Association (Khimki, Moscow Region, Russia). The SC is a three-axis stabilized platform oriented to

**Table 2.** Main characteristics of an example Interhelioprobe flight

| Characteristic, dimension | Value |
|---|---|
| Launch date | 18 April 2022 |
| Asymptotic speed of departure from Earth, km/sec | 1.950 |
| Duration of the Electric Propulsion System work, hours (days) | 7434 (309.74) |
| Duration of the Earth-Earth flight phase, years (days) | 1.18 (429) |
| Asymptotic speed of approach to Earth and departure from it, km/sec | 9.225 |
| Asymptotic speed of approach to Venus, km/sec | 17.500 |
| Sequence of orbital resonances with Venus after each maneuver | 1 : 1, 4 : 3, 1 : 1, 1 : 1 |
| Minimal perihelion radius, solar radii | 66.4 |
| Maximal inclination to the ecliptic, deg | 30.5 |
| Flight duration from the launch to the last gravity maneuver, years (days) | 5.04 (1826) |

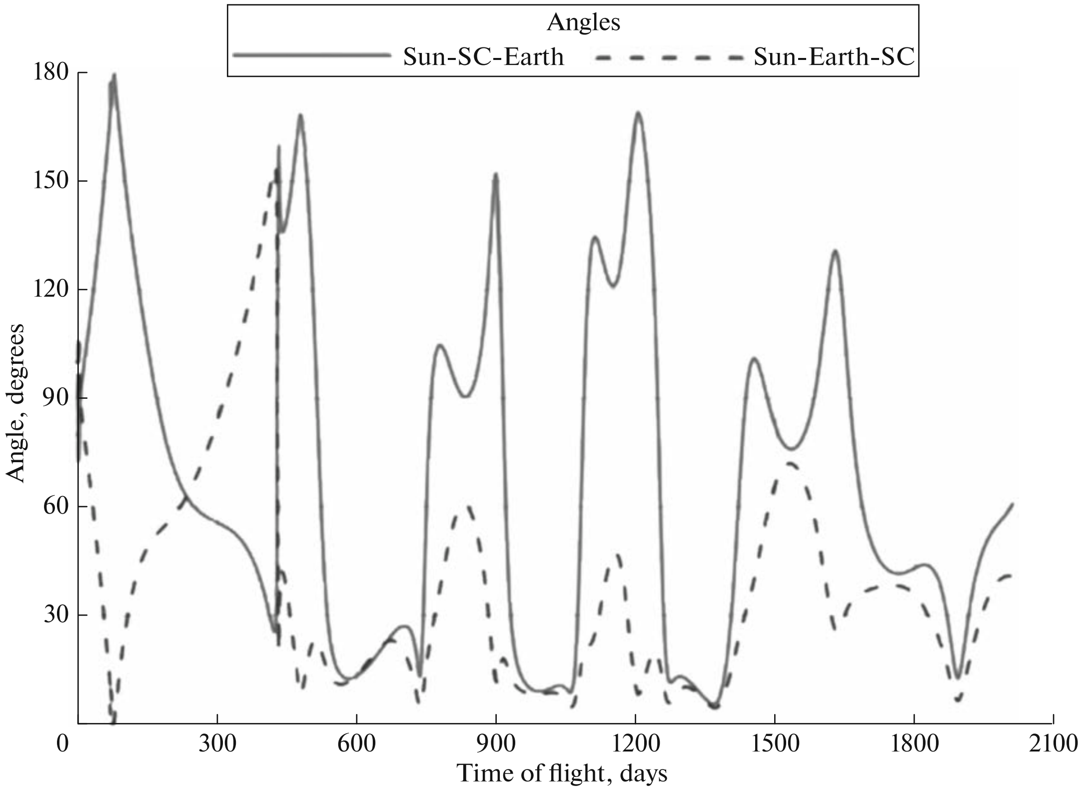

**Fig. 2.** Sun-Interhelioprobe-Earth (solid curve) and Sun-Earth-Interhelioprobe (dashed curve) angles during the Interhelioprobe spacecraft flight.

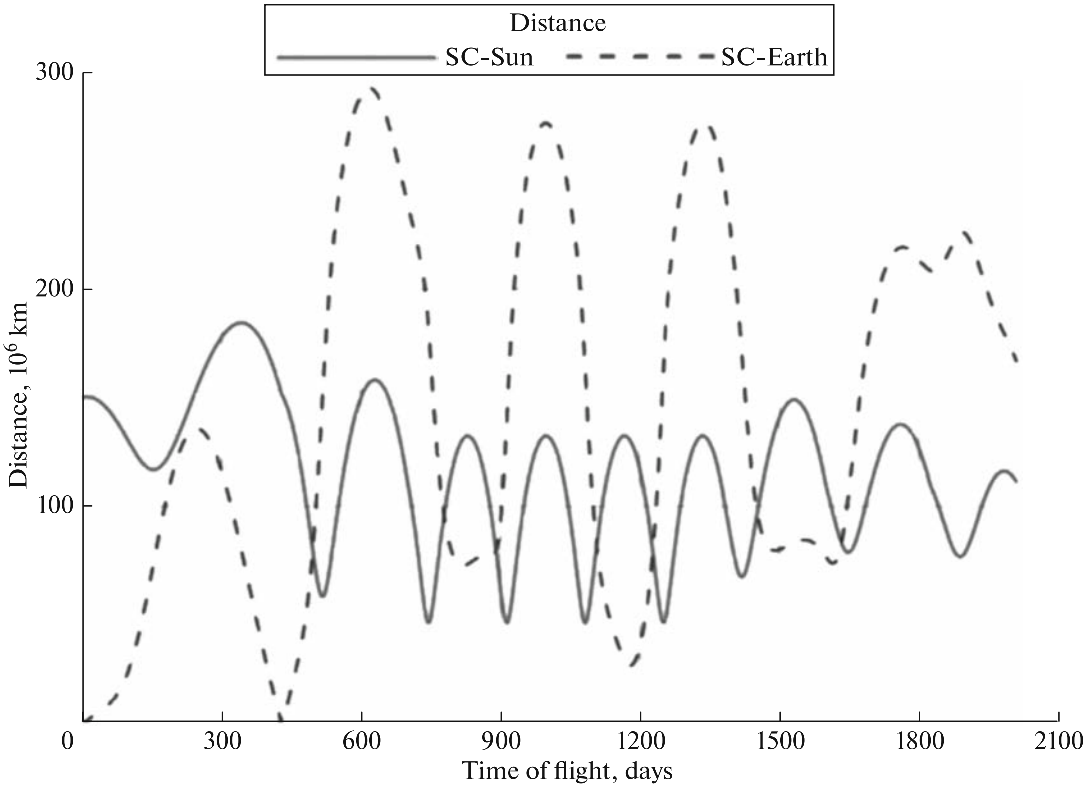

**Fig. 3.** Distances from the Interhelioprobe spacecraft to Sun (solid curve) and Earth (dashed curve).

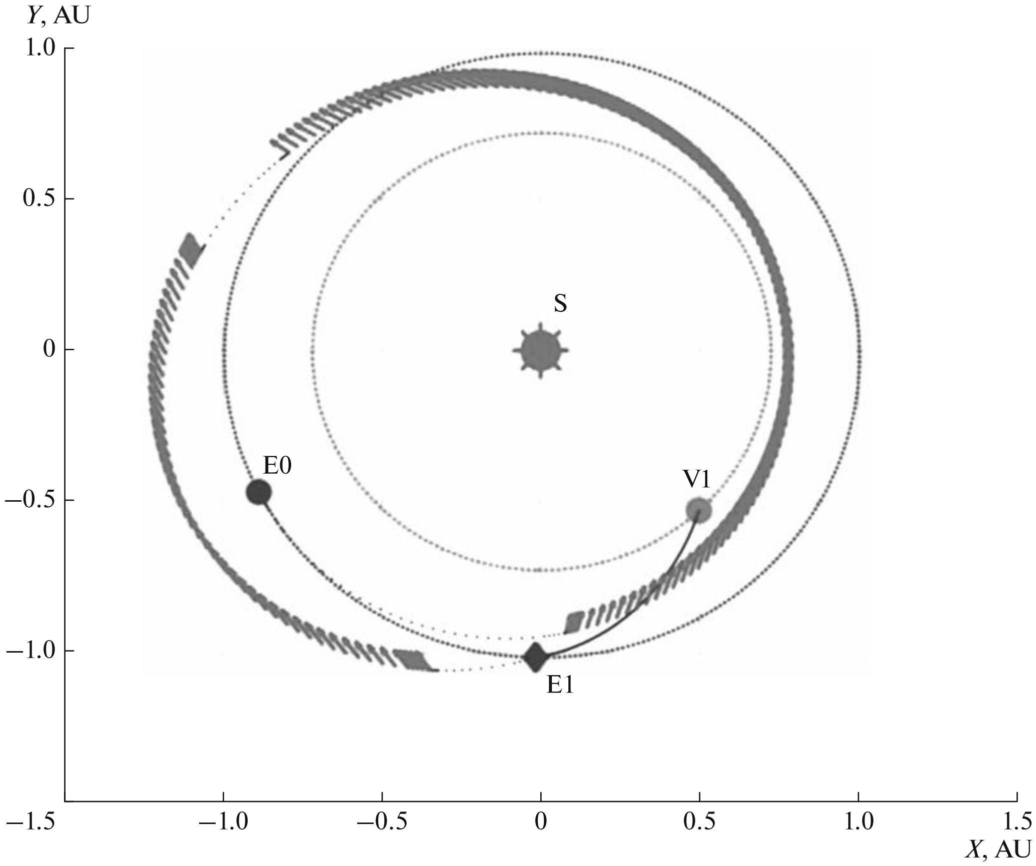

**Fig. 4.** Projection of the heliocentric Earth-Earth-Venus part of the Interhelioprobe orbit to the ecliptic plane. The Sun is shown by large grey circle S. Dark grey circle E0 is the Earth position during the launch of the spacecraft. Dark grey rhomb E1 is position of the Earth during the spacecraft gravity assist maneuver with it. Light grey circle V1 is the Venus position during the first spacecraft gravity assist maneuver with the planet. Dark and light grey closely spaced dots show the Earth and Venus orbits respectively. Grey arrows show directions of the Electric Propulsion System thrust during its active phase. Passive parts of the spacecraft orbit, with the disabled Electric Propulsion System, are shown by black sparse dots and solid curves.

the Sun. Orientation error of the viewfinder axis in inertial space is planned to be less than 1 arc-minute. Stabilizing deviation is less than 2.5 arc-seconds. Maximal angular velocity of stabilization is less than 1 arc-second per second. Scientific Payload will obtain information about the SC viewfinder axis with accuracy not less than 5 arc-seconds.

The Interhelioprobe SC (Fig. 8) consists of three main functional blocks:

1. Flight Module,
2. Transitional Framework with Separation System,
3. Scientific Payload.

The Flight Module includes:

—Onboard Control System,
—Antenna-Feeder System,
—Onboard Radio System,
—Electric Propulsion System,
—Orientation and Stabilization System,
—Power and Control System,

**Table 3.** Characteristics of the SC-2 orbits during the phase of flight with the gravity assist maneuvers with the Venus. The SC-2 launch from the Earth is assumed to be on 24 August 2022

| Gravity assist maneuver | Radius of perihelion, AU | Inclination to ecliptic, grad | Radius of aphelion, AU | Orbit period, days | Resonance $N_{SC} : N_{Venus}$ | Time of flight, days |
|---|---|---|---|---|---|---|
| 1 | 0.304 | 10.021 | 0.890 | 168.524 | 4 : 3 | 674.099 |
| 2 | 0.286 | 18.786 | 0.818 | 149.799 | 3 : 2 | 449.399 |
| 3 | 0.338 | 26.086 | 0.775 | 151.800 | No | |

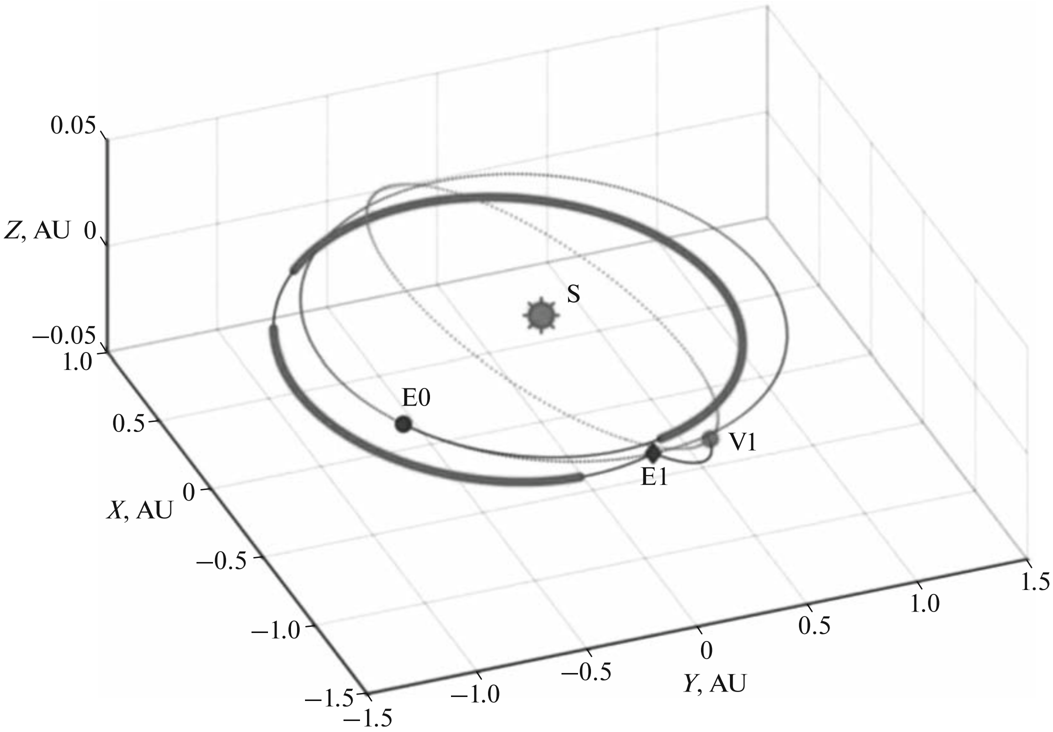

**Fig. 5.** Spatial view of the heliocentric Earth-Earth-Venus part of the Interhelioprobe orbit. All is the same as in Fig. 4. The scale of the Z-axis is increased.

—Telemetry System,

—Temperature Control System,

—Electrification Control System,

—Electrical Power System,

—Onboard Cable Network,

—Supporting Structure.

The Flight Module is subdivided on two modules – Engine Module and Payload Module. The Engine Module has a rectangular shape. It consists of a frame constructed from welded balks having angle cross-section and thermal honeycomb panels (THPs) mounted on sides. The THPs hold equipment of the Electric Propulsion System with two Engine Units, as well as the liquid propulsion engines of the Orientation and Stabilization System. The Electric Propulsion System is based on two stationary plasma engines (SPD-140). The THPs are also used to transmit lateral inertial loads. There are tanks of xenon and nitrogen inside the Engine Module. The High-Gain Parabolic Antenna with the drive is on the bottom plane of the Engine Module.

The Payload Module has a construction scheme similar with the Engine Module. All the service equipment and the Scientific Payload are attached to the THPs of the Payload Module. The Solar Panels with the drives are attached to the outer sides of the THPs.

The Protective Thermal Shield is fixed at the top level of the Payload Module with the use of the special Framework with Radiators. The Thermal Shield is used to protect the SC and all its payload from high fluxes of solar radiation reaching of ≈18 kW/m$^2$ near the perihelion. The Thermal Shield contains several windows with shutters to provide required field-of-views for the remote-sense instrumentations.

The Transitional Framework (not shown on Fig. 8) consists of a system of vertical stands and diagonal struts. They connect the “Fregat” Upper Stage with the Engine Module. There are pyrolocks and spring plungers on the upper nodes of the stands. They are used to separate the “Fregat” Upper Stage from the Engine Module at a certain phase of the flight, when all the fuel of the “Fregat” will be used.

## 6. GROUND CONTROL SEGMENT OF THE MISSION

The Interhelioprobe spacecraft (SC) will be managed by the Ground Control Segment (GCS) at all stages of its flight after separation from the launch vehicle. The GCS will provide the main following tasks:

(a) automatic planning of the SC’s functioning;

(b) formation and transmission of command-program information to the SC;

(c) receiving and processing of control and scientific telemetry information from the SC;

(d) ballistic-navigation support of the SC.

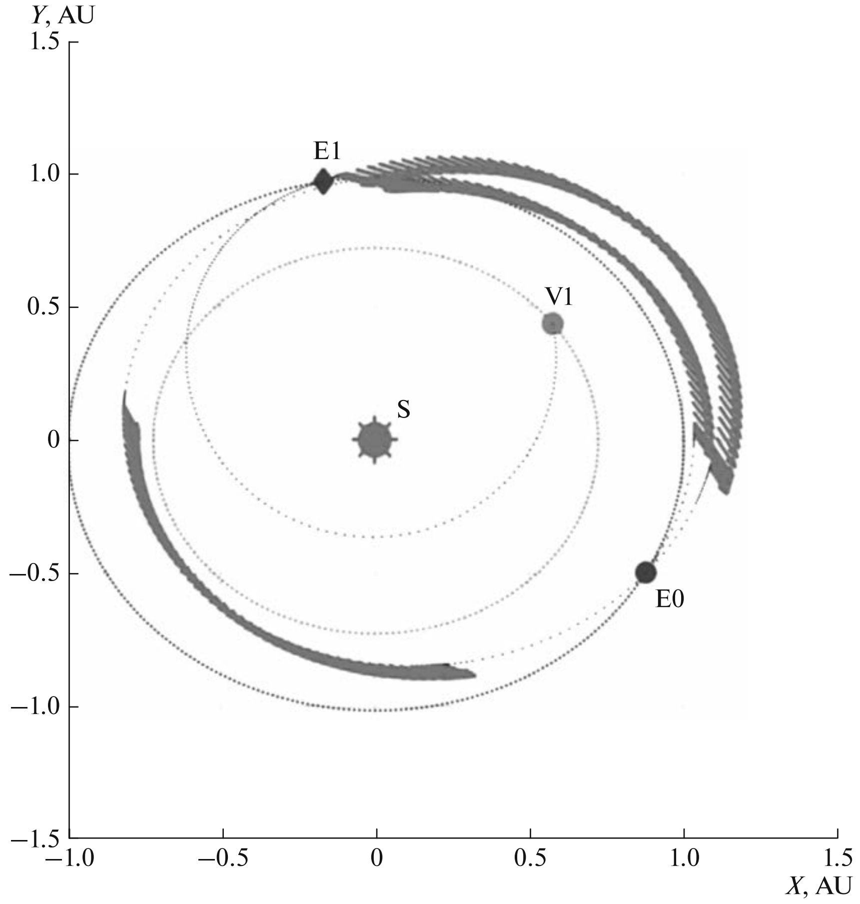

**Fig. 6.** Projection to the ecliptic plane of the heliocentric Earth-Earth-Venus part of the Interhelioprobe SC-2 orbit. The Sun is shown by large circle (S). Dark grey circle E0 is position of the Earth during the launch of the SC-2 (on 24 August 2022). Dark grey rhomb E1 is position of the Earth during the spacecraft gravity assist maneuver with it. Light grey circle V1 is Venus position during the first SC-2 gravity assist maneuver with the planet. Dark and light grey closely spaced dots show the Earth and Venus orbits respectively. Grey arrows show directions of the SC-2 Electric Propulsion System thrust during its active phase. Passive parts of the SC-2 orbit, with the disabled Electric Propulsion System, are shown by black sparse dots and solid curves.

The Ground Control Segment will mainly consists of:

1. Flight Control Center on the base of the Mission Control Center of the Central Research Institute of Machine Building (Korolev, Moscow Region, Russia),

2. Flight Control Center on the base of the Lavochkin Flight Control Center (Khimki, Moscow Region, Russia),

3. Two major Ground Control Stations – Antenna Station TNA-1500 (64-m antenna) “Medvezgyi Ozera” (Moscow Region, Russia) and Antenna Station P2500 (70 m antenna) “Ussuriysk” (Primorsky Krai, Russia),

4. Ballistic Center on the base of the Ballistic Center of the Keldysh Institute of Applied Mathematics of the Russian Academy of Sciences (Moscow, Russia),

5. Science Operation Center on the base of the Space Research Institute (IKI) of the Russian Academy of Sciences (Moscow, Russia).

## 7. SCIENTIFIC PAYLOAD

Scientific Payload of the Interhelioprobe mission consists of 19 instruments (Tables 4 and 5) to measure specific physical quantities and 4 supplementary (service) systems (Table 6) to manage the scientific instrumentation and to provide centralized data collection, storage and preliminary processing and analysis onboard the SC. The scientific payload is subdivided in two conditional groups:

1. 10 instruments for remote observations of the Sun (Table 4);

2. 9 instruments for local (in situ) measurements in the interplanetary space (Table 5).

Tables 7 and 8 represent energy bands and wavelengths, which will be covered by observations and measurements with each instrument. Table 9 gives information about main scientific organization responsible for each instrument and its principal investigators (PIs). Both Interhelioprobe SC (SC-1 and SC-2), if SC-2 will be approved, most probably,

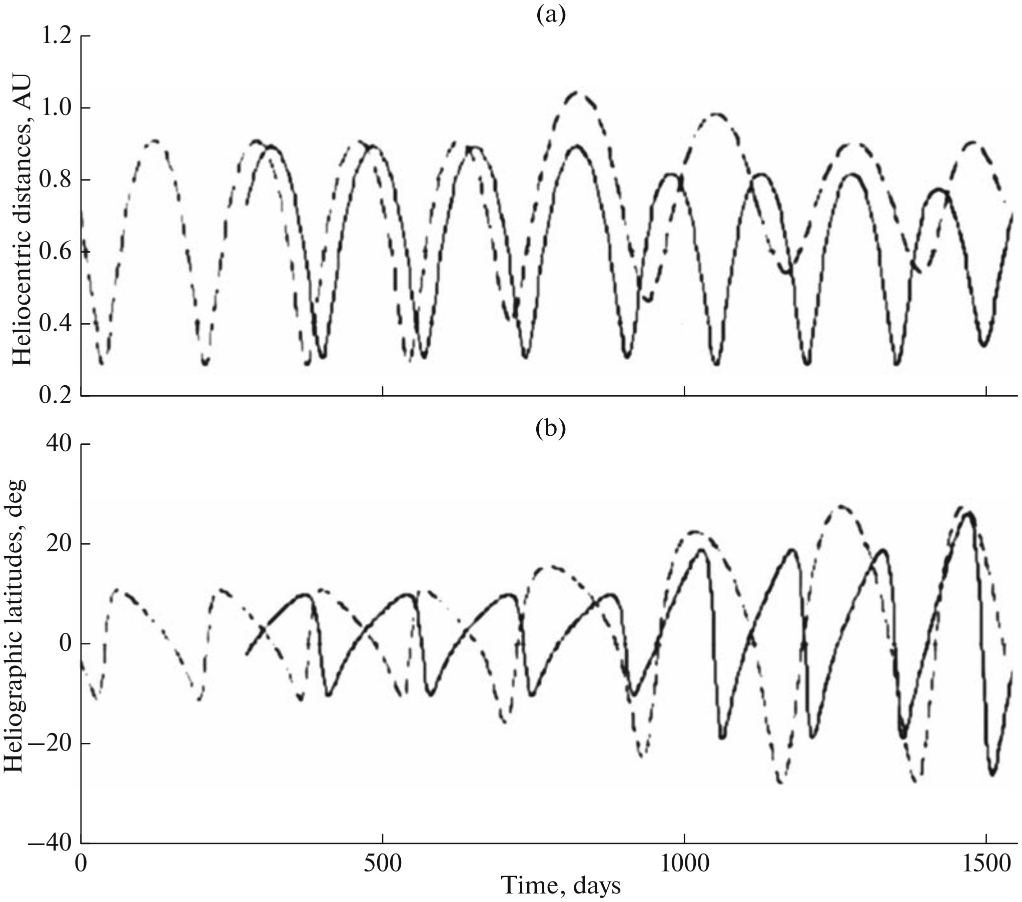

**Fig. 7.** Time profiles of the Interhelioprobe SC-1 (dashed curves) and SC-2 (black solid curves) heliocentric distances (a) and heliographic latitudes (b) shown for the periods of the spacecraft orbits starting from their first gravity assist maneuvers with the Venus. Launch dates of the SC-1 and SC-2 from the Earth are 18 April 2022 and 24 August 2022 respectively.

will be equipped with identical sets of Scientific Payload.

Total mass of the Scientific Payload is 160 kg, including interconnecting cables. Power supply of the onboard systems and Scientific Payload is provided by stabilized DC voltage of 27 ± 1.35 V in the stationary regime. Total power usage of the Scientific Payload is 50 W in the standby regime (non-observational mode) and 225 W in the operational regime (observations and measurements). Scientific data transfer at the SC-Earth line is provided by the High-Gain Parabolic Antenna with a rate of not less than 128 Kbit/sec at the maximal distance from the Earth of $270 \times 10^6$ km and with a rate from 256 kbit/sec up to 1024 Mbit/sec depending on distance between the SC and Earth. Data transfer at the SC-Earth line is also provided by Near-Omnidirectional Receiving and Transmitting Antennas at rate of not less than 8 bit/sec at the maximal distance from the Earth of $270 \times 10^6$ km. Maximal volume of data transferred at the SC-Earth line is not larger than 1 GB per 24 hours.

Brief descriptions of each scientific instrument are given below.

### *7.1. Multi-Functional Optical Complex TAHOMAG*

Multi-function optical complex TAHOMAG is intended to measure vectors of magnetic and velocity fields at the photosphere with high angular resolution and sensitivity. TAHOMAG operates in the optical wavelength range from 0.3 to 0.6 μm. The complex consists of three main parts:

- Supply Optical Telescope,
- Solar Spectro-Magnetograph,
- Narrowband Filter Package.

**7.1.1. Brief description of the supply optical telescope.** At perihelion the Interhelioprobe SC will be three times closer to the Sun than the Earth. This allows us to explore the small-scale structure of the solar plasma. In order to realize such a possibility, it is necessary to use a telescope with high spatial resolution, i.e., with the primary mirror of large diameter — 450 mm. The shadow of the input aperture should not

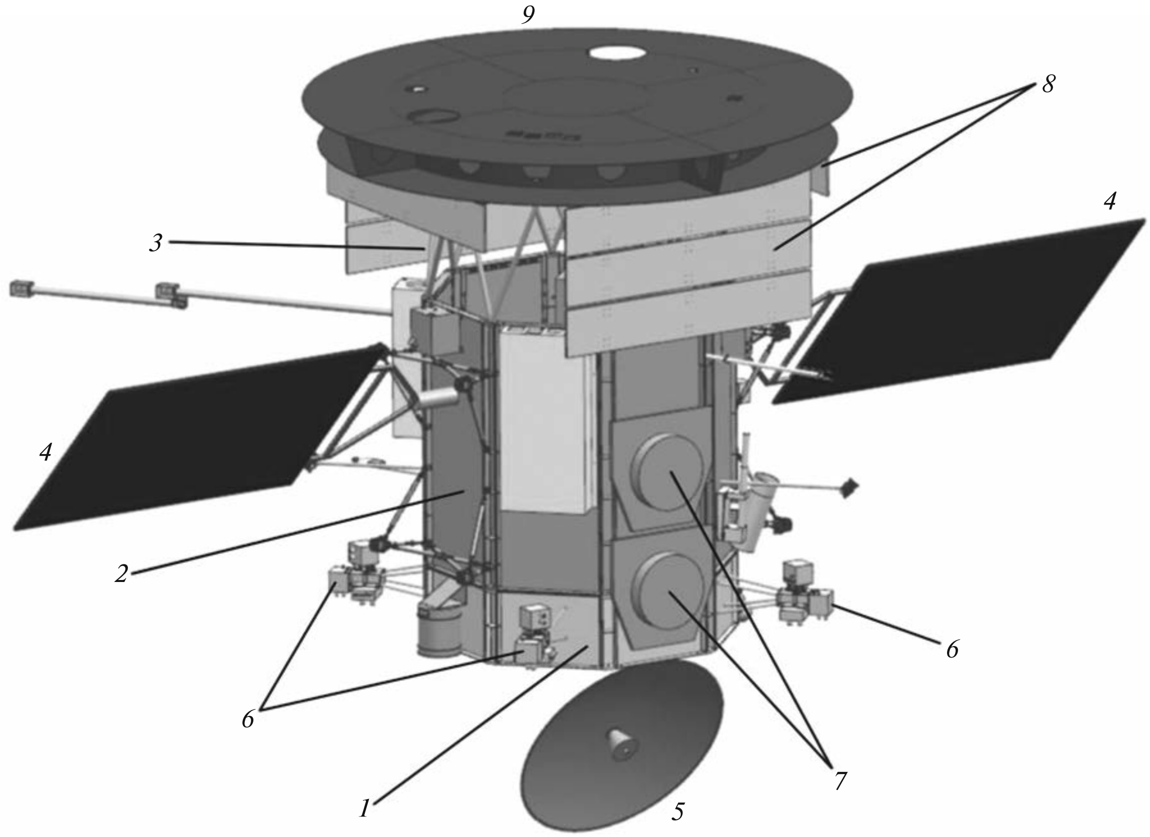

**Fig. 8.** Scheme of the Interhelioprobe spacecraft: (*1*) engine module; (*2*) payload module; (*3*) framework; (*4*) solar panels with drives; (*5*) high-gain parabolic antenna; (*6*) engine units of the orientation and stabilization system; (*7*) engine units of the electric propulsion system; (*8*) radiators; (*8*) protective thermal shield with windows.

fall on the primary mirror during observations at any possible position of the Sun. Therefore, the diameter of the input aperture must be even greater – 560 mm. The energy flux from the Sun at SC's perihelion is 17.6 kW/m$^2$, i.e. 12.8 times greater than the flux at the Earth orbit. Thus, the telescope will get the power of 4.5 kW. The need to remove this power from the spacecraft determines the choice of the optical scheme. The scheme used in the Solar Optical Telescope (SOT) onboard the Hinode satellite (Tsuneta et al., 2008) is unsuitable here, due not only to a large energy flux, but also to a large angular size of the Sun. As seen from Fig. 9, a diagonal mirror (MD), which sets off an area 700″ in diameter, is placed in the plane of the primary image. All radiation not related to this area (99% of the incident power at perihelion) goes back towards the Sun. Besides, the primary mirror consists of a transparent dielectric covered with stratified coating. This mirror reflects all the light in the spectral range required for measurements (0.630 and 0.3 μm) and transmits more than 80% of the incident radiation.

The Supply Optical Telescope is intended for solar imaging with a resolution of 0.35 arc seconds in the Spectro-Magnetograph wavelength range (0.630 μm) and 0.17 arc seconds in the blue spectral range (0.3 μm). We can see that the angular resolution of the Supply Optical Telescope is similar to that of the Hinode/SOT solar telescope. But at the Interhelioprobe perihelion (60 solar radii), this corresponds, respectively, to 70 and 35 km on the solar surface. The angular field of view of the telescope is $500 \times 500$ arc-seconds$^2$. The telescope is supplied with a system of image stabilization to within 0.03 arc-seconds. The optical layout of the instrument is illustrated in Fig. 9. It comprises a primary mirror M1 of 450 mm in diameter, a diagonal mirror (field mirror) MD, a secondary mirror M2 130 mm in diameter, a collimator lens L1-L2 with a working diameter of 40 mm, a piezo-driven tip-tilt mirror M3, and reimaging lens L3, L4 are the spectrograph lens. L5-L6 are the lenses related to the polarization analyzer, L7-L8 are the lenses for the narrow-band filter package. F1–F2 are the filters for the narrow-band filter package.

**7.1.2. Solar spectro-magnetograph.** The Solar Spectro-Magnetograph provides the Stokes parameters in the spectral range of 6300.5–6303.5 Å, which involves two magnetically active lines of neutral iron FeI 6302.5 and FeI 6301.5, with a spectral resolution of 32 mÅ. The instrument consists of a diffraction spectrograph comprising the input slit D1, collimator

**Table 4.** Interhelioprobe instruments for remote-sensing observations

| No | Instrument | Measurements | Characteristics | Mass, kg | Power, W |
|---|---|---|---|---|---|
| 1 | Multi-functional optical complex **TAHOMAG** | Stokes parameters. Vectors of magnetic and velocity fields at the photosphere. Intensity of white-light radiation | FOV = 500″ × 500″; $d\alpha = 0.17''$–$0.35''$;<br>$\lambda = 6300.5$–$6303.5$ Å, 3000 Å; $d\lambda = 32$ mÅ;<br>B = ±4000 Gs; dB = 2 Gs (line-of-sight) | 36 | 40 |
| 2 | Multi-channel solar photometer **PHOTOSCOPE** | Solar constant. Global oscillations of the Sun | FOV = 10°; $\lambda = 3000$–$16000$ Å; $d\lambda = 100$ Å; $dt = 16$ s | 6.5 | 12 |
| 3 | EUV and SXR telescope **TREK** | EUV and SXR images of the Sun. Localization of active regions. Fine structure of the solar atmosphere. Observations of high temperature plasma | FOV = 0.7°–2°; $d\alpha = 1.2''$–$3.5''$;<br>$\lambda = 131, 171, 304, 8.42$ Å | 14 | 15 |
| 4 | Solar HXR telescope-spectrometer **SORENTO** | Images of solar HXR sources and their energy spectra | FOV = 1.5°; $E = 5$–$100$ keV; $d\alpha = 7''$; $dt = 0.1$ s | 8 | 6 |
| 5 | Solar coronagraph **OKA** | White-light images of the solar corona, eruptive events, transients, CMEs | FOV = 8°; $d\alpha = 28''$; $\lambda = 4000$–$6500$ Å | 5 | 7 |
| 6 | Heliospheric Imager **HELIOSPHERA** | White-light images of the outer corona and inner heliosphere, CMEs | FOV = 20°; $d\alpha = 70''$; $\lambda = 4000$–$6500$ Å | 5 | 7 |
| 7 | X-ray spectrometer **CHEMIX** | Spectra of solar X-ray emission. Chemical composition of solar corona plasma | FOV = 10°; $d\alpha = 5'$; $\lambda = 1.5$–$9$ Å | 6 | 21.5 |
| 8 | Hard X-ray polarimeter **PING-M** | Fluxes, energy spectra of solar soft X-ray emission<br>Fluxes, energy spectra, polarization of solar hard X-ray emission | $E_x = 1.5$–$25$ keV; $dE = 200$ eV (at 5.9 keV);<br>$dt \geq 0.1$ s<br>$E_{x,\gamma} = 20$–$600$ keV; $dE/E = 0.12$ (at $E = 60$ keV);<br>$dt \geq 0.1$ s; $E_{\text{polar}} = 18$–$150$ keV | 13.5 | 19.5 |
| 9 | Scintillation gamma-spectrometer **HELIKON-I** | Fluxes and spectra of hard X-rays and gamma-rays (of not only solar origin) | $E = 0.01$–$15$ MeV; $dE/E = 0.08$ (at $E = 662$ keV);<br>$dt = 0.001$–$8$ s | 10.5 | 10 |
| 10 | Gas gamma-ray spectrometer **SIGNAL** | Fluxes and spectra of solar gamma-rays | $E_\gamma = 0.03$–$5.00$ MeV; $dE/E = (1.7 \pm 0.3)\%$<br>(at 662 keV) $dt = 0.1$–$60$ s | 5 | 20 |
|  |  |  |  | **109.5** | **158.0** |

FOV—field-of-view; $\lambda$—wavelength; $E$—energy; $E_{\text{polar}}$—energy of polarized emission; $E_{x,\gamma}$—energy of X-rays and $\gamma$-rays; B—magnetic induction; $f$—frequency; $m$—mass; $v$—velocity; $d\lambda$—spectral resolution; $dE$—energy resolution; $d\alpha$—angular resolution; $dt$—time resolution; $dv$—velocity resolution; dB—magnetic induction resolution.

**Table 5.** Interhelioprobe instruments for in situ measurements

| No | Instrument | Measurements | Characteristics | Mass, kg | Power, W |
|---|---|---|---|---|---|
| 1 | Analyzer of solar wind electrons **HELIES** | Distribution functions of solar wind electrons | FOV = 120° × 360°; $E = 1–5000$ eV; $dE/E = 0.18$ | 2.5 | 3 |
| 2 | Analyzer of solar wind ions **HELION** | Energy and angular spectra of solar wind ions | Ions: FOV = 120° × 100°; $E/q = 0.04–12$ keV/q; $dE/E = 0.07$; $dt = 10–100$ s<br>Electrons: FOV = 15° × 60°; $E = 0.35$ eV–6.30 keV; $dE/E = 0.16$ | 1.8 | 1.5 |
| 3 | Energy-mass-analyzer of solar wind plasma **PIPLS-B** | Energetic and mass composition of solar wind ions; distribution functions of solar wind ions | FOV = 45° × 45°; $E = 1–20$ keV; $m/q = 2–9$; $m/dm = 10–40$; $d\alpha = 2°–9°$; $dE/E = 0.05$; $dt > 1$ min | 2.5 | 4 |
| 4 | Dust particle analyzer **PIPLS-A** | Interplanetary and interstellar dust particles | $m = 10^{-16}–10^{-6}$ g; $m/dm = 100$; $v = 5–100$ km/s | 2.5 | 9.8 |
| 5 | Magnetometer **HELIOMAG** | Heliospheric magnetic field and its disturbances | B = ±1000 nT<br>dB = 2 pT | 1.9 | 5 |
| 6 | Electromagnetic wave complex **IMWE** | Fast variations of magnetic fields, ion fluxes | $f$ =300 Hz – 30 MHz<br>$E/q = 0.05–5$ keV/q; $dE/E = 5–7\%$; $dt = 0.031$ s | 9.5 | 18 |
| 7 | Radiospectrometer **RSD** | Radio emission of solar corona and solar wind plasmas | $f$ = 15 kHz – 300 MHz<br>DR = 80 dB | 2.2 | 10 |
| 8 | Charged particle telescope **SKI-5** | Energetic charged particles in the interplanetary space | Electrons: $E = 0.04–10$ MeV<br>Protons: $E = 2–120$ MeV<br>Ions: $E = 10–200$ MeV/nucleon | 4.5 | 14 |
| 9 | Neutron detector **INTERSONG** | Solar neutrons, hard X-rays and gamma-rays | $E_n = 3–100$ MeV;<br>$E_\gamma = 0.03–10$ MeV | 6.5 | 15 |
|  |  |  |  | **33.4** | **80.3** |

FOV—field-of-view; λ—wavelength; $E$—energy; $E_n$—energy of neutron; $E_\gamma$—energy of γ-rays; B—magnetic induction; $f$—frequency; $m$—mass; $v$—velocity; $q$—electric charge; DR—dynamic range; dλ—spectral resolution; d$E$—energy resolution; dα—angular resolution; d$t$—time resolution; d$v$—velocity resolution; dB—magnetic induction resolution.

**Table 6.** Interhelioprobe Scientific Instrumentation Supplementary Systems

| No | System | Function | Responsible Organization | Mass, kg | Power, W |
|---|---|---|---|---|---|
| 1 | Scientific data collection and storage system **SSNI** | Collection and storage of scientific data and its transmission to the onboard Radio System. Receiving of control commands from the SC's Control System to manage the scientific instrumentation | Space Research Institute (IKI), Moscow, Russia | 5 | 6 |
| 2 | Switching and control system **BUS** | Management of the Scientific instrumentation through supply chains | Space Research Institute (IKI), Moscow, Russia | 3 | 2 |
| 3 | Control unit of the imaging instrumentation **BK-HOST** | Management of the imaging instrumentation block (TREK, SORENTO, OKA, HELIOSPHERA). Preliminary processing and analysis of its scientific datasets | Lebedev Physical Institute (LPI), Moscow, Russia | 2.5 | 5 |
| 4 | Onboard cable network **BKS** | Power supply of the scientific instrumentation. Transfer of information from the scientific instrumentation to the SSNI. Transfer of control commands from the BUS to the scientific instrumentation | Space Research Institute (IKI), Moscow, Russia | 10 | 0 |

**Table 7.** Coverage of electromagnetic emission by the Interhelioprobe remote-sense instrumentation

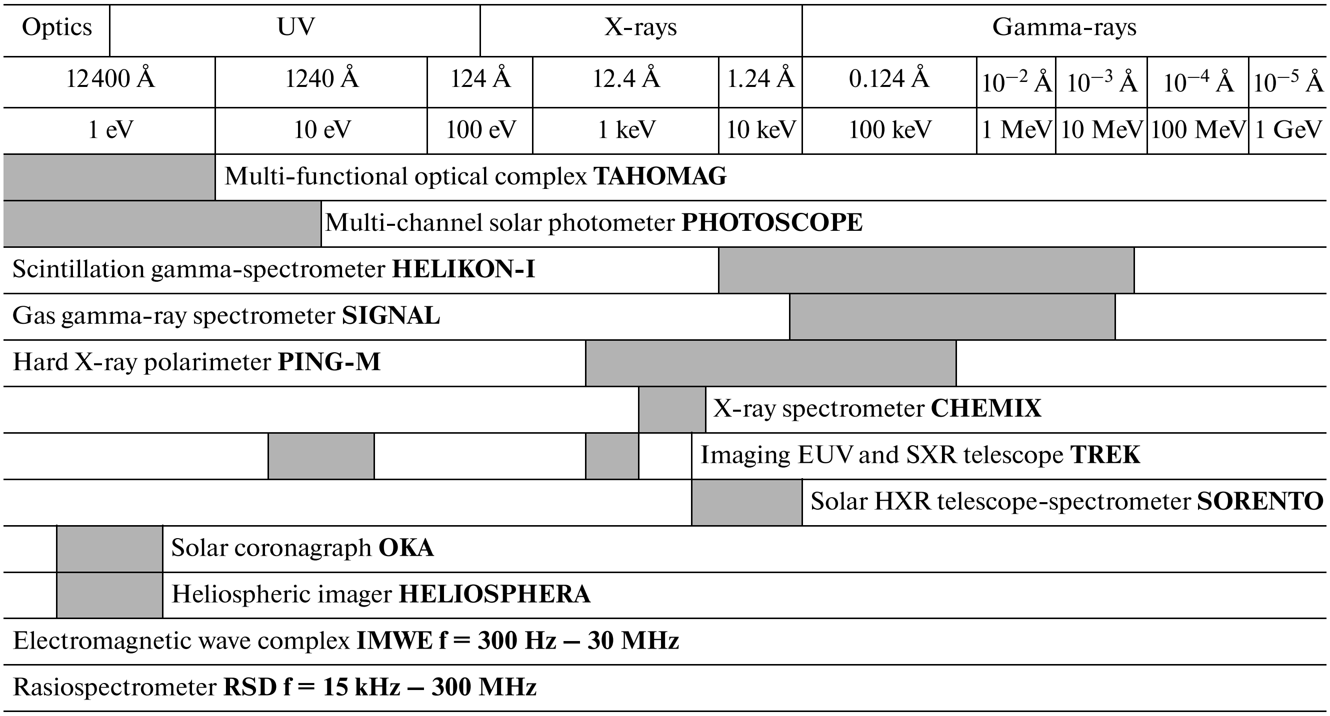

L4, diffraction grid G, output slit D2, folding mirror M4, and the polarization optics assembly comprising collimator L5, parallel polarization analyzer PA, focusing lens L6 and CCD detectors CCD3.

**7.1.3. Narrowband filter package.** The Narrowband Filter Package provides solar images in narrow spectral bands. The package comprises two spectral beam splitters BS1-BS2, narrow-band filters F1, F2, reimaging lenses L7, L8 and a CCD cameras CCD1, CCD2. At present, we are planning to install two narrowband filters: one in the 0.3 μm continuum for obtaining photospheric images with a resolution of 35 km and the other in Hα for imaging the chromosphere and corona with a resolution of 70 km. The

**Table 8.** Particle coverage by the Interhelioprobe in-situ instrumentation

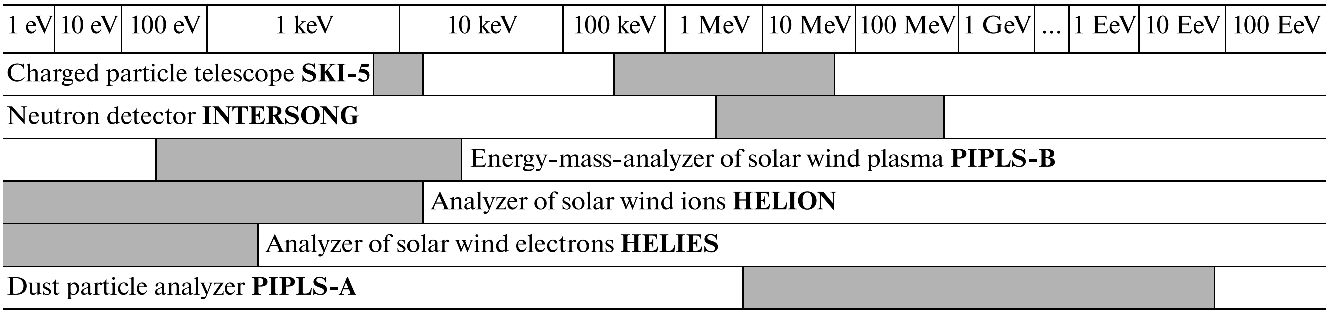

**Table 9.** Collaboration of the Interhelioprobe Scientific Instrumentation

| Instrument | Principal Investigator (Institution) | Scientific Collaboration |
|---|---|---|
| Multi-functional optical complex **TAHOMAG** | V.N. Obridko (IZMIRAN) | IZMIRAN, NIRFI |
| Multi-channel solar photometer **PHOTOSCOPE** | V.D. Kuznetsov (IZMIRAN) | IZMIRAN |
| Imaging EUV and SXR telescope **TREK** | S.A. Bogachev (LPI) | LPI, IAS |
| Solar HXR telescope-spectrometer **SORENTO** | S.A. Bogachev (LPI) | LPI, IKI, CEA Saclay, CBK PAN ZFS |
| Solar coronagraph **OKA** | S.V. Shestov (LPI) | LPI |
| Heliospheric Imager **HELIOSPHERA** | S.V. Shestov (LPI) | LPI |
| X-ray spectrometer **CHEMIX** | J. Sylwester (CBK PAN),<br>V.D. Kuznetsov (IZMIRAN) | CBK PAN ZFS, IZMIRAN, LPI, IRA NASU |
| Hard X-ray polarimeter **PING-M** | Y.D. Kotov (NRNU “MEPhI”) | NRNU “MEPhI”, IPTI |
| Scintillation gamma-spectrometer **HELIKON-I** | R.L. Aptekar (IPTI) | IPTI |
| Gas gamma-ray spectrometer **SIGNAL** | S.E. Ulin (NRNU “MEPhI”) | NRNU “MEPhI” |
| Analyzer of solar wind electrons **HELIES** | R.A. Kovrazhkin (IKI)<br>B. Lavraud (IRAP) | IKI, IRAP, ONPU |
| Analyzer of solar wind ions **HELION** | M.I. Verigin (IKI)<br>J. Ŝimůnek (IAP) | IKI, IAP, IGEP TUB, MPS, ONPU |
| Energy-mass-analyzer of solar wind plasma **PIPLS-B** | O.L. Vaisberg (IKI) | IKI |
| Dust particle analyzer **PIPLS-A** | O.L. Vaisberg (IKI) | IKI |
| Magnetometer **HELIOMAG** | V.A. Styazhkin (IZMIRAN) | IZMIRAN, IGEP TUB, IWF, PIC GPI, IC London UK |
| Electromagnetic wave complex **IMWE** | A.A. Skalsky (IKI) | IKI, LPC2E, FMP CU, IAP, LC ISR |
| Radiospectrometer **RSD** | V.V. Fomichev (IZMIRAN) | IZMIRAN |
| Charged particle telescope **SKI-5** | M.I. Panasyuk (SINP MSU) | SINP MSU |
| Neutron detector **INTERSONG** | M.I. Panasyuk (SINP MSU) | SINP MSU |

The majority of abbreviations are presented in the authors affiliation list. Not listed ones are described below.
IAS—Institut d’Astrophysique Spatiale (Orsay, France);
CEA Saclay—The Saclay Nuclear Research Centre, DSM/DAPNIA/Service d’Astrophysique (Saclay, France);
PIC GPI—Physics Instrumentation Center at General Physics Institute of the Russian Academy of Sciences (Troitsk, Russia);
IC London UK—Imperial Colledge London (London, United Kingdom);
LPC2E—Laboratoire de Physique et Chimie de l’Environnement et de l’Espace (Orleans, France);
FMP CU—Faculty of Mathematics and Physics, Charles University (Prague, Czech Republic);
LC ISR—Lviv Center of Institute for Space Research (Lviv, Ukraine).

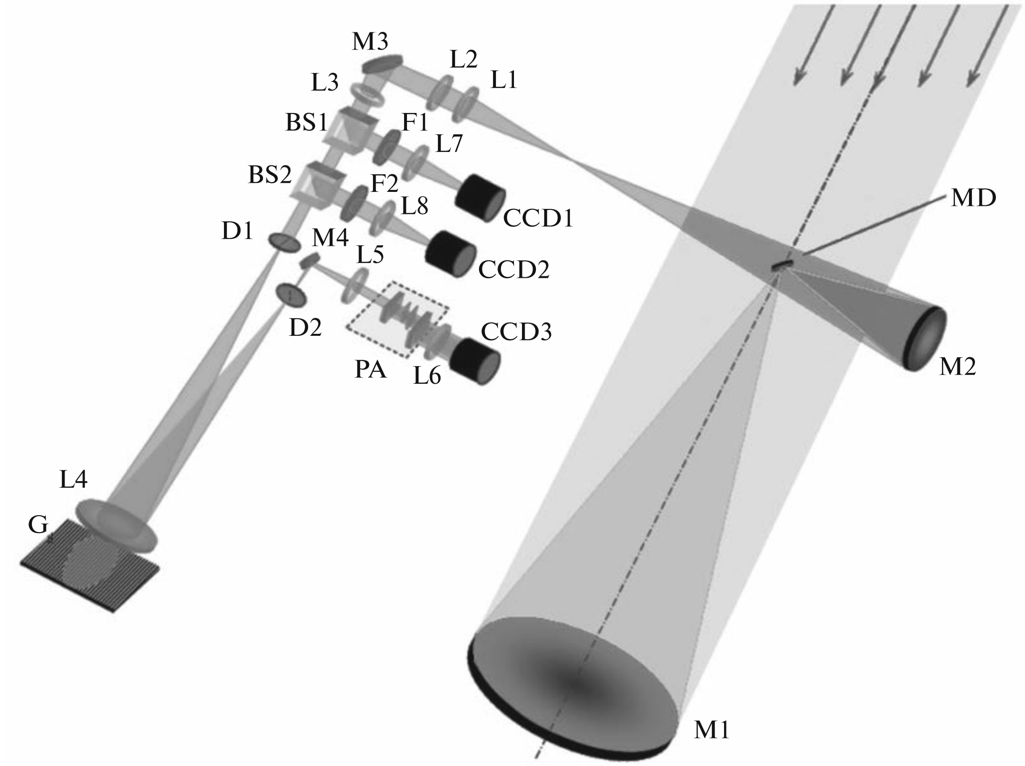

**Fig. 9.** Optical layout of the TAHOMAG complex. M1—Primary parabolic mirror; M2—Secondary aspheric mirror; MD—diagonal mirror-diaphragm; L1, L2—collimators; M3—scanning mirror; L3—reimaging lens; D1, D2—slits; L4—collimator; G—grating; M4—folding mirror; L5—collimator; PA—polarization analyzer; L6—reimaging lens; BS1, BS2—beam splitters; F1, F2—narrow-band filter package; L7, L8—lens; CCD1-CCD3—CCD-cameras. Incoming sunlight is shown by the faint grey strip with arrows.

final configuration of the Narrowband Filter Package is not yet determined. The decision will be taken jointly by all participants of the international cooperation.

**7.1.4. Polarization analyzer of optical radiation.** The PA is one of the basic elements of the solar magnetographs. Despite a variety of used design and structural solutions, the requirement of the controllability of the polarization analyzer is common for most solar magnetographs. This is most frequently performed by mechanical manipulations with the polarization elements or by applying electric voltages with the use of electro-optical effects.

A fundamental distinguishing feature of our PA which determines its design and structural features, is the absence of both controllable elements and the necessity of control. All parameters of the polarization optical radiation (components of the Stokes vector) are recorded simultaneously (in parallel). The advantages of such a scheme of the PA are not only its high response speed but also a significantly decreased effect of the instrument instability factors on the result of the spectral–polarization analysis.

Figure 10 shows the optical scheme of the PA. The scheme includes an entrance slit, a collimator L5, a beam splitter, two quarter wavelength plates, a polarization splitter, and an objective L6 that constructs an image of the entrance slit on the CCD array.

The entrance slit of the PA is simultaneously the spectrograph's output slit that limits the spectral range of the analyzed radiation. The objective lens L5 at whose focus the PA entrance slit is positioned associates each point of the spectrum image with a parallel beam of rays. The beam splitter divides each beam into three beams with maximally equal intensities and minimal polarization distortions. Although unequal light intensities and polarization distortions are taken into account by the subsequent calibration, the requirement of the identity of beams at the beam splitter output is not surplus.

As it is seen from Fig. 10, the first beam that emerges from the beam splitter without reflections sequentially passes through two-quarter wavelength plates, which are turned with respect to each other by an angle of 45°; the second beam is reflected twice in the beam splitter and passes through one quarter-wavelength plate, while the third beam after four reflections passes directly to the polarization beam splitter. The combination of quarter-wavelength plates used in the scheme is typical. The difference is that, in

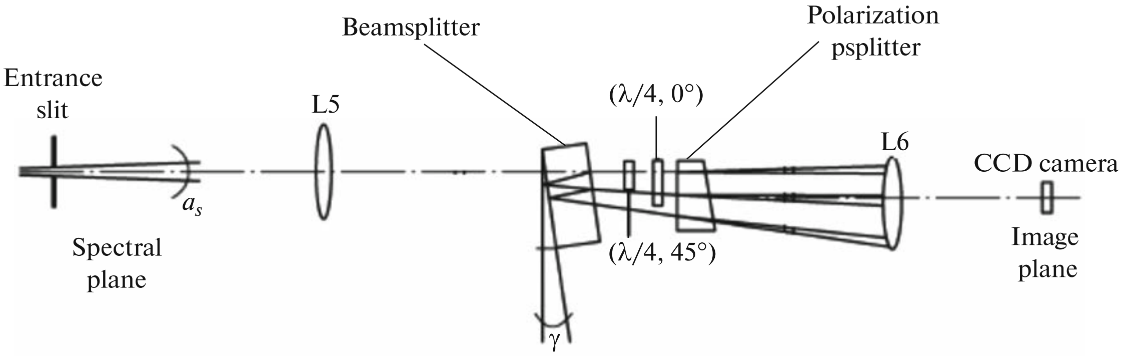

**Fig. 10.** Optical scheme of the TAHOMAG polarization analyzer (PA).

known PAs, a beam sequentially passes through a combination of quarter-wavelength plates as a result of controlling the PA. In the presented scheme, the beam passing through the elements of the combination is sequentially divided into six parts and a separate image is constructed at the PA output for each beam. In this case, the PA state remains constant and the polarization analysis is performed in parallel. In addition, it should be noted that the quarter-wavelength plates are manufactured as zero-order elements, and this determines their broad passband and high luminosity.

The combination of a quarter wavelength plates and the linear-polarization analyzer, provided that these elements were perfectly manufactured, yields the following intensities in each of the six beams at the PA output: I + Q (1), I – Q (2), I + V (3), I – V (4), I + U (5), I – U (6). Here, I, Q, U, and V are the Stokes parameters in accordance with the conventional notation.

Figure 11 shows the spectrum obtained at the IZMIRAN ground based analogue for different combinations of polarization parameters. Further processing with the use of appropriate spectral line transfer theory allows us to find all components of magnetic field, Doppler velocity, turbulence characteristics and with some additional assumptions to construct a model of the solar atmosphere at each point of observation.

### *7.2. Observations of Brightness Fluctuations of the Sun as a Tool for Exploration of Solar Variability and Global Oscillations (Experiment PHOTOSCOPE)*

The scientific payload of the mission will allow us to observe the solar irradiance in the entire energy range from X-rays to radio emission. In this context, measurements of the solar radiation flux, its fluctuations, and spectral distribution in the wavelength range from 300 nm to 1600 nm carried out within the framework of the PHOTOSCOPE experiment will provide continuous energy spectrum in the optical and near infrared ranges.

The multichannel solar photometer – PHOTOSCOPE is intended for continuous measurements of intensity variations in the solar irradiance in the spectral range from UV to near IR at close distances both from the ecliptic plain and from out-of-ecliptic, strongly inclined Interhelioprobe orbits.

The photometer enables continuous spectral and integral-flux measurements in the range of 300–1600 nm. Spectral measurements will be carried out with the single-element optical spectrometer based on the Fery prism. In this spectrometer, the prism combines the properties of the dispersing element and focusing optics. It is made of quartz optical glass, highly resistant to UV radiation. The spectral decomposition of the input slit image is obtained on the multi-element NMOS linear image sensor. Si and InGaAs photodiodes integrated in a structure called a trap detector are used as photodetectors for measuring the integral solar radiation flux. The photometer (Fig. 12) is a single unit mounted on the upper platform of spacecraft immediately under the thermal shield.

The instrument has two identical measuring channels. Each of them involves photodetectors of solar irradiance and a spectrometer. The main measuring channel will work continuously throughout the Interhelioprobe active period, while the calibration channel will be switched on briefly approximately once a month. As a result, the degradation of optical and photosensitive elements exposed to the luminous flux and corpuscular particles will not virtually affect the parameters of the calibration channel. So, a periodic calibration of the main channel will be performed by comparing the measurement data obtained in both channels.

The principal specifications of the photometer are as follows:

Spectral measurements:

—wavelength range observed – 300–1050 nm;

—wavelength resolution – no more than 10 nm;

—sampling time – 16 s;

Integral measurements:

—wavelength range observed – 300–1600 nm;

—sampling time – 16 s;

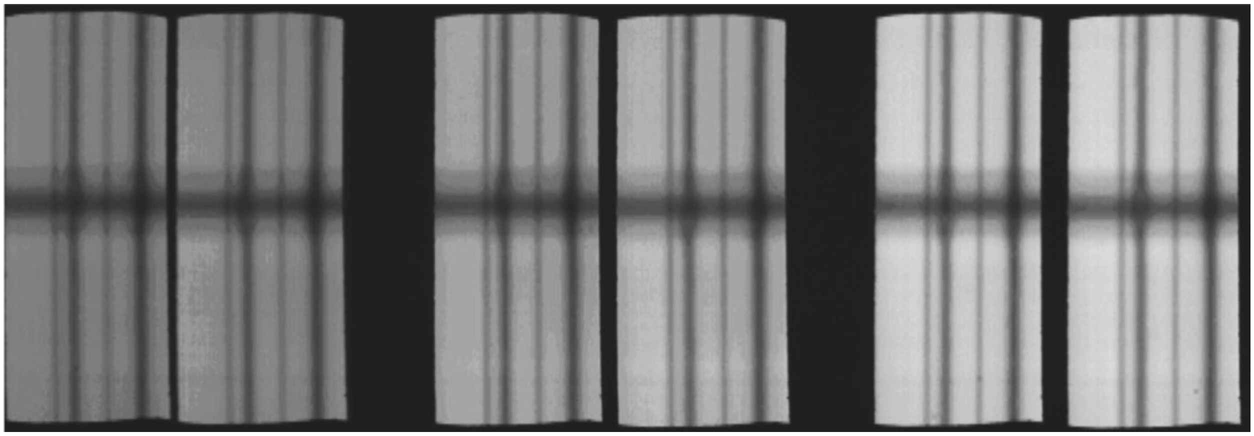

**Fig. 11.** Spectra in six polarizations in the presence of a solar spot on the spectrograph entrance slit (data of the IZMIRAN ground based analogue of the TAHOMAG complex).

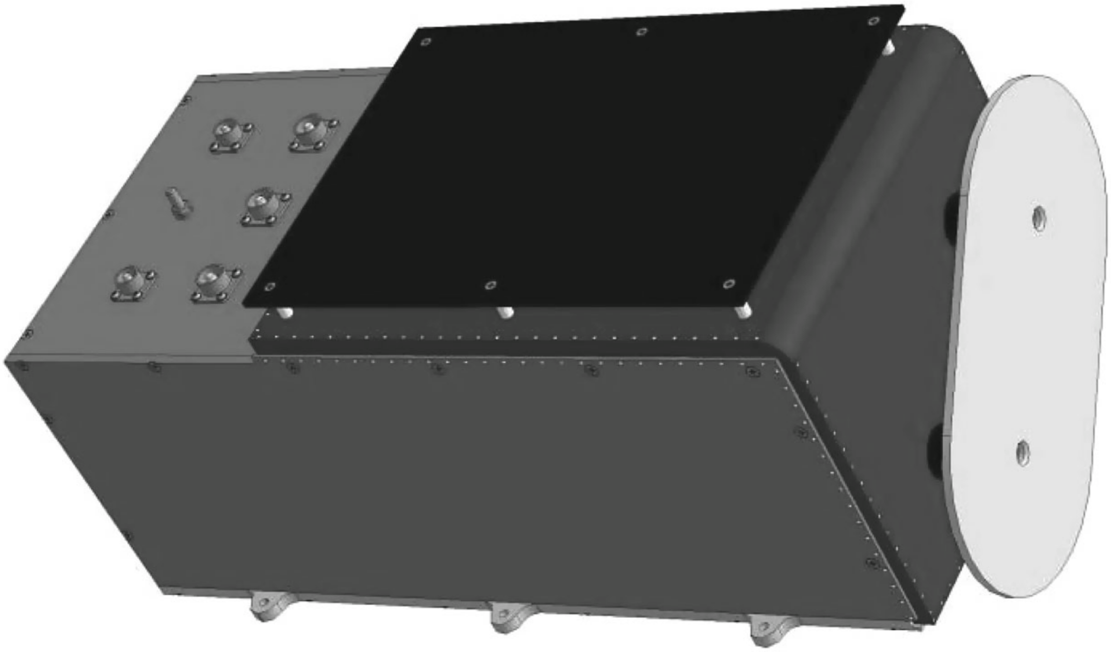

**Fig. 12.** PHOTOSCOPE photometer.

—accuracy of the solar-radiation intensity measurements – no worse than 0.3%;

—long-term stability of the solar-radiation intensity measurements – no worse than 0.1%/year;

General characteristics:

—daily amount of data – no more than 20 Mb;

—power – no more than 12 W;

—size – 224 × 182 × 470 mm;

—mass – 6.5 kg.

The scientific program of the PHOTOSCOPE experiment is focused on two aspects of the solar physics: (1) measurements of the solar irradiance in a broad spectral range (from UV to near IR radiation), i.e., the so-called “quasi-solar constant”, and (2) the study of processes in the photosphere and sub-photospheric layers based on observations of the global oscillations of the Sun.

So far, the best measurements of the solar constant were obtained from orbital spacecrafts; i.e. actually, the radiation flux from the solar hemisphere visible from the Earth has been measured (Fröhlich et al., 1997). The experiment under discussion is supposed to measure the solar flux at different azimuth angles, including out-of-ecliptic positions. Combined with ground-based data, these measurements will enable a comprehensive study of fluctuations of the solar irradiance under the influence of various manifestations of solar activity (from flares to the 11-year cycle). The advantage of this experiment is the possibility to measure the distribution of the solar radiation flux in the optical and near IR ranges, which will allow us to study the spectral re-distribution of energy depending on the level of solar activity.

Measuring time fluctuations in the solar radiation spectrum, particularly in its HF part, is important because of their significant effect on processes in the Earth upper atmosphere (Ermolli et al., 2012).

The other group of problems to be addressed by the PHOTOSCOPE experiment is associated with the study of global oscillations of the Sun. It should be noted that precise determination of all parameters of the solar oscillation p-modes is only possible when they are observed simultaneously over the entire surface of the Sun, while the measurements available nowadays have been taken on its visible side (Fröhlich et al., 1997; Zhugzhda et al., 2014). In this context, the opportunity to observe at different azimuth angles the fluctuations of the solar irradiance caused by global oscillations is of particular importance. Such observations, together with the data provided continuously by ground-based observatories and Earth orbiting spacecrafts will increase the accuracy of determining the eigenfrequencies and their splitting characteristics due to the solar rotation (Zhugzhda, 2006; Zhugzhda and Lebedev, 2009; Zhugzhda et al., 2014).

In addition, the PHOTOSCOPE photometer is able to measure the oscillation power at a large number of observation wavelengths determined by the characteristics of the attached spectrometer. All space-borne instruments currently used to observe the global oscillations of the Sun can take measurements only in a few relatively narrow spectral ranges. In PHOTOSCOPE, the number of spectral channels has been increased several times compared to the previous experiments. This will facilitate a detailed study of 5-minute oscillations in the photosphere, because the radiation at different wavelengths comes from different photospheric layers (Zhugzhda et al., 2014).

It is worth noting that all previous observations of the radiation flux and global oscillations of the Sun were carried out from the ecliptic plane and the Sun-Earth line. Out-of-ecliptic observations as well as the observations at different azimuth angles are unique per se and will significantly improve the quality of research.

### *7.3. EUV and SXR Telescope TREK*

The multichannel telescope TREK is designed to image solar transition region and corona in the EUV bandpass. TREK includes wide-field (WF) channels with full-Sun coverage and high-resolution (HR) channels for the detailed imaging of separate regions of interest. The Sun will be observed in four spectral lines: He II 304 Å ($T \approx 0.08$ MK), Fe IX 171 Å ($T \approx 0.8$ MK), Mg XII 8.42 Å ($T > 4$ MK) and Fe XXIII 131 Å ($T > 6$ MK).

The main scientific goals of the instrument include:

—investigation of structure and dynamics of solar transition region and low corona;

—study of the formation mechanisms of hot coronal plasma in active regions;

—observations of the eruptive solar events in a height range up to 1 solar radius above the photosphere;

—investigation of major counterparts of solar flares in EUV spectral range;

—observations of micro- and nano-flares in active regions and quiet corona.

The instrument design is based on multicoated reflective optics and a backside illuminated CCD-matrix. HR-channels incorporate a dual-mirror layout (Ritchey-Chretien type) while WF-channels have a single mirror off-axis optical scheme (Hershel type). A set of thin-film multilayer filters placed in the entrance aperture and focal plane are used to cut off the white-light radiation. The light scattered by the thermal shield of the spacecraft is controlled by the baffle attached to the front panel of the instrument. The baffle has a reflective inner surface, which directs the excesses of optical emission back to the entrance window. The rendered view of the TREK 3d-model is illustrated in Fig. 13.

Two of the WF channels (171 and 304 Å) are embodied in a single configuration. The focusing mirror of 171/304 telescope is divided into two halves, one of which is sensitive to 171 Å line and another – to 304 Å. Channel selection is organized via rotation of a selector wheel placed in front of the mirror. To increase the reflectivity of the third WF channel (Mg XII, 8.42 Å) a spherically bended crystal of fused silica is used instead of a “standard” multicoated mirror. The principal optical layout of WF-channels is depicted in Fig. 14. Both HR channels (131 and 304 Å) are designed as separate telescopes. The principal optical layout of HR-channels is presented in Fig. 15. The main technical parameters of TREK channels are listed in Table 10.

### *7.4. Solar HXR Telescope-spectrometer SORENTO*

SORENTO is an instrument for X-ray imaging spectroscopy in the energy range 5–100 keV with high spatial and energy resolution. The main operating principle is indirect Fourier imaging. Images are restored by the Fourier components distinguished by subcollimators. X-ray telescope SORENTO includes 3 main units: X-ray filters, imager and detector unit. The main characteristics of SORENTO are given in Table 11.

**7.4.1. Scientific tasks of SORENTO**—Investigation of thermal and non-thermal components of solar flare X-ray emission; testing the models of thick and

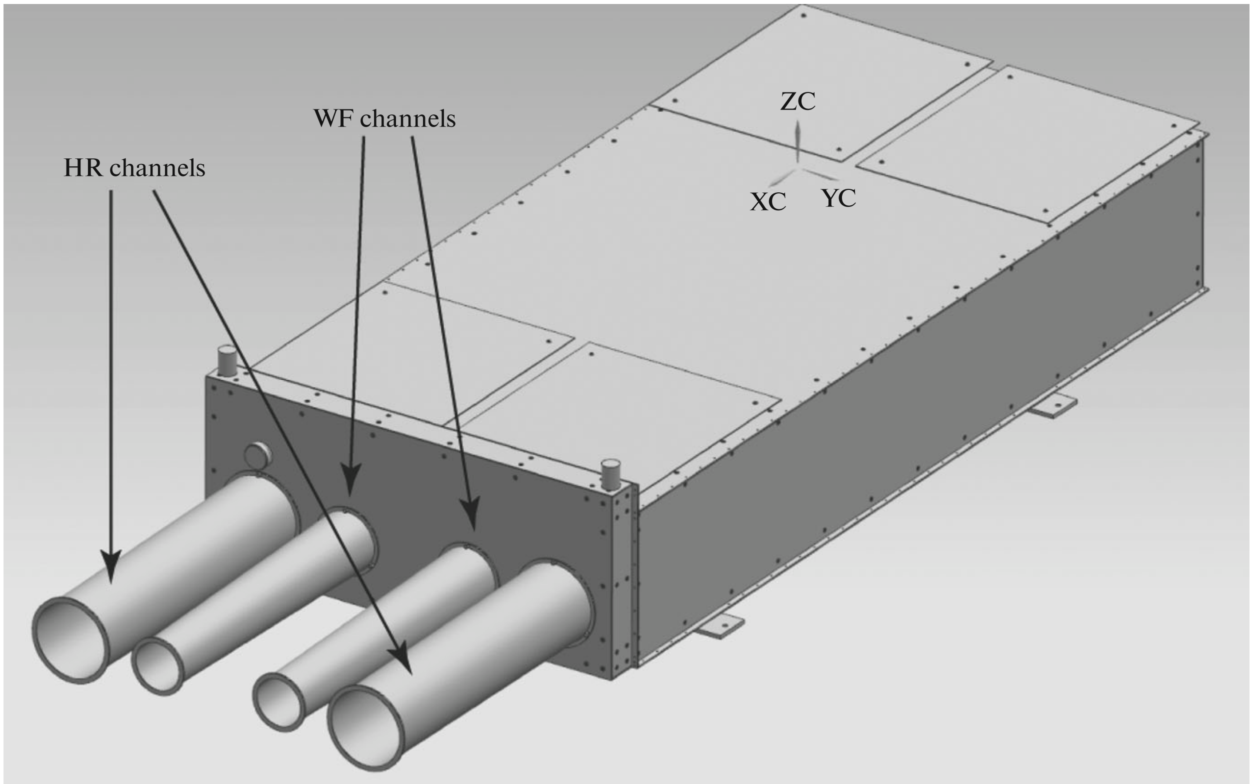

**Fig. 13.** 3d-model of the TREK instrument.

thin targets of energy release during the impulse phase of flares; testing the model of collapsing magnetic traps for coronal sources of hard X-ray emission and particles acceleration during the impulse phase of flares;

—analyzing of primary energy release regions in solar corona;

—exploring the mechanisms of electron acceleration in solar flares;

—flaring plasma diagnostics: determination of temperature, emission measure, electron concentration of emission sources;

—diagnostics of accelerated electrons in solar flares: measuring its rates, total energy, and energy distribution;

—investigation of hot (T ~ 10 MK), very hot (T ~ 30 MK) and superhot (T ~ 100 MK) plasma in active regions on the Sun.

**7.4.2. SORENTO X-ray filters.** X-ray filters of the SORENTO play two main roles. First, they significantly decrease heating load of the instrument through reflecting and reradiating the incident radiation (mainly in optical and infrared spectral regions). The second assignment of this unit is reduction of low energy X-ray flow, which can result in pileup effect and changing the live time of detector. X-ray filter unit includes two beryllium windows placed in external and internal thermal shields of the Interhelioprobe SC with 2 and 1 mm thickness respectively (Fig. 16). Thermal shields are made of polycarbon. Their main function to prevent overheating of instruments due to the close distance to the Sun at perihelium (≈60 solar radii). The distance between inner shield and scientific instruments is 1000 mm. The external shield placed 305 mm higher than internal one.

**7.4.3. SORENTO Imager.** The lenses and mirrors cannot be successfully applied in the SORENTO telescope due to the high energy of registered emission. Therefore, indirect Fourier imaging is used like in HXT/YOHKOH (Kosugi et al., 1991) and RHESSI (Lin et al., 2002) telescopes.

**Table 10.** The main technical parameters of the TREK instrument

| Characteristics | HR | WF |
|---|---|---|
| Channels, Å | 171, 131 | 171/304, 8.42 |
| Spatial resolution, arcsec | 1.2 | 3.5 |
| Cadence, sec | 5–20 | 5–20 |
| Detector size, pix | 2048 × 2048 | 2048 × 2048 |
| Field of view, deg | 0.7 | 2 |
| Dimensions, $cm^3$ | 120 × 65 × 20 | |
| Total mass, kg | 15 | |
| Energy consumption, W | 20 | |
| Telemetry rate, MB/day | >100 | |

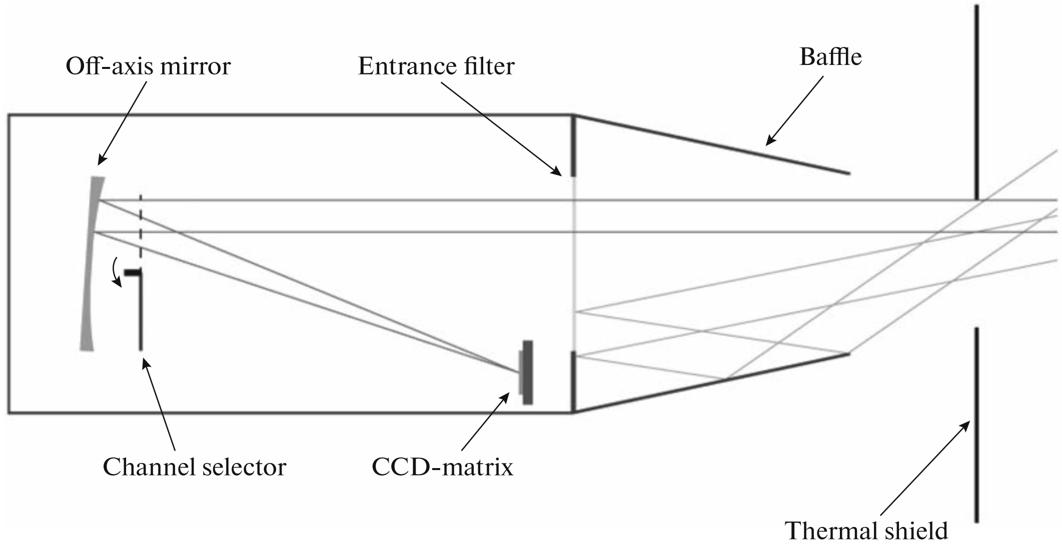

**Fig. 14.** Principal optical layout of the TREK WF-channels.

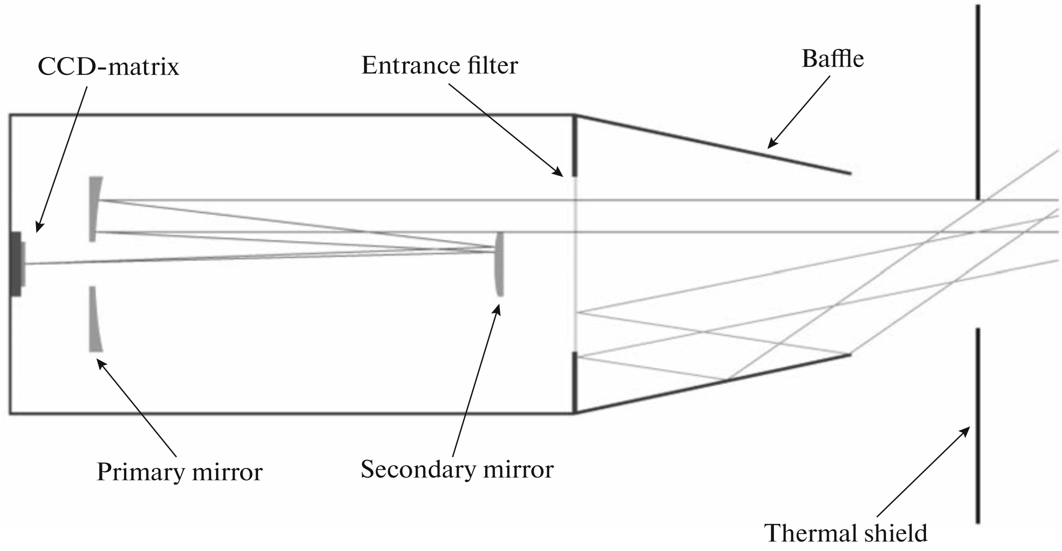

**Fig. 15.** Principal optical layout of the TREK HR-channels.

Imager module contains two sets of tungsten grids of 0.4 mm thickness at opposite ends of tube of 550 mm length (Figs. 16, 17) and the aspect system. Each set in turn consists of 32 subcollimators, which are located in front of corresponding detectors (Fig. 18). Subcollimator is a one-dimensional grid with equispaced slits and X-ray opaque slats. Pitches and orientation of rear and front subcollimators slightly differ that results in forming the Moire pattern on the detector. Detector has four main pixels, which measure time arrival and energy of photons. Pitches and orientation of grids are chosen to form one Fourier component of the source distribution after transmitting each subcollimator pair (Hurford et al., 2002).

**Table 11.** Main parameters of SORENTO

| | |
|---|---|
| Energy range, keV | 5–100 |
| Energy resolution, keV | 1 (FWHM at 5 keV) |
| Total mass, kg | 8 |
| Angular resolution, arcsec | 7 |
| Field of view, deg | 2 |
| Time resolution, sec | up to 0.1 |

The assignment of the aspect system of SORENTO is reducing the uncertainty in pointing on the Sun. It is a pin-hole camera with 4 diodes as a registration ele-

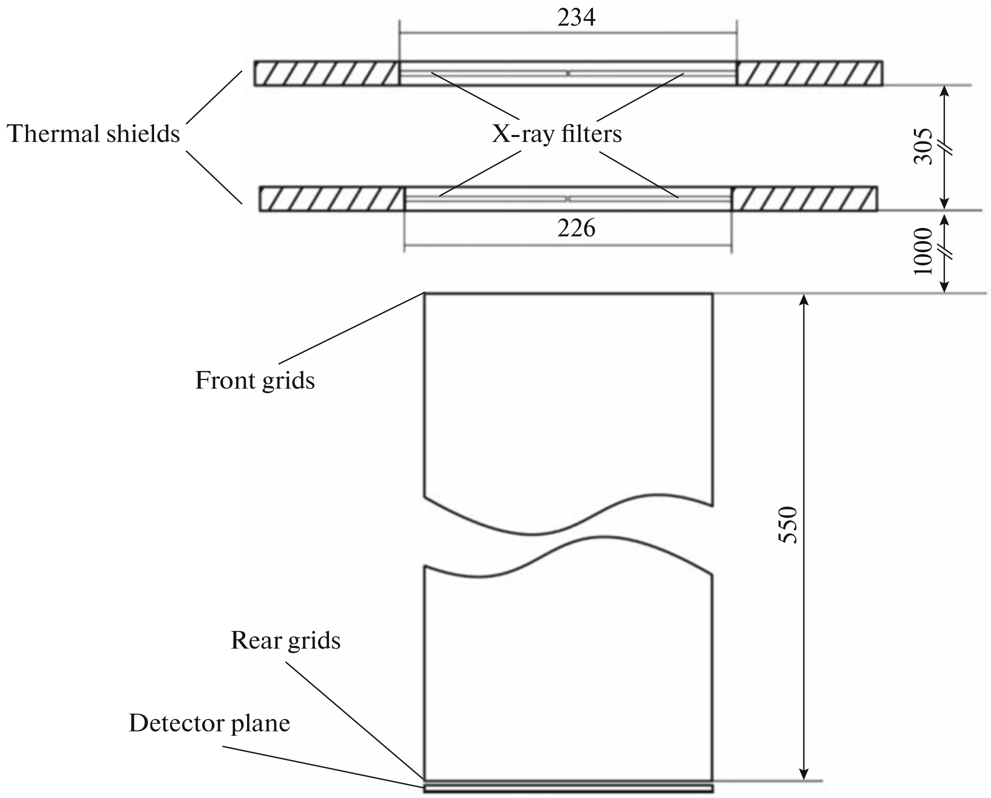

**Fig. 16.** Scheme of the solar X-ray telescope SORENTO. The X-ray filters of SORENTO are moved out of the instrument to the thermal shields.

ment. By measuring and comparing the signal on each of diodes one can obtain the position of Sun center.

**7.4.4. SORENTO detector unit.** Detector unit consists of the Detector box and the Instrument Data Processing Unit (IDPU). Detector box contains 32 CdTe semiconductor detectors with front-end electronics called Caliste-SO (Limousin et al., 2011; Michalowska et al., 2010). Each detector divided on 4 main pixels, which in turn consist of 3 small subpixels for reducing the effective area in case of high rates of incident photons. To decrease the part of low-energy photons in the spectrum aluminum attenuator is applied. It has two boundary positions – above the detectors and between them. It is moved mechanically by special shifting mechanism after receiving signal from the IDPU.

### *7.5. Side-looking OKA and HELIOSPHERA Coronagraphs*

To comprehensively study CME evolution, it is necessary to observe solar corona at all height ranges. All instrument assemblies, which investigate CMEs, try to make continuous observations from solar surface up to helioshepere, for example, the LASCO instrument onboard SOHO (Brueckner et al., 1995) or SECCHI onboard STEREO (Howard et al., 2008). Such observations allow to judge about CME acceleration mechanisms (Zhang et al., 2001) or changes in CME structure (Reva et al., 2014).

Side-looking coronagraph OKA is developed to register solar corona images on height 1.9–32.0 $R_S$ from the photosphere. The coronagraph is a part of a set of instruments, developed at Lebedev Physical Institute (LPI, Moscow), which are designed for continuous observations of the solar corona up to heights of 105 $R_S$. The TREK and SORENTO instruments will provide EUV and X-ray images of the solar disk with field-of-view FOV ≈ 2°, whereas OKA and HELIOSPHERA instruments will provide side-looking white-light images of the solar corona with total FOV ≈ 28°. Partial intersection of the FOV of different instruments allows to combine images and provide continuous observations (see Fig. 19). This gives an opportunity to continuously observe the corona from solar surface up to the height of 105 $R_S$.

**7.5.1. The OKA coronagraph.** The main scientific goals of the OKA coronagraph are:

—Investigation of the structure and dynamics of the far corona on height till 32 $R_S$;

—Ecliptic and non-ecliptic observation of the CME propagation on their early stages of the evolution;

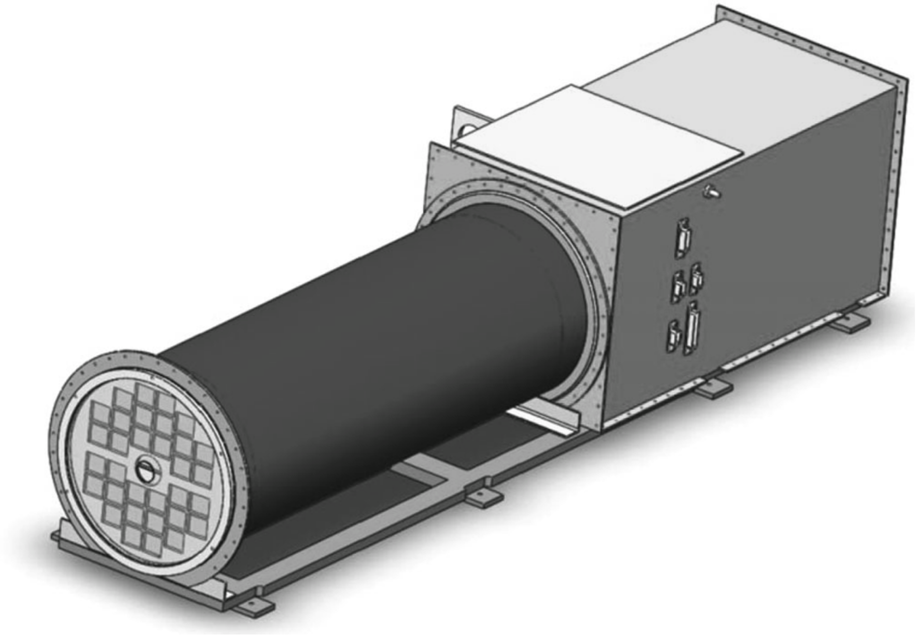

**Fig. 17.** The SORENTO imager with detector and electronic unit.

—Investigation of the mechanisms of the CME acceleration in the far corona and their interaction with solar wind and solar magnetic field;

—Joint observations with the instrument HELIOSPHERE of the structure and dynamics of the CME in the ecliptic plane with the total field of view from 0.5° to 28°.

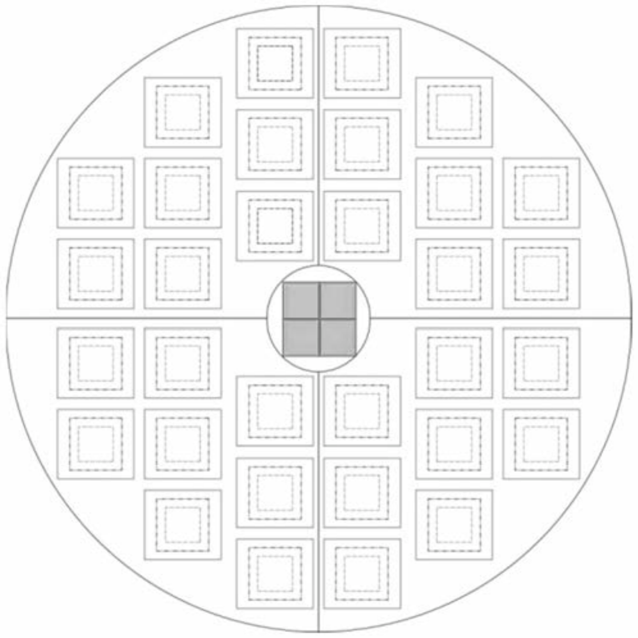

**Fig. 18.** The schematic top view of SORENTO imager and detectors. The outer squares (solid lines) correspond to front grids; middle (dot-dashed lines) – rear grids; inner squares (dashed lines) – detectors. Four squares in the center are diodes of the aspect system.

The side-looking layout, with respect to classical Lyot coronagraph with an artificial moon, will considerably simplify optical and mechanical design of the instrument. OKA will be installed in a shadow of the spacecraft thermal shield and inclined by 4.5° with respect of the spacecraft axis. A similar concept of side-looking coronagraph was realized in HI-1 and HI-2 cameras aboard STEREO (Eyles et al., 2009).

The OKA coronagraph consists of a light baffle, lens, CCD-detector and electronics (Fig. 20). The main challenges in developing the coronagraph are in developing objective from a radiation hardened glasses, developing of efficient baffle and detector under a tight mass budget. Main characteristics of the OKA instrument are summarized in Table 12.

Optical layout of the OKA lens is given in Fig. 21. The optical layout of the lenses is based on the telephoto layout. During the optimization a special attention was paid to the scattered light and ghost rejection. The RMS geometric spot radius is less than 10 mkm for the full FOV.

**7.5.2. The heliospheric imager HELIOSPHERA.** The side-looking coronagraph HELIOSPHERA is designed to register images of the far corona and heliosphere at heights of 30–105 $R_S$. Its main scientific goals are:

- Investigation of the structure and dynamics of the CME at heights from 30–105 $R_S$ above the solar surface;
- Non-ecliptic observations of CMEs;

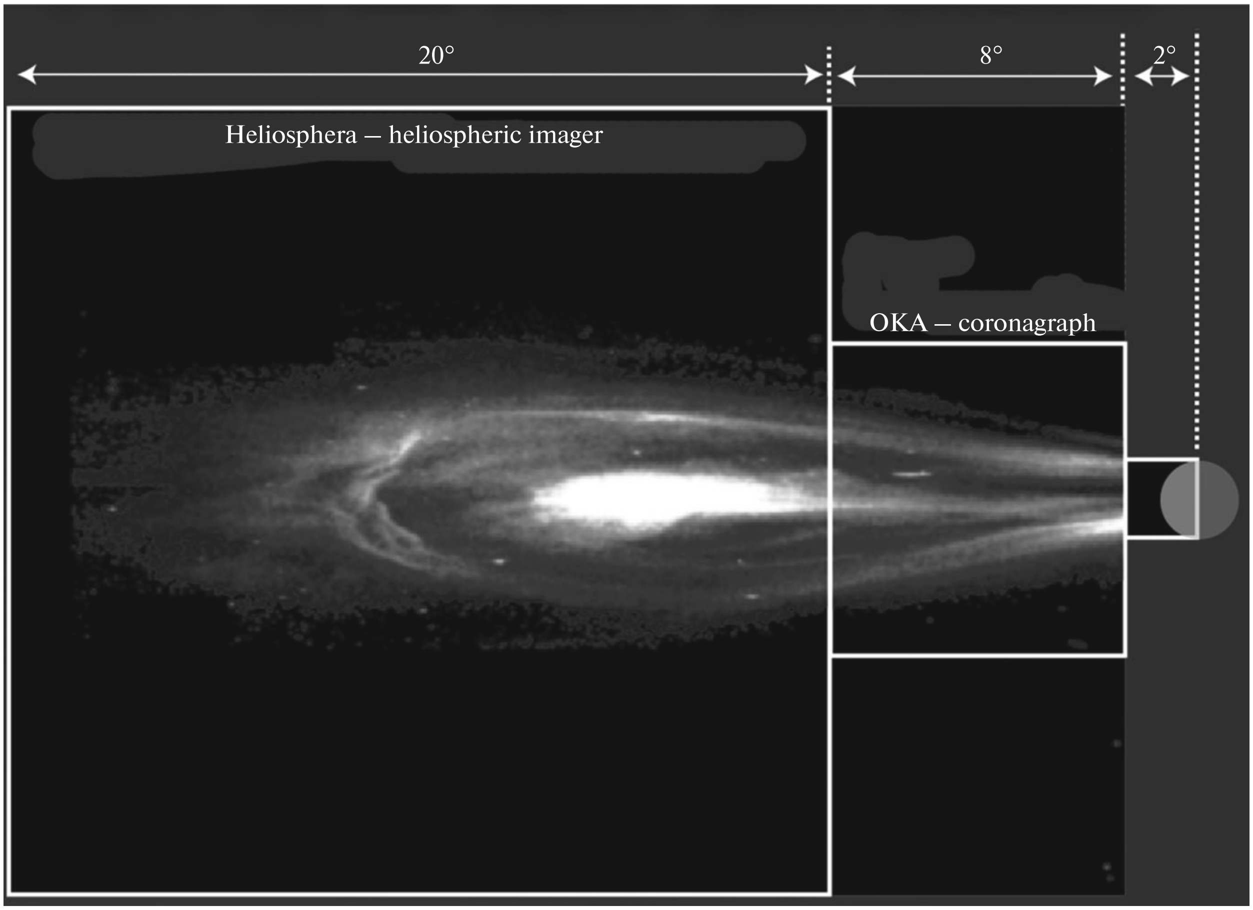

**Fig. 19.** Fields of view of the coronagraphs OKA and HELIOSPHERA, and the TREK telescope (right).

- Investigation of the mechanism of acceleration of CMEs and their interaction with solar wind, magnetic field and heliospheric plasma;

- Joint CME observations with the OKA coronagraph.

HELIOSPHERA will be installed in a shadow of the thermal shield and inclined by 18° with respect of the spacecraft axis.

The coronagraph consists of a light baffle, lenses, CCD-detector and electronics (Fig. 22). The main challenges in developing the coronagraph are in developing objective from a radiation hardened glasses, developing of efficient baffle and detector under a tight mass budget. Main characteristics of the instrument are summarized in Table 13.

Optical layout of the HELIOSPHERE lens is given in Fig. 23. Optical layout is based on the Tessar optical layout. The aperture is placed in front of the first element. A special attention was paid to the scattered light and ghost rejection of the lens. The RMS geometric spot radius is less than 16 mkm for the full FOV.

### *7.6. X-ray Spectrometer ChemiX*

ChemiX (chemical composition in X-rays) will constitute the advanced space X-ray spectrometer. In its construction the X-ray Dopplerometer principle will be for the first time combined with the bent crystal geometry of the Bragg reflection (Sylwester et al., 2015; Siarkowski et al., 2016). This will allow to study hot plasma motions in the absolute wavelength reference system, making in this way possible detailed verification of so-called evaporation scenarios related with flare energy release. Unique construction of ChemiX is presented below. Spectra to be collected will be used for purposes not only of the solar physics investigations, but also by specialists working in the field of atomic physics and plasma diagnostic, as the solar flare plasma thermodynamic characteristics resemble closely those of the fusion plasmas in Tokamaks and the other large Earth-based thermonuclear installations (Rice et al., 2014).

ChemiX is taking on a heritage from the many previous Bragg-spectrometry missions including the P78-1 (Doschek, 1983) by NRL USA, SMM XRP: FCS and BCS spectrometers (Acton et al., 1980), Hinotori Japanese mission (Akita et al., 1982), Yohkoh BCS (Cul-

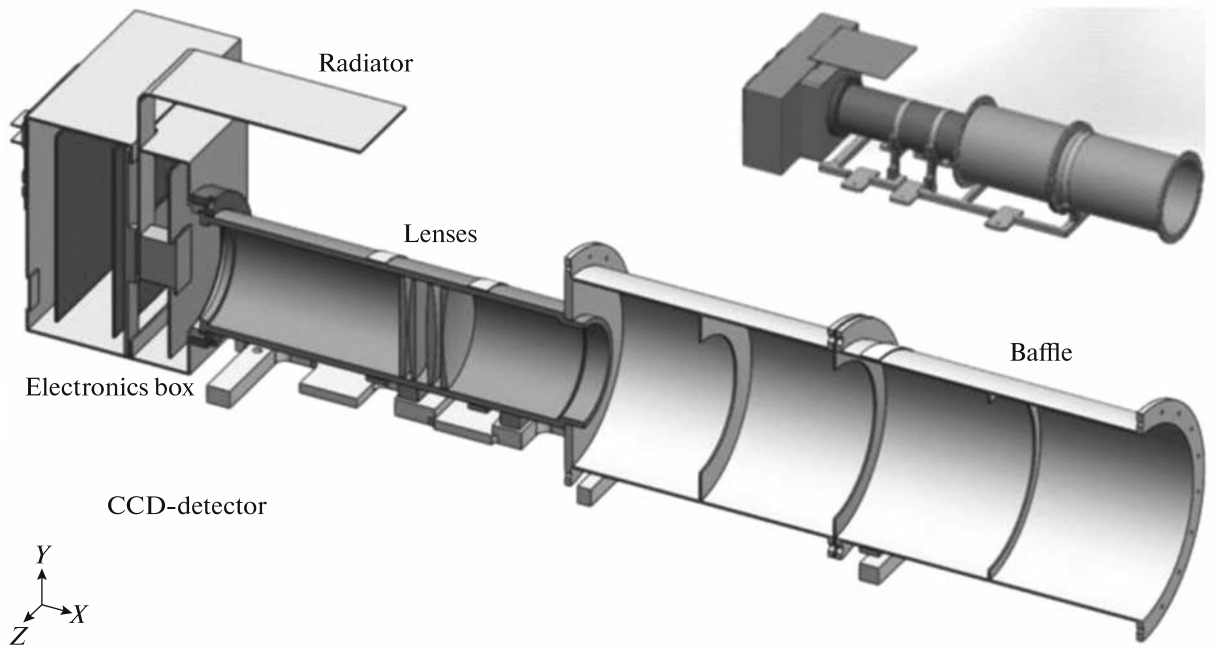

**Fig. 20.** Structural scheme of the OKA coronagraph.

hane et al., 1991) and finally RESIK (Sylwester et al., 2005) and DIOGENESS (Sylwester et al., 2015) aboard CORONAS-F. All those experiments were short of certain science outcome capabilities. ChemiX is intended to devoid of most of those shortcomings and represents the best at the time concept for the detailed diagnostics of the plasma state at the X-ray forming regions located in the solar corona. These regions of interest are the plasmas contained within the magnetic structures of non-flaring active regions (so-called coronal loops) and, in the first instance, flares—the most energetic phenomena observed within our solar system. ChemiX spectral observations will improve by at least a factor of 10 the spectral resolution and/or accuracy of the X-ray observations in the spectral range covered. There will be hundreds if not thousands of targets which will be observed by the instrument with unprecedented temporal and spectral resolution. These targets will be selected in-flight by the on-board computer performing on-line analysis of individual sources in the pin-hole images of the corona.

The use of cooled CCD detectors to record the spectra will result in at least 10-fold increase of the continuum-to-background signal, as compared with its predecessor RESIK. This will increase the accuracy of absolute abundance determinations by at least a factor of three, making in this way the X-ray solar plasma composition diagnostics the most precise ever. The knowledge of solar plasma abundances has a fundamental importance for astrophysics in the context of helio-seismology (Antia and Basu, 2006; Serenelli et al., 2009), FIP differentiation (Laming, 2009; Testa, 2010) and power radiation losses from plasmas. Com-

**Table 12.** Main characteristics of the OKA coronagraph

| | |
|---|---|
| Off-axis inclination, deg | 4.5 |
| FOV, deg | 8 |
| f, mm | 198 |
| f/D | 1/4.2 |
| CCD detector | e2v 42-40, 2048 × 2048 pix, 13.5 mkm/pixel |
| Weight, kg | 5 |
| Dimension, mm$^3$ | 590 × 160 × 235 |
| Telemetry, Mb/day | 100* |

* Actual telemetry is defined by downlink capacity. Telemetry can be shared between other LPI package instruments on a commands from BK-HOST (see Table 6).

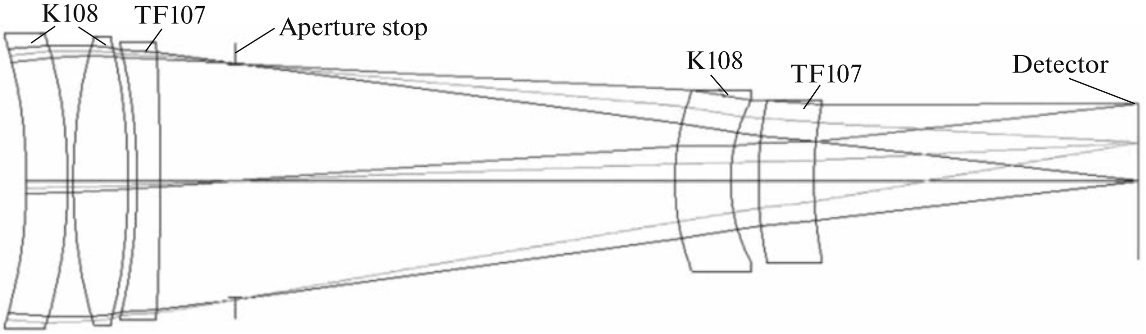

**Fig. 21.** Optical layout of the OKA coronagraph objective.

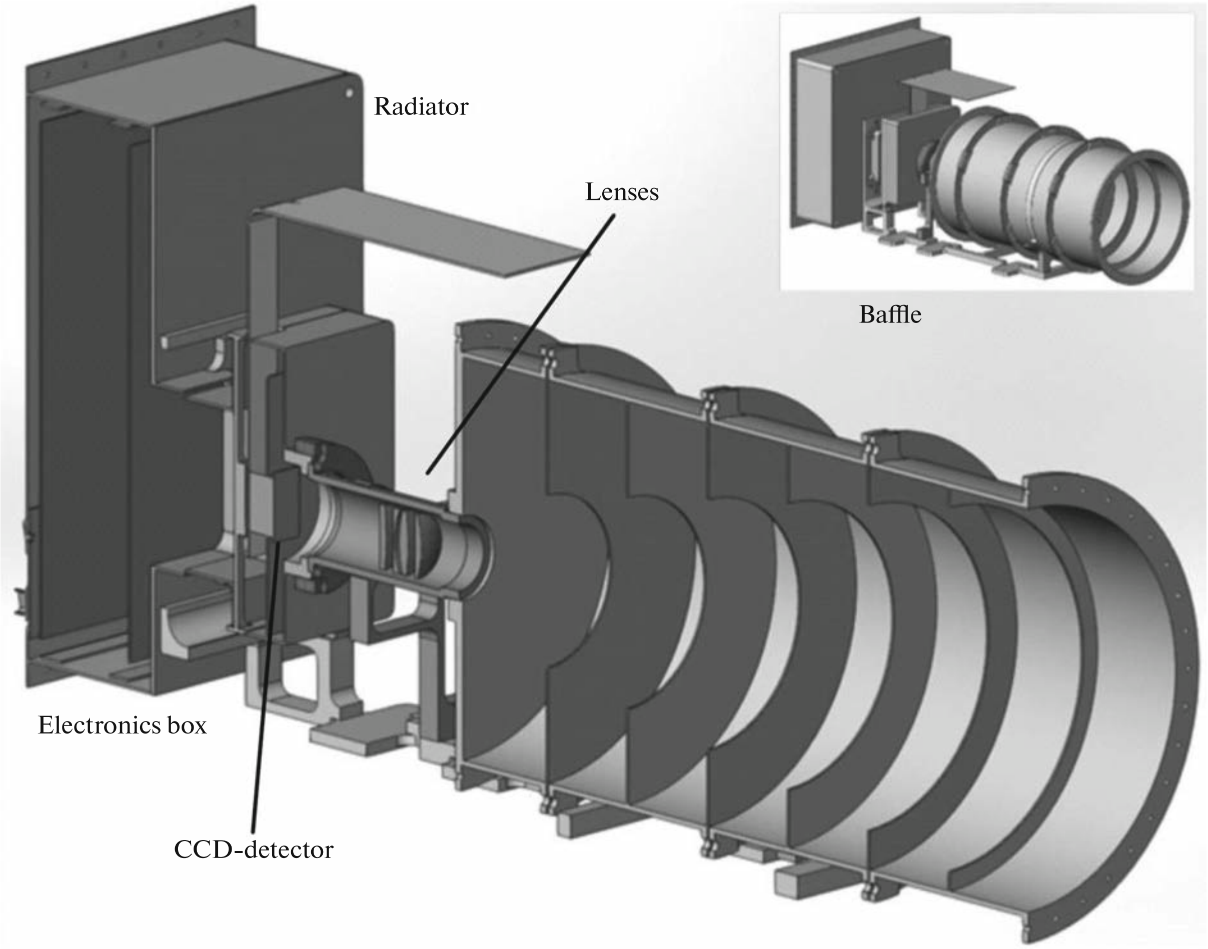

**Fig. 22.** Structural scheme of the HELIOSPHERA instrument.

plex studies of dielectronic line relative and absolute intensities will provide first-ever advanced diagnostics of the shape of energy distribution for electrons responsible for the line excitations in the most interesting physically energy range between 2–10 keV, where the character of X-ray emission is changing from thermal to non-thermal.

The main scientific goal of ChemiX is determination of elemental composition of solar coronal plasma X-ray bright structures based on the analysis of their high-resolution, collimated spectra. In the analysis of such spectra the most up-to-date versions of spectral software packages like CHIANTI will be used: http://www.chiantidatabase.org/. As a result it will be

**Table 13.** Main characteristics of the HELIOSPHERA instrument

| Characteristics | Values |
|---|---|
| Off-axis inclination, deg | 18 |
| FOV, deg | 20 |
| f, mm | 79 |
| f/D | 1/4.2 |
| CCD detector | e2v 42-40, 2048 × 2048 pix, 13.5 mkm/pixel |
| Weight, kg | 5 |
| Size, $mm^3$ | 490 × 240 × 250 |
| Telemetry, Mb/day | 100* |

* Actual telemetry is defined by downlink capacity. Telemetry can be shared between other LPI package instruments on a commands from BK-HOST (see Table 6)

possible to determine the individual elemental abundances with much greater precision than obtainable at present from analysis of photospheric or coronal spectra. In addition, the following quantities characterizing the physical conditions prevailing in individual coronal structures will be derived or determined: thermal (ion temperature) and turbulent line widths; directed plasma motions of key plasma constituents like Si, S, Ar, Ca, Fe; multi-temperature structure of the thermal plasma component will be studied, for the first time based on hundreds (not just tens, as at present) temperature sensitive lines, including transitions in multiple H- and He-like resonance line sequences extending to $n \sim 10$ spectral components; profile of the partial distribution function for exciters (electrons) in the range 2–10 keV in the source, thanks to the analysis of instant values of relative intensities of satellite lines formed in the resonance process of dielectronic excitations.

These measurements, made as function of time, and with the support of measurements from the other instruments aboard the Interhelioprobe, other spacecraft and ground-based observatories, will allow for the first time a complete and detailed approach to the solution of full energy balance equation for coronal plasma and unraveling basic processes of energy transfer from energy stored in coronal magnetic structures, to the non-thermal and thermal components which are manifested by high-energy radiation.

There is no other experiment planned for the next decade which may provide the observations of the quality and physical content envisaged for ChemiX.

**7.6.1. ChemiX construction.** Thanks to the proximity of the Sun, it is possible to build the bent crystal spectrometer much more compact and lighter in comparison with Earth-bound devices of similar designation. The design of the ChemiX has to comply with the requirements, described in respective Roskosmos document, more stringent than those necessary to accomplish space missions at the LEO. In particular, the instrument should survive in conditions of strong solar illumination, 10 times larger than at 1 AU distance. The instrument has to operate for not less than 5 years on the heliocentric orbit.

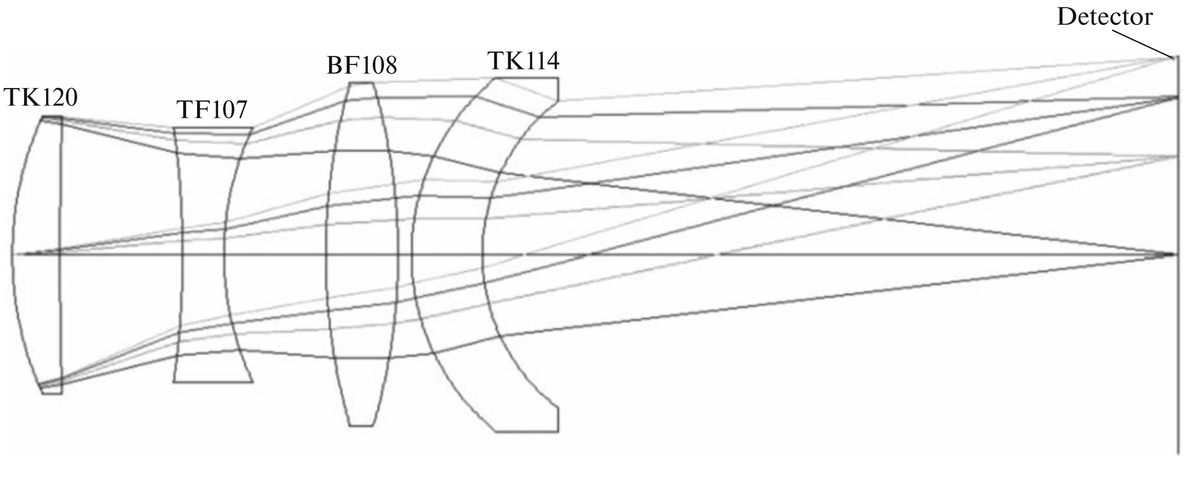

**Fig. 23.** Optical layout of the HELIOSPHERA coronagraph.

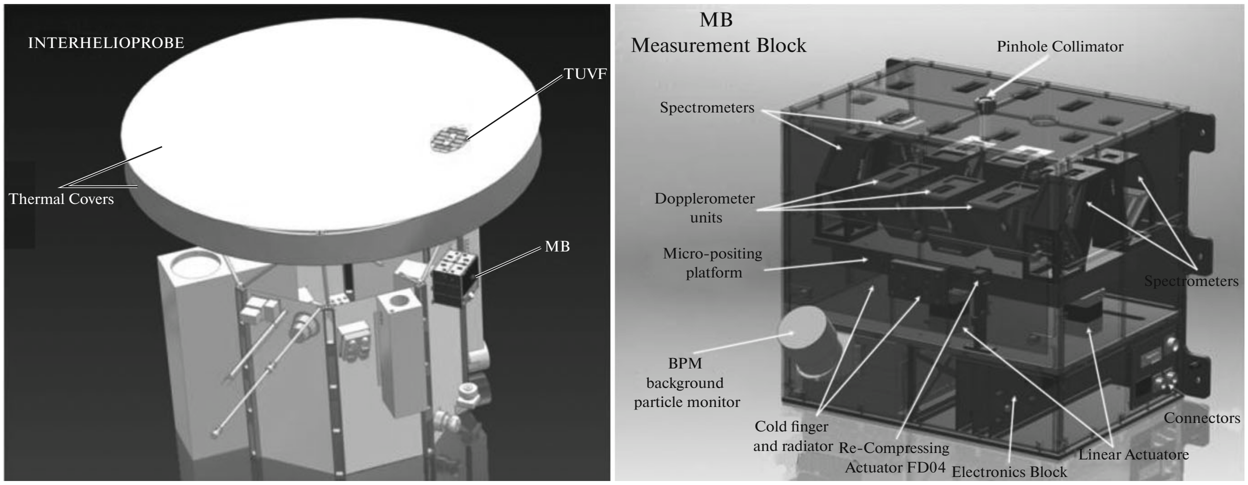

**Fig. 24.** Left: ChemiX measurement bloc (MB) placement on the Interhelioprobe spacecraft, behind the set of 11 soft X-ray filters (TUVF); Right: detailes of MB internal composition (see the text).

ChemiX is a convex, bent-crystal spectrometer under development at the Wrocław Solar Physics Division of the Polish Academy of Sciences Space Research Centre in collaboration with the international team (see Table 9). The instrument overall concept is presented in Fig. 24 and the spectral channel characteristics are given in Table 1. The total mass is 6 kg, size 30 × 30 × 32 cm$^3$, average power consumption 21.5 W and the telemetry rate above 20 MB/day.

Basic ChemiX construction elements are the following:

***Thermal shield and X-ray filters.*** They consist of two sections attached to front and rear planes of the spacecraft Thermal Shield. The main function of these two layers is to block the thermal load of solar radiation on the instrument and prevent the heat to penetrate down to the SC. Absorption in this shield limits the spectral range of ChemiX to wavelengths below ~0.9 nm (9 Å);

***A system of 2D capillary collimators.*** Their main function is to limit the field of view (FOV of ~3 arcmin$^2$) of solar X-ray illumination to (pre)selected portion of the solar disk, i.e. an active region or flare;

***The pin-hole imager*** with the aperture of the order of 1 mm$^2$ which projects the real-time X-ray solar image on the CCD. Images will have intrinsic resolution of few arc-minutes, enough to distinguish emission formed within particular active region of the corona and to see X-ray limb brightening. The images, to be analyzed by the instrument processor, will allow to locate ROI, usually the brightest region in the corona over the disk. Flags will be passed to the motor which will point entire spectrometer towards ROI;

***The four sections of spectrometer.*** These four sections cover the spectral range from ≈1.5 Å to 9 Å in approximately four thousands spectral channels provided by rectangular 256 × 1024 CCD's with pixels of 26 × 26 micron size. Each CCD will be illuminated by X-rays diffracted from selected mono-crystal wafers (see Table 14) bent cylindrically to a desired radius of curvature;

***Three double sections of Dopplerometer,*** each equipped with identical crystal wafers with opposite sense of dispersion. These three sections will allow for precise measurements of emission line absolute Doppler-shifts and profiles;

The very important role plays ***the background particle monitor system*** developed fully in Kharkiv, Ukraine. This will consist of a special design of PIN Si wafers and scintillators placed next to the MPPCs. The system will monitor fluence of charged particles (electrons and protons) that may arise from clouds of solar energetic particles (SEP) accompanying larger flares. The flux of those particles can reach such a high levels that it would be necessary to switch off entire instrument, to prevent the damage to the detectors.

ChemiX will be controlled by the on-board computer, connected to SC telemetry SSNI (see Table 6). The instrument electronics will be based on FPGA technology. The computer will activate the motors of the pointing platform, issue flare flags, compress and format the data. A large memory buffer (up to 512 GB) will be installed to store all registered detectors events history including the arrival time and the signal charge. Pre-selected parts from this data bank will be downlink to the ground when telemetry contact allows for faster transmission rates.

The instrument will have a special arm equipped with the Fe$^{55}$ radioactive source, which will allow for the calibration of the CCD "flat-field" response during entire mission duration. The instrument will be always "on", except for initial outgassing and periods of SEP or CME crossings. Substantial "operational autonomy" will be provided at periods where limited

**Table 14.** ChemiX spectral channels

| Channel no. | Crystal | Diffracting plane | 2d, Å | Wavelength range, Å | Average spectral resolution, mÅ/pix | Number of crystals |
|---|---|---|---|---|---|---|
| Spectrometer channels | | | | | | |
| 1 | Si | 111 | 6.271 | 1.500–2.713 | 1.41 | 1 |
| 2 | Quartz | $10\bar{1}0$ | 8.514 | 2.700–4.304 | 1.82 | 1 |
| 3 | KDP | 011 | 10.185 | 4.290–5.228 | 0.98 | 1 |
| 4 | KAP | 001 | 26.64 | 5.200–8.800 | 4.2 | 1 |
| Dopplerometer channels | | | | | | |
| 1 | LiF | 022 | 2.848 | 1.835–1.949 | 0.12 | 2 |
| 2 | Si | 111 | 6.271 | 3.150–3.324 | 0.11 | 2 |
| 3 | Si | 111 | 6.271 | 3.900–4.080 | 0.19 | 2 |

connectivity from Earth to the spacecraft will be available (particularly, when the SC will be close or behind the Sun) as seen from Earth.

**7.6.2. ChemiX spectra.** Spectral atlases consisting of full spectral scans over the entire 1.5–9 Å range will be taken while the instrument is directed at particular sources with a user-chosen intensity level (e.g. a total of 10000 photon counts over the spectrum). Spectral line and continuum fluxes will be obtained with unprecedented precision, especially when the spacecraft is at perihelion, about 0.3 AU from the Sun. An example of the spectrum arising on one of the Dopplerometer channels (no. 3) is presented in Fig. 25.

**7.6.3. Summary.** The ChemiX instrument on the forthcoming Russian Interhelioprobe spacecraft, will be launched into elliptical orbits after 2025. The instrument will have four channels viewing Fe xxv, Ca xix, S xv, Si xiii and Si xiv lines as well as lines of Mg and Al with a full coverage of the 1.5–9 Å range. The diffracting crystals will be arranged in a dopplerometer manner as for DIOGENESS but will be bent and non-moving. The use of cooled CCD detectors will give much better spectral resolution over the RESIK spectrometer on CORONAS-F which had position-sensitive proportional counters. A collimator will allow the emission from individual active regions to be observed.

### *7.7. Hard X-ray Polarimeter PING-M*

One of the most important tasks of solar physics is the detailed investigation of plasma heating and charged particles acceleration mechanisms during solar flares. Electron acceleration mechanism parameters can be studied by means of investigation of accelerated electrons spectra and electron angular distributions. The spectrum of the accelerated electrons can be obtained by measuring the bremsstrahlung hard x-ray spectrum of solar flare. To obtain the angular distribution of accelerated electrons one has to measure linear polarization degree of hard x-rays. Also, hard x-ray energy spectrum measurement can make the results interpretation more reliable because the polarization degree strongly depends on three parameters: the angular distribution of accelerated electrons, the spectrum of these electrons and the observation angle of a flare.

The predicted linear polarization degree can vary from several per cent up to 60 per cent depending on parameters of particular angular distribution. Linear polarization degree was measured only for several solar flares. However, statistic accuracy of most of these measurements is insufficient and all collected data cannot be described by the common flare loop model (Kotov, 2010).

The Interhelioprobe orbit will allow stereoscopic observations if the similar instrument be installed on a near Earth satellite. Also, if the launch of the second similar mission be realized during the operation period of the first mission, stereoscopic observation will be performed by identical instruments in the frame of one project.

Thermal processes in solar flares generate soft x-ray emission with thermal or quasi thermal spectrum. The main parameters of this spectrum are the temperature and the emission measure. These parameters are usually obtained by means of the GOES measurements in the two broad channels. But, there are many evidences of multi-temperature nature of the emission region. High resolution spectral measurements in the energy range 1–20 keV are necessary for the multi-temperature radiation spectrum analysis. Temperature measurements are also possible by means of intensity and width of Fe and Fe/Ni lines (6.7 keV and 8.0 keV correspondingly) investigation in case when the energy resolution of the detector is better than 250 eV in the energy range 3–10 keV.

**7.7.1. The scientific tasks of PING-M experiment.**

- Polarization degree measurements in 18–150 keV energy range.

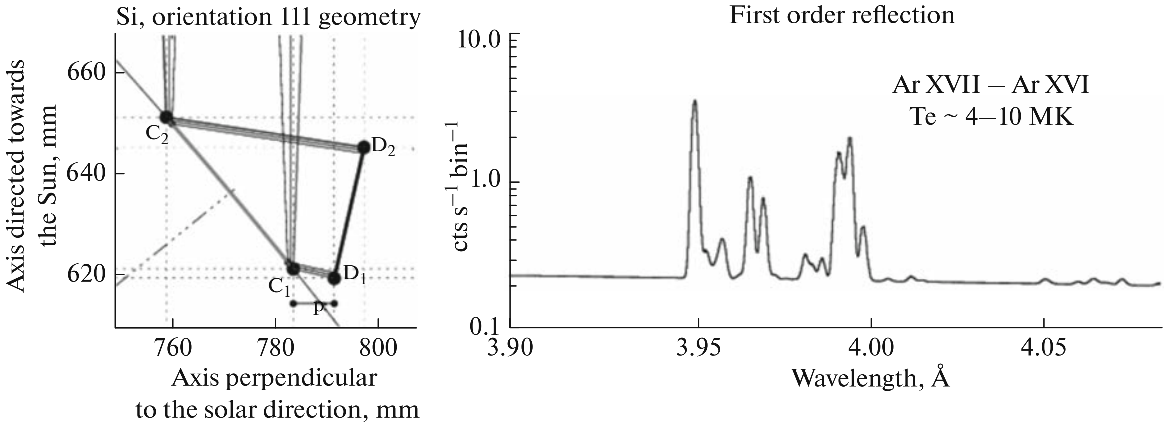

**Fig. 25.** Left: Scheme of crystal diffraction for dopplerometer channels 3 (Ar XVII) and (right) resulting spectra (simulated for a GOES M5 flare using the CHIANTI database and software package). Solar X-rays are incident from the figure top on the crystal, are diffracted by the crystals ($C_1$–$C_2$) and then are incident on the CCD detectors ($D_1$–$D_2$).

- Hard x-ray spectra of solar flares measurements in the energy range 20–600 keV with the energy resolution better than 4.5% at 662 keV line.

- High resolution measurements of solar flares soft x-ray spectra in the energy range 1.5–25 keV with the energy resolution better than 200 eV at 6.9 keV line and solar flare classification with the GOES scale during the Interhelioprobe mission.

**7.7.2. PING-M instrument description.** The instrument PING-M consists of two units: PING-P (hard X-ray polarimeter) and PING-PIRS (precise x-ray spectrometer). The spectrometer unit consists of two detectors: the soft X-ray spectrometer (SXRS) and the hard X-ray spectrometer (HXRS). Both units include front-end and processing electronics. Power supply and interface modules, which provide communication with the satellite systems BUS and SSNI, are common for the both blocks and placed in PING-PIRS unit.

To obtain X-ray linear polarization degree PING-P polarimeter measures angular distribution of scattered photons. Anisotropy of this distribution strongly depends on polarization degree of incident photons, and orientation of the anisotropy is perpendicular with polarization plane of the incident beam. Three p-terphenyl ∅36 × 30 mm scintillators are used as active scatterers of the incident photons. These scatterers register in coincidence with detectors of scattered photons made of CsI(Tl) (∅45 × 5 mm, 6 units). The active scatterers and the coincidence system allow the polarimeter to reduce its background. The expected background count rate of each detector during flight is about $10^2$ $s^{-1}$, while count rate of false double coincidence is about $10^{-1}$ $s^{-1}$. The scheme of the polarimeter assembly is represented in Fig. 26.

PING-P provides polarization measurements in the energy range 18–150 keV. Effective area of the polarimeter is about 2.5 $cm^2$ in its operation energy range. The minimal measurable degree of polarization is about 1.0% for 100 sec exposition of X1 solar flare. The main aspect which determines polarimeter sensitivity (the minimal polarization degree that can be registered) is uniformity of the detectors. PING-P uses onboard $^{129}$I and $^{241}$Am isotopes for periodic calibration of the scatterers and the detectors of scattered photons correspondingly and on-line LED stabilizer for both types of detectors.

HXRS operates in the energy range 20–600 keV. The detector is based on a fast inorganic scintillator ∅5 × 2.54 cm with high light yield ($LaBr_3$(Ce) or $CeBr_3$ crystals). $LaBr_3$(Ce) has better energy resolution (3% at 662 keV versus 4% for the second one) but it has much higher intrinsic activity in comparison to $CeBr_3$.

The spectrometer SXRS is based on a relatively novel type of semiconductor detector SDD (Silicon Drift Detector), that will operate in the energy range 1.5–25 keV, which is similar to region of GOES X-Ray Sensor (XRS). The SDD is cooled down to −30°C by incorporated Peltier element. Unlike GOES the SXRD is capable to measure the energy of each photon in the mentioned band with high resolution (better than 200 eV at 5.9 keV). To correct the effects of signal overlapping fast intensimeters are used to measure counting rates in three energy bands: >0.9, 1.55–6.2; 6.2–12.4 keV. The minimum and the maximum fluxes measured by the detector correspond to B1 and X10 solar flare classes of the GOES scale. The scheme of PING-PIRS unit is represented in Fig. 27. The main characteristics of PING-M instruments are represented in Table 15.

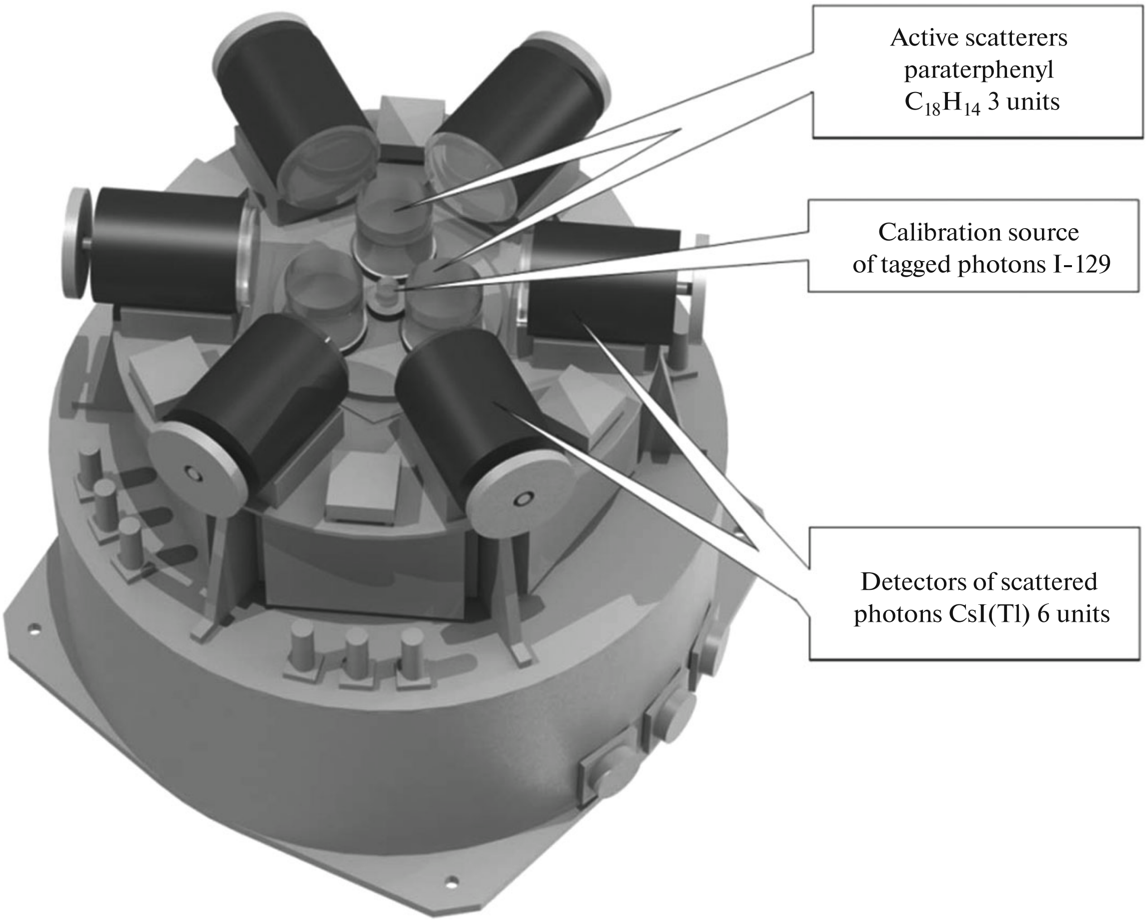

**Fig. 26.** PING-P unit.

### *7.8. Scintillation Gamma-spectrometer HELIKON-I*

Fundamental problems of solar physics, studied by X-ray and gamma-ray astronomy, are: acceleration of the electron component of flare plasma, acceleration of the nuclear component of flare plasma, heating of the corona and flare plasma. In addition, detailed spectral data contain information on such important physical processes as a non-uniform ionization of the chromosphere, reverse currents and albedo of the photosphere. Experiment with the HELIKON-I instrument as part of the Interhelioprobe mission is intended for comprehensive studies of temporal profiles and energy spectra of hard X-ray and gamma-ray solar flares in a broad energy range from 10 keV to 15 MeV, in a wide range of flare durations from a few milliseconds to tens of minutes and in a wide range of intensities of events from microflares to powerful X-class flares.

**7.8.1. Scientific goals of the HELIKON-I experiment.** The scientific goals of HELIKON-I include:

—studying heating processes of the solar corona. Detection of radiation in the 10 keV – 15 MeV range allows registering the ‘tail’ of the thermal component of the radiation, the transition region between thermal and non-thermal components and a non-thermal component. Sensitivity of HELIKON-I’s detector in combination with the SC orbit being close to the Sun will provide accurate measurements of non-thermal component, while measurements in the X-ray range with other instruments of the mission (ChemiX, SORENTO, PING-M) will provide detection with good spectral resolution of the thermal spectrum component and cross-calibration of instruments in the region of low-energy X-ray radiation;

—studying the processes of electron acceleration in solar flares. Determination of the spectra of electrons accelerated in flares in the spatio-temporal dynamics is a key to understand the processes of particle acceleration in the solar corona, as well as in a broader astrophysical context. In this regard, the ability of the HELIKON-I instrument to measure X-ray spectra at high energies – above 100 keV – will be of fundamental significance in the joint analysis of data from X-ray and microwave range, as microwave radiation is generated primarily by electrons with energies above 100 keV. It is important to bear in mind that by the time Interhelioprobe is launched there will be several ground-based multi-frequency radio interferometers of a new generation, such as improved SSRT (Russia), EOVSA (USA), CSRT (China), and, possibly, a super instrument FASR (USA). Therefore, extra information about the spectra of electrons in the region of hundreds of keV, that HELIKON-I will supply, is absolutely invaluable;

—determination of the cut-off energy of the electron spectrum of solar flares in the low energy region and its evolution during flares in order to determine the total energy of non-thermal electrons and efficiency of acceleration processes;

—studying the processes of ion acceleration in solar flares. Spectroscopy of nuclear gamma-ray lines, most of which lies in the range ≈0.5–8 MeV, is an important tool to study the abundance of different elements in the solar chromosphere and the upper photosphere (narrow lines) and in the population of accelerated nuclei (broad lines). It gives the opportunity to determine the spectrum of the accelerated ions and the total energy contained in them. HELIKON-I has in this energy range an effective area greater than that of RHESSI and energy resolution sufficient for the analysis of intense lines;

—studying the energy distribution between components of solar flares. Comparison of the energy contained in accelerated electrons and ions gives, in turn, an unique opportunity to understand one of the key issues on the energy distribution between the accelerated electrons and ions and acceleration processes of each of these particle species. Furthermore, analysis of gamma-ray lines may give constraints on magnetic loop parameters. In this matter, a joint analysis of X-ray and gamma-ray data on the one hand and microwave data on the other hand is of paramount importance;

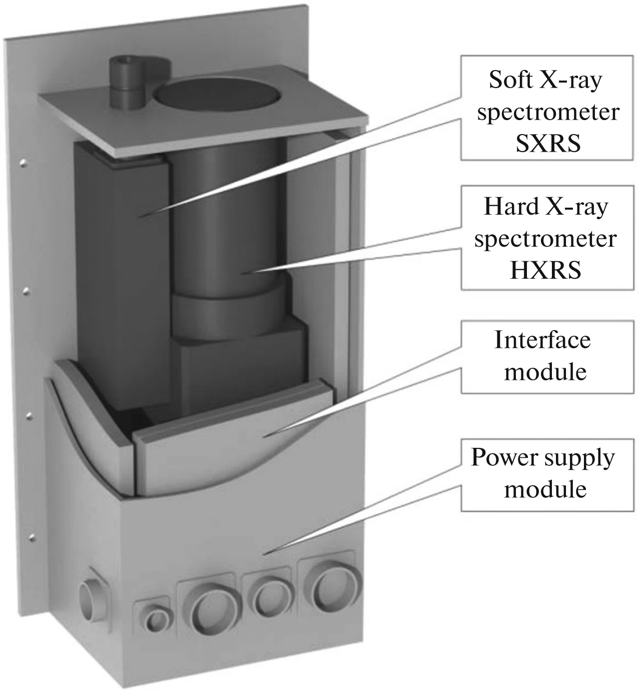

**Fig. 27.** PING-PIRS unit.

—studying cosmic gamma-ray bursts and soft gamma repeaters. An additional scientific goal of the HELIKON-I experiment is the study of time profiles, energy spectra and a rapid spectral variability of cosmic gamma-ray bursts and soft gamma repeaters as sources of extreme flows of electromagnetic energy.

**Table 15.** PING-M characteristics

| **PING-P** | |
|---|---|
| Operational energy range, keV | 18–150 |
| Effective area, cm$^2$ | about 2.5 |
| Maximum systematic error of the polarization measurements, % | 1 |
| Mass of the unit, kg | 10 |
| Power consumption, W | 12 |
| Dimensions, mm$^3$ | 325 × 360 × 395 |
| **PING-PIRS** | |
| Operational energy range of the hard x-ray spectrometer, keV | 20–600 |
| Energy resolution of the hard x-ray spectrometer at 662 keV, % | 3.5–4.5 |
| Effective area of the hard x-ray spectrometer, cm$^2$ | 10–20 |
| Operational energy range of the soft x-ray spectrometer, keV | 1.5–25 |
| Energy resolution of the soft x-ray spectrometer at 5.9 keV, eV | <200 |
| Mass of the unit, kg | 3.5 |
| Power consumption, W | 7.5 |
| Dimensions, mm$^3$ | 170 × 120 × 320 |

The Intergelioprobe spacecraft will approach the Sun up to $60R_S$ (0.3 AU), thus X-ray and gamma-ray radiation fluxes increase approximately 10 times in comparison with fluxes in Earth orbit. This will allow studying thoroughly the dynamics of non-thermal continuum emission of a large number of relatively weak solar flares and the dynamics of gamma-ray lines with good temporal resolution in the spectra of strong and moderately intense flares.

**7.8.2. Brief description of the HELIKON-I instrument.** To solve the above stated scientific problems in the HELIKON-I instrument we plan to use a scintillation gamma-ray spectrometer, which contains a NaI(Tl) crystal with a diameter of 130 mm and a height of 76 mm, placed in a thin-walled aluminum container with a beryllium entrance window and the output window made of high transparency lead glass to protect the detector from the background radiation coming from spacecraft in soft range.

Schematic representation of the device is shown in Fig. 28. The preliminary dimensions of the HELIKON-I instrument is the following: the diameter is 200 mm, the length is 361 mm. The weight of the HELIKON-I instrument is 10.5 kg, average power consumption is less than 5W, the information yield of the instrument is 200 MB/day.

The spectrometer provides a low-energy threshold of detection from 10 keV, the range of gamma-ray quanta detection up to 15 MeV with an energy resolution of about 8% on the reference line 660 keV (isotope $^{137}$Cs) and sensitivity of detection about $10^{-7}$ erg cm$^{-2}$. In the width of energy range and the degree of protection from the background of SC and surrounding structures, single-crystal gamma-ray spectrometer HELIKON-I has no analogues in Russian and foreign scientific equipment for registering X-ray and gamma-ray bursts. The prototype of the HELIKON-I gamma-ray spectrometer is the KONUS-WIND spectrometer, which has been operating for 20 years with a high scientific output as part of the NASA spacecraft Wind (Aptekar et al., 1995), as well as gamma-ray spectrometers Konus-A, Helikon and Konus-RF, having successfully conducted observations of solar flares and gamma-ray bursts on Russian spacecraft series Cosmos and Coronas (Aptekar et al., 2010; Mazets et al., 2012; Mazets et al., 2014).

**7.8.3. Brief description of the HELIKON-I monitoring modes.** Solar flares of hard X-ray and gamma-ray radiation and gamma-ray bursts are rare occurrences of photon count excess above the background level, the time of event is not known in advance. The duration of a flare may vary from a few milliseconds to tens and hundreds or thousands of seconds. Therefore, the measurement program of the HELIKON-I instrument is primarily focused on detailed continuous registration of the background level. This operation mode is called a background mode. In this mode, the radiation is registered continuously in two energy bands, covering energy from 10 keV to 15 MeV, each of which is divided into a number of energy windows, the accumulation time is adjustable by means of digital commands. Simultaneously with the registration of X-ray and gamma-ray light curves in the background mode, energy spectra are measured in two bands using 256 channel analyzers with quasilogarithmic scale, the accumulation time of the spectra can also be controlled by digital commands. Also in the background mode registration of charged particles is conducted, they are detected by energy release exceeding 15 MeV in a scintillation crystal. Information gathered in the background mode allows making in flight calibration of the scintillation spectrometer by the lines of natural and induced radiation activity and studying in detail burst precursors, weak subthreshold spikes and other unusual phenomena in the background cosmic X-ray and gamma-ray radiation.

Transition of the HELIKON-I instrument to flare mode, at which recording of X-ray and gamma-ray radiation begins with significantly greater detail, is done automatically as soon as the number of gamma-ray quanta in the selected energy window exceeds a predetermined level. In the flare mode time histories are measured in the same energy windows in two bands with significantly higher time resolution from a few milliseconds and the total duration of the record of a few hundred seconds, which will also be adjusted by means of digital commands. At the same time, energy spectra are registered in two energy bands with 264 channels per band and spectrum accumulation time is set automatically by a special adaptive system depending on the intensity of flare radiation. The total number of the energy spectra is 4096. Particular attention is paid to the initial registration phase of flare events. The measurement program of the HELIKON-I instrument in the burst mode provides 2 seconds long registration of event pre-history, and in the most intense parts of flare it provides time tagged event mode with a maximum time resolution of about 1–2 microseconds. This mode provides for fixing the arrival time of each photon coming from a flare and was named TTE regime for English transcription of words “time-tagged events”. RAM for the TTE mode is expected to store 500 thousand photonic events for each flare. The information gathered in the flare mode allows detailed studying of the temporal structure of flares and bursts, determining the delay of flare radiation light curves at different energies, searching for periodicities in flare radiation, studying the spectral variability on millisecond scale and conducting joint spectral analysis of flares and gamma-ray bursts registered with several SC.

To expand the capabilities of the HELIKON-I instrument a replacement of NaI(Tl) scintillation crystal to a new lanthanum bromide scintillation crystal is considered. Its major advantage is significantly less, almost 2 orders of magnitude, decay time. It allows for linear measurement circuits of spectrometer with ultra-low ‘dead time’ reaching 2–3 microsec-

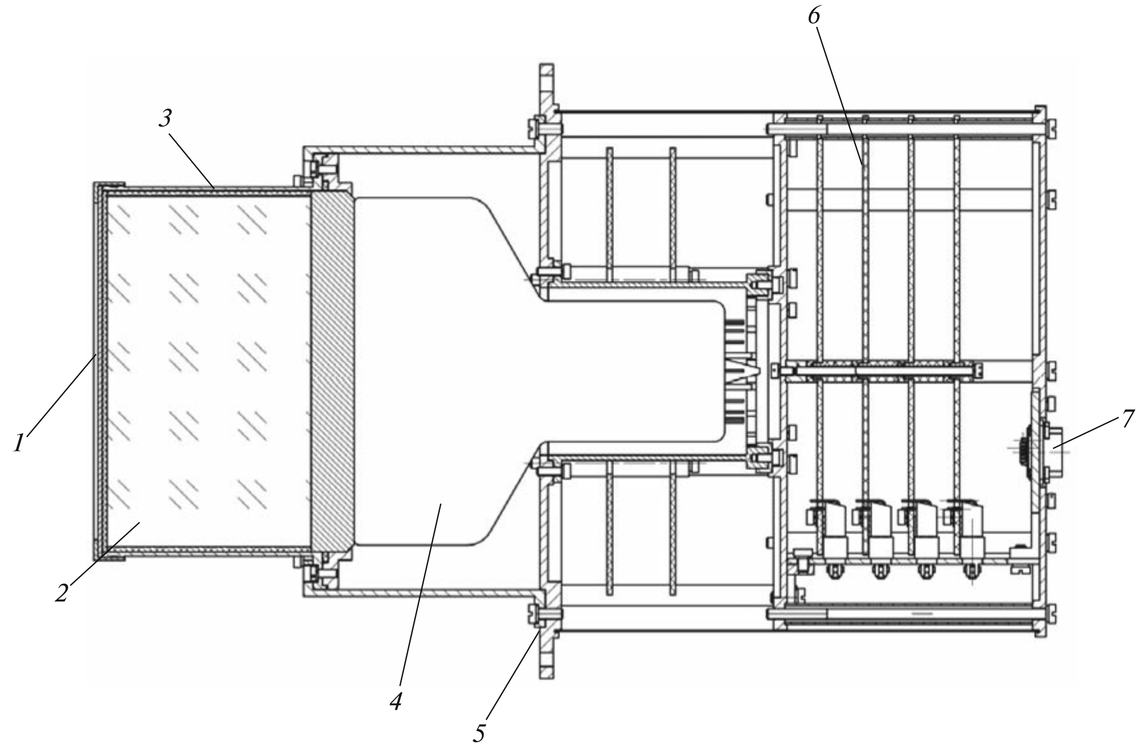

**Fig. 28.** Design scheme of the HELIKON-I instrument: (*1*) beryllium entrance window; (*2*) scintillation crystal; (*3*) crystal container of aluminum; (*4*) photomultiplier FEU-167; (*5*) seat flange of the unit, (*6*) electronic boards, (*7*) connectors to on-board systems.

onds. As shown by many years of the Konus-Wind experiment experience it is extremely important for observations of intense solar flares and huge bursts of gamma-repeaters. A linear chains with scintillators based on sodium iodide are completely saturated for the period of registration of the main phase for such events. The second important advantage of the new scintillation crystal is a much higher energy resolution of 3% at the reference line $^{137}$Cs. This is very promising for the spectroscopy of nuclear gamma-ray lines of solar flares.

It is planned that the experiment with the HELIKON-I instrument should be carried out continuously during the entire time of active operation of the Intergelioprobe mission. The details of the measurement program for flare events and the possibility of changes in the course of the experiment with the help of digital commands will be updated in next stages of development of the HELIKON-I instrument.

### *7.9. Gas Gamma-ray Spectrometer SIGNAL*

SIGNAL is another gamma-ray experiment within the Interhelioprobe mission. Its core is a xenon gamma-spectrometer. This spectrometer is chosen because of its characteristics permitting detailed probing of solar gamma-radiation under rough experimental conditions. The equipment is able to provide: high energy resolution (5–6-fold better than that of scintillation detectors), performance at high temperatures, steady operation at significant vibroacoustic load, and high radiation resistance of working substance. The aforesaid properties of the xenon gamma-ray spectrometer meet goals and objectives of the experiment SIGNAL.

**7.9.1. Scientific objectives of the SIGNAL experiment. 1.** *Gamma-ray line radiation and continuum study over the energy range from 30 keV to 5 MeV in solar flares. In particular, it will be possible to investigate:*

—$^7$Be and $^7$Li nuclei proportion, $^4$He(α, *n*)$^7$Be* and $^4$He(α, *p*)$^7$Li* forming in the nuclear reaction, accelerated α-particle fluxes in the solar atmosphere, as well as angular anisotropy extent of α- particle motion;

—certain γ-ray lines intensity to determine various nuclei quantitative composition such as, $^{56}$Fe (0.84 and 1.24 MeV), $^{24}$Mg (1.37 MeV), $^{20}$Ne (1.63 MeV), $^{28}$Si (1.78 MeV), $^{12}$C (1.99 and 4.43 MeV ), and $^{14}$N (2.31 MeV) in the solar atmosphere;

—intensity of γ-ray line 2.22 MeV for study of light elements solar fusion processes. This γ-ray line is emanated at thermal neutrons capture by protons or by $^3$He generating deuterium or tritium correspondently. The γ-ray line intensity contains unique information about $^3$He concentration, which will help peep in subphotosphere of the Sun;

—solar atmosphere temperature magnitude over the width of γ-ray line 0.511 keV, as its width is dependent on temperature as $T^{1/2}$;

—particle acceleration processes in solar flares, by means of measurement of their time profiles and γ-ray lines intensity ratio over various energy ranges;

—concentration of $^3$He during solar flares according to the γ-ray line intensity measurement data, occurring in $^3$He direct reaction (0.937, 1.04 and 1.08 MeV);

—gamma-ray emission of week class (B and C) solar flares, which permits to study of spectrum continuum shape in detail as well as determination of the range where nonthermal component starts to prevail;

**2.** *Research of galactic and metagalactic gamma ray bursts (GRBs). Results to be obtained are:*

—fluxes and spectra of γ-radiation in interplanetary space at various distances from the Sun;

—energy spectra, time profiles, and dynamics of GRBs progress for better understanding of particle acceleration and interaction at the time of GRBs, which will lead, in turn, to improvement of the phenomena models;

—time fluctuations of γ-radiation background fluxes along the Interhelioprobe SC orbit, with subsequent assessment of radiation environment in various parts of interplanetary space;

**3.** *Registration of charged particles fluxes along the SC orbit. Data to be obtained are:*

—measurements of cosmic rays charged component near the Sun, which is significant for analysis of solar wind motion in circumsolar space as well as for space weather prediction.

**7.9.2. Description of the SIGNAL instrument.** General view of the SIGNAL device and layout of its main units are shown in Fig. 29. It consists of a xenon gamma-detector (XeGD) (1), which is, basically, an impulse cylinder ionization chamber, filled with compressed xenon gas (Ulin et al., 2004; Vlasik et al., 2004; Elokhin et al., 2007), and anticoincidence scintillation detectors (ACD) (2), surrounding XeGD to provide anticoincidence shielding against charged cosmic radiation component.

At the bottom of the device, there are the power supply stabilization and voltage transformation unit (3) and digital electronics unit (4), digital electronics unit implementing processing and accumulation of experimental data coming from the detectors, control and running of the SIGNAL device as well as communication with telemetry of the SC.

All the units of SIGNAL device are located on the same base (7), and covered with protective case (5). The device is to be secured to one of the lateral faces of the SC by means of six fixing elements.

The entire device is protected by common thermal shield of the SC to avoid its exposure to direct solar radiation. Structural components of the SC and other scientific equipment are practically out of XeGD's field-of-view.

**7.9.3. Main characteristics of the SIGNAL equipment.** Main characteristics of the SIGNAL instrument are summarized in Table 16. Typical energy spectra of gamma-ray sources $^{137}$Cs and $^{133}$Ba measured by means of a XeGD prototype are shown in Fig. 30.

The SIGNAL device is intended to operate continuously in two modes. Idle mode provides gamma-ray spectra measurement every other second during one minute. The spectra will be analyzed for the purpose of flares and GRBs detection. If a flare or GRB is not detected, all the data are summarized in a single spectrum, that, along with auxiliary information, is stored in intermediate memory to be further prepared for telemetry transmission to the Earth.

Another mode (the mode of flares and/or GRBs registration) provides gamma-ray spectra measurement every second. Transition from idle mode to registration mode will be implemented automatically on the basis of detectors' load analysis.

In the normal mode, scientific equipment SIGNAL requires about 20 Mbites/day to store information on condition that transition of information takes place once a day.

### *7.10. Analyzer of Solar Wind Electrons HELIES*

**7.10.1. Scientific tasks of the HELIES experiment.** The HELIES experiment within the Interhelioprobe mission aims to measure the distribution functions of electrons of the solar wind as well as of interplanetary and circumplanetary plasmas. The experiment will help in solving the following scientific tasks:

—identification of mechanisms of solar corona heating and solar wind formation;

—clarification of dynamical processes in the solar wind and plasma fluctuations leading to transformation of charged particle energy to the wave (Alfven and magnetosonic) energy;

—determination of structure of current sheets in the solar wind at middle and small heliocentric distances;

—understanding the origin and properties of coronal mass ejections;

—investigation of properties of discrete plasma structures in the solar wind, especially out of the ecliptic plane, their influence to propagation and acceleration of charged particles (in particular, solar cosmic rays) in the inner heliosphere.

The HELIES measurements will also allow to obtain general information about the solar wind, which can be useful for the monitoring of "space weather". This monitoring could be long-term and

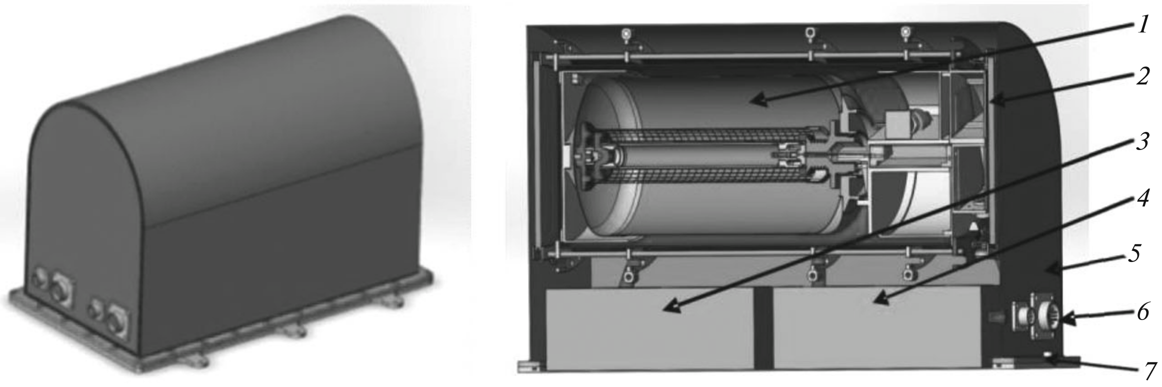

**Fig. 29.** General view of the SIGNAL device (left) and layout of its main units (right): (*1*) Xenon gamma-ray detector (XeGD); (*2*) anticoincidence scintillation detectors (ACD); (*3*) power supply stabilization and voltage transformation unit; (*4*) digital electronics unit; (*5*) case; (*6*) connectors; (*7*) platform.

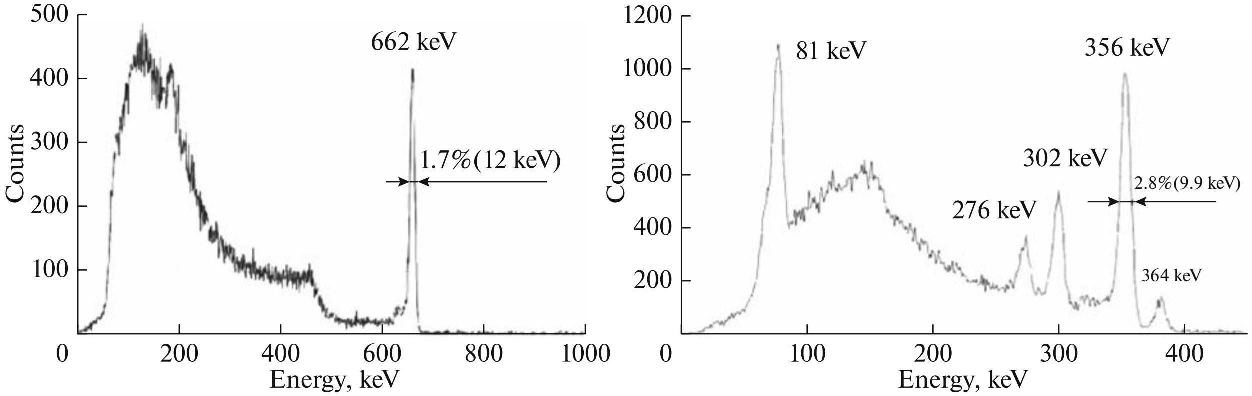

**Fig. 30.** Energy spectra of $^{137}$Cs (left) and $^{133}$Ba (right) gamma-ray sources measured by means of the SIGNAL XeGD prototype.

detailed. It is quite important due to the close approach of the Sun by the spacecraft (up to $60R_S$).

Capability to observe charged particles out of the ecliptic plane can give new information about the processes of plasma heating and acceleration close to the Sun, while observations of electron beams, as the "tracers" of the structure and topology of coronal and interplanetary magnetic field, will help to identify and investigate local plasma formations in the near-polar regions of the Sun.

**7.10.2. Description of the HELIES instrument.** The HELIES instrument is a monoblock consisting of two modules – detector and electronic ones. The instrument interface has connections with the onboard sys-

**Table 16.** Main characteristics of the SIGNAL device

| Characteristics | Values |
|---|---|
| Energy range of registered γ-quanta, MeV | 0.03–5.00 |
| Energy resolution over the gamma-ray line 662 keV, % | 1.7 ± 0.3 |
| Gamma-quanta detection efficiency at 662 keV, % | 2.0 ± 0.5 |
| Mass of the equipment, kg | 6.0 ± 0.5 |
| Outer dimensions, mm$^3$ | 420 × 280 × 265 |
| Voltage of power supply, V | + (24 –27) |
| Power consumption, W | 15 ± 5 |
| Operating temperature range, °C | 0–100 |

tems, with the compound and command unit, as well as with the Scientific Data Collection and Storage System (SSNI).

The HELIES instrument works as follows. Incoming electrons pass through systems of deflectors and then come to the electrostatic analyzer. To minimize effects of the SC surface charging and to maintain constant energy resolution of the instrument, negative potential ($-V_0$) is applied to the input deflector grids and to the external analyzer plate. This leads to deceleration of incoming electrons to an amount, which is almost equal to the SC potential. The deflecting system allows to collect electrons within an angle of ±60° with respect to the input axis of the analyzer. A quarter-spherical analyzer with the disk field of view of 360° is used as an electrostatic analyzer (Carlson and McFadden, 1998). Such analyzer is used in spectrometers working on the Wind, Cluster and STEREO spacecraft (Sauvaud et al., 1997; Rème et al., 2001; Sauvaud et al., 2008). The ring micro-channel plate (MCP) detector of the chevron type with the amplification factor of $2 \times 10^6$ is placed at the analyzer output. The grid with a potential of +300 V, allowing to additionally accelerate incoming electrons, is placed ahead of the detector. The MCP-detector efficiency is ≈70%. The scanning high voltage of 0–1500 V is applied to the deflector system, 0–750 V is applied to the electrostatic analyzer. 64 logarithmically distributed steps of high voltage are sequentially applied to the analyzer. The time required to collect entire spectrum is 2 s. The deflectors allow to obtain data within 6 angular sectors 120° each at every energy step of the analyzer. The maximum energy of the studied electrons is 5 keV, however, the distribution function of electrons within the full angle of 120° can be obtained only up to electron energy of 2 keV.

There is a collector system of 16 anodes on the MCP output. Thus, every anode collects charges within the 22.5° angular sector of the 360-degree field of view of the electrostatic analyzer. Further, signals from the anodes are going to the amplifiers-discriminators and then to the pulse counters. The instrument has the ability to check and calibrate the amplification tract using the test frequency generator, which applies pulses to the preamplifier input.

Prototypes of the HELIES detector module is used on the STEREO and MAVEN missions. The structural scheme and the general view of the HELIES prototype are shown in Fig. 31.

The HELIES electronic module consists of the power converter, 16 pulse counters linked with the preamplifiers, the data processing unit (DPU), and the interfaces with the onboard service systems.

The HELIES instrument can operate in several modes, differed by the information rate. The information rate can change from 0.3 to 3.0 Kb/s. Regimes can be changed with the command codes. The main characteristics of the HELIES instrument are summarized in Table 17.

### *7.11. Analyzer of Solar Wind Ions HELION*

**7.11.1. Scientific tasks of the HELION experiment.** Among the main scientific tasks of the Interhelioprobe mission is the solar wind studies in earlier unexplored regions close to the Sun out of Solar system ecliptic plane. HELION plasma instrument is a reliable gadget for measurements of detailed energy and angular spectra of solar wind/planetary ions and electrons (Verigin et al., 2012). These measurements can provide permanent solar wind monitoring in the inner heliosphere and may essentially contribute to solution of the following problems:

—solar wind radial evolution;

—solar activity transient phenomena, e.g., coronal mass ejections, large scale interplanetary shocks propagating throughout the inner heliosphere;

—studies of the heliospheric current sheet at small heliocentric distances;

—specification of the solar wind formation processes;

—studies of the solar wind – Venus interaction during flybys near this planet.

Joint remote observations of the Sun as well as coordinated in situ HELION, HELIOMAG, HELIES, etc. measurements will provide information for identification of solar corona heating and solar wind acceleration mechanisms.

So far there are no plasma measurements out of the ecliptic plane at heliocentric distances closer than 1.3 AU. It is assumed that the solar wind velocity at ≈0.3 AU is about the same as at the Earth's orbit while ion density and temperature are essentially higher than at 1 AU. Besides, ion density variations can be basically higher at small heliocentric distances. Thus, a plasma ion instrument for the Interhelioprobe mission must provide detailed measurements of complex 3D ion velocity distributions within the wide field of view (≈80°–100°) and wide energy range (≈40–12000 eV for ions and ≈0.35–6300 eV for electrons) in order to cover solar wind density and velocity, and also ion and electron temperature variations. Besides, an instrument must reliably operate under extreme thermal radiation of the Sun.

**7.11.2. Description of the HELION instrument.** The HELION experiment is based on the ROMAP experiment (Auster et al., 2009), which recently successfully operated onboard European ROSETTA mission in the end of 2014. Assembled HELION experiment sensor consists of two separate ion spectrometers (Ion-1, Ion-2), one electron spectrometer with joint spherical analyzing system, and one Faraday cup. Mock-up and principal diagram of the instrument are presented in Figs. 32 and 33, respectively. Ion-1 and Ion-2 spectrometers are formed by outer electrostatic analyser (Fig. 33). Incoming through entrances 1 and 2, ions can achieve counting channel electron multipliers (CEMs) 1 and 2, respectively, only in a narrow energy band. The central energy of this narrow band $E_i/q$ ($E_i$—ion energy, $q$—ion charge) is determined by variation of negative voltage applied to the central spherical electrode (Fig. 33). The energy resolution is $\Delta E_i/E_i \approx 7\%$. Additionally, only ions coming from knife shaped solid angle of ≈120° × 4° can be counted by CEMs 1 and 2. The energy range of both ion spectrometers is $40 < E_i/q < 12000$ eV/$q$.

Ion deflectors (Figs. 32 and 33) installed in front of both ion spectrometers provide possibility to deflect the center of knife shaped angular diagram up to ±50°. Figure 34 gives information on the general angular field of view of two ion spectrometers. The use of two orthogonal deflection systems for the Ion-1 and Ion-2 spectrometers provide possibility to determine a direction of arrival of ion population to the instrument.

Electron spectrometer of the HELION instrument is formed by the inner part of the hemispherical electrostatic system shown in Fig. 33. Entrance of the electron electrostatic analyser is placed between Ion-1 and Ion-2 entrances. Due to wider gap of this analyser, an energy range and energy resolution of electron spectrometer are $0.35 < E_e < 6300$ eV and $\Delta E_e/E_e = 16\%$ respectively, i.e. both lower than those for ion spectrometers.

In addition to ion and electron spectrometers Faraday cup (Fig. 32) measures ion integral spectra for the retarding potential ($U_{\text{ret}}$) in the range $0 < U_{\text{ret}} < 2000$ V in 32 voltage steps and within the field of view of 140° × 140°.

Complete time of all spectra measurements is as small as 10 s.

The HELION instrument sensor is mounted on a short boom under the Interhelioprobe SC thermal screen. Boom length and slope of instrument are selected to minimize the screening of the field of view of the instrument sensors, thus, all spectrometer entrances should not be under the screen while CEMs compartment should be in the screen shadow.

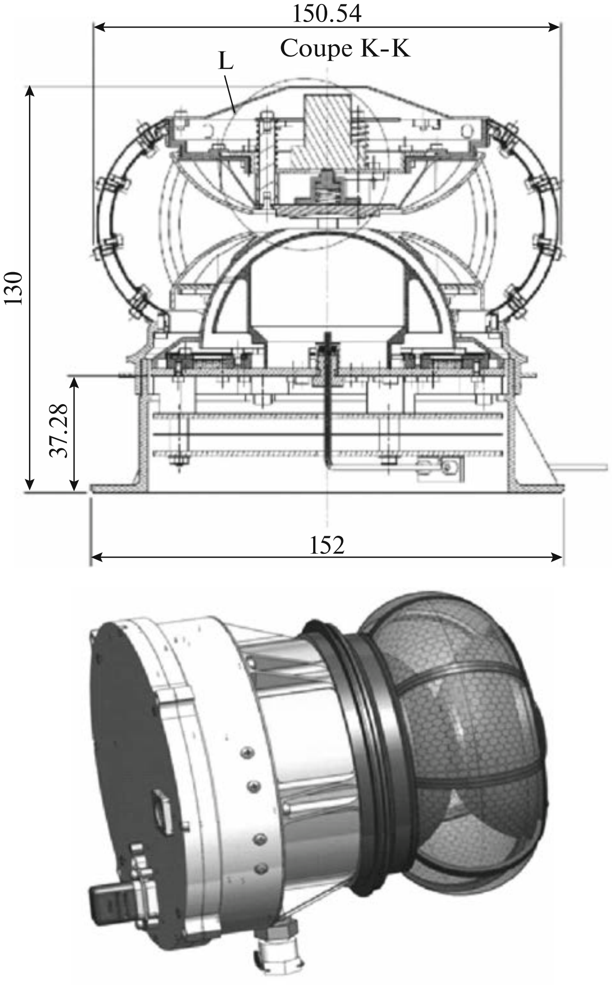

**Fig. 31.** Structural scheme (top) and general view (bottom) of the HELIES prototype.

All sensors of HELION experiment are controlled by a separate data processing unit (DPU) electronic block. Main elements of this block are presented in Fig. 35. DPU is installed at payload platform of the SC thermo-stabilized within –50°C to +50°C range.

**Table 17.** The main characteristics of the HELIES instrument

| Characteristics | Values |
|---|---|
| Energy range, eV | 1–5000 |
| Maximal number of energy levels | 64 |
| Maximal number of deflector's angular sectors | 6 |
| Maximal number of anodes (22.5°) | 16 |
| Full field-of-view | 360° × 120° |
| Information rate, Kb/s | 0.3–3.0 |
| Total mass, kg | 2.5 |
| Power consumption , W | 3 |
| Geometrical factor, cm$^2$ sr eV/eV | $8.4 \times 10^{-3}$ |

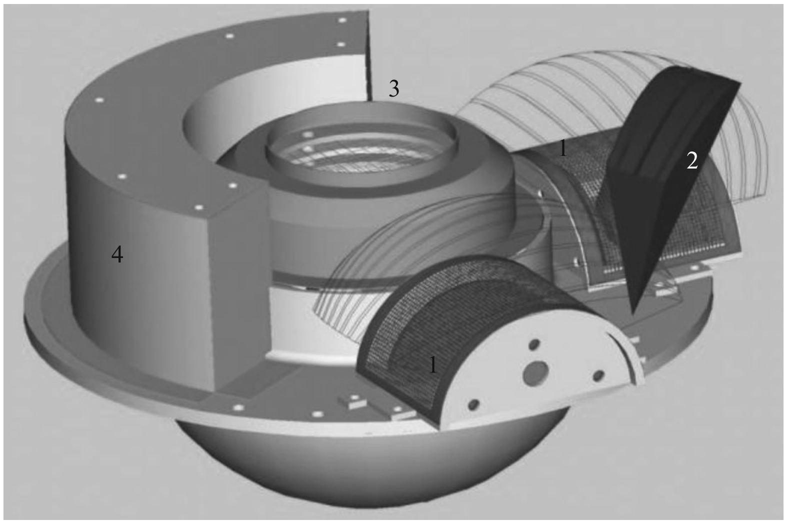

**Fig. 32.** Mock-up of the HELION sensor. Ion-1 and Ion-2 spectrometer entrances are under dark grey grids (1) that cover proper deflector systems. An entrance to electron spectrometer is marked by black color (2) while Faraday cup is marked by light grey (3). CEMs for particle registration are in the light grey (4) compartment.

Table 18 summarizes main characteristics of the HELION ion and electron sensors. Total weight of sensor and DPU block is ≈1.5 kg (1.8 kg with cabling). Minimal power consumption is ≈400 mW, maximal – ≈800 mW.

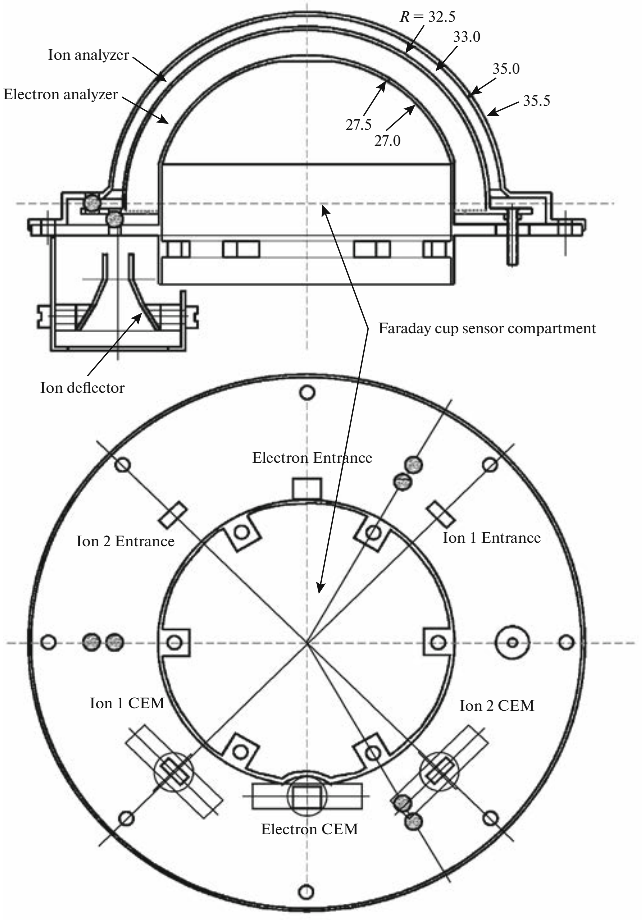

**Fig. 33.** Principal diagram of the HELION sensor.

### *7.12. Energy-mass-analyzer of Solar Wind Plasma PIPLS-B*

PIPLS-B experiment is intended to investigate properties of the solar wind and its sources in the solar corona by measurements of heavy ions' ionization state and velocity distribution characteristics.

Scientific goals of the PIPLS-B experiment will be achieved by measurements of characteristics of solar wind ions: their mass and charge compositions, velocities, temperature, concentration, and velocity distributions (Owocki et al., 1983).

PIPLS-B combines two types of analysis – electrostatic and magnetic – for measurements of solar wind ions physical characteristics. Electrostatic analyzer allows to select ions by $E/q$ ratio; magnetic system is necessary to perform $m/q$ analysis of ions. Structure of the PIPLS-B electronic optics are shown schematically in Fig. 36. Estimated characteristics of the PIPSL-B instrument are given in Table 19.

The prototype of PIPSL-B is the instrument RIP-803, flown on Prognoz-2 spacecraft (Zertsalov et al., 1976). Prototype of position-sensitive microchannel panel (MCP) detector has been already developed (Fig. 37) to perform estimations of mass resolution of the instrument.

### *7.13. Dust Particle Analyzer PIPLS-A*

Main goals of the PIPLS-A instrument is to record interplanetary and interstellar dust particles and to measure their elemental compositions, velocities, and masses.

Measurement of dust particle elemental composition is based on time-of-flight (TOF) measurements of ions, generated during the impact of dust particle at the target. Particle velocity measurement is performed by measurement of time delay between its pass through the entrance grid and impact at the target. Measurement of dust particle mass is based on measurement of charge pulse from the target during its impact. Structure of the TOF module of PIPLS-A is shown in Fig. 38. Figure 39 shows the 3D model of the detector. Estimated characteristics of the PIPSL-A instrument are given in Table 20.

The prototypes of PIPLS-A instrument are: LAMA (DuneXpress proposal; (Srama et al., 2006)), Cosmic Dust Analyzer for the Cassini spacecraft (Grun et al., 2001), PUMA and SP-1 for the Vega spacecraft (Vaisberg et al., 1987; Smirnov et al., 1987).

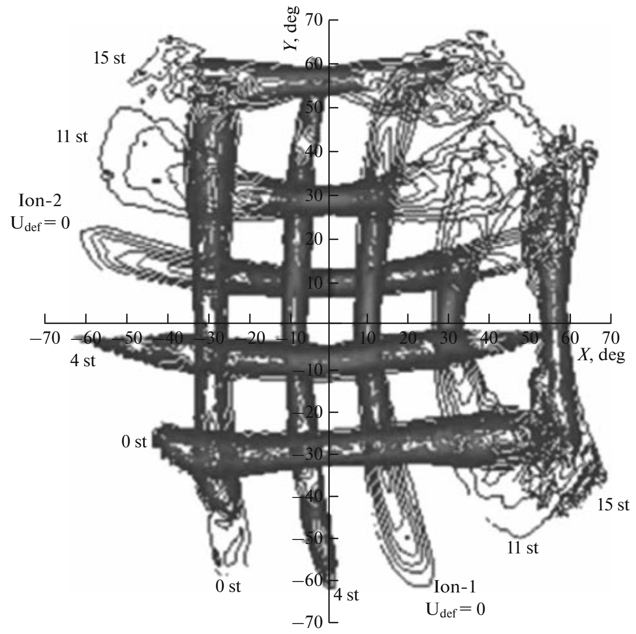

**Fig. 34.** General field-of-view of Ion-1 and Ion-2 spectrometers resulted from prototype of the HELION instrument calibration in ion beams under different steps (st) of voltage $U_{def}$ applied to ion deflectors.

### *7.14. Magnetometer HELIOMAG*

**7.14.1. Scientific objectives of the HELIOMAG experiment.** Magnetic field measurements jointly with plasma, energetic particles and wave measurements in near-Sun environment are carry out to study:

—heliospheric magnetic field and its disturbances;

—nature and global dynamics of the most powerful manifestations of the solar activity – solar flares and coronal mass ejections – and their influence on the heliosphere and space weather;

—mechanisms of solar corona heating and acceleration of the solar wind.

**7.14.2. Brief description of the HELIOMAG experiment.** The main problem of magnetic field experiment in the Interhelioprobe mission is to design and manufacture the magnetometer which will operate with set of metrological parameters in complicated temperature and radiation environment at close heliocentric distances from the Sun. Taking into account these circumstances under preparation of the magnetic field experiment HELIOMAG, it is extremely advantageous to use the preparation experience of the magnetic field experiment MPO/MERMAG in ESA BepiColombo mission. Therefore the magnetometer MPO/MERMAG are used as prototype of the HELIOMAG magnetometer. As a matter of fact HELIOMAG is renamed MPO/MERMAG. The HELIOMAG is the three-axial fluxgate magnetometer. The basic operating principle of the fluxgate magnetometer is well known and documented. The short description of

**Table 18.** Main characteristics of the HELION instrument

| Characteristics | Ions | Electrons | Faraday Cup |
|---|---|---|---|
| Effective area, $cm^2$ | 0.06 | 0.17 | 6 |
| Energy range, eV/$q$ | 40–12000 | 0.35–6300 | > 0–> 2000 |
| Energy/voltage gain | 8.0 | 4.2 | 1.0 |
| Energy resolution ΔE/E, % | 7 | 16 | |
| Number of energy steps | 64/32, log scale | 64/32, log scale | 32 |
| Angular field-of-view (FOV) | 120° × 100° | 15° × 60° | 140° × 140° |
| One energy step FOV | 120° × 6° | | |
| FOV angular number of steps | 32/16, lin. scale | | |
| Geometric factor, $cm^2$ ster keV | $3.5 \times 10^{-4} E$ | $4.3 \times 10^{-3} E$ | |
| Time resolution (total), sec/cycle | from 10 to 100 | | |
| Telemetry rate (total), byte/cycle | from 200 to 2000 | | |

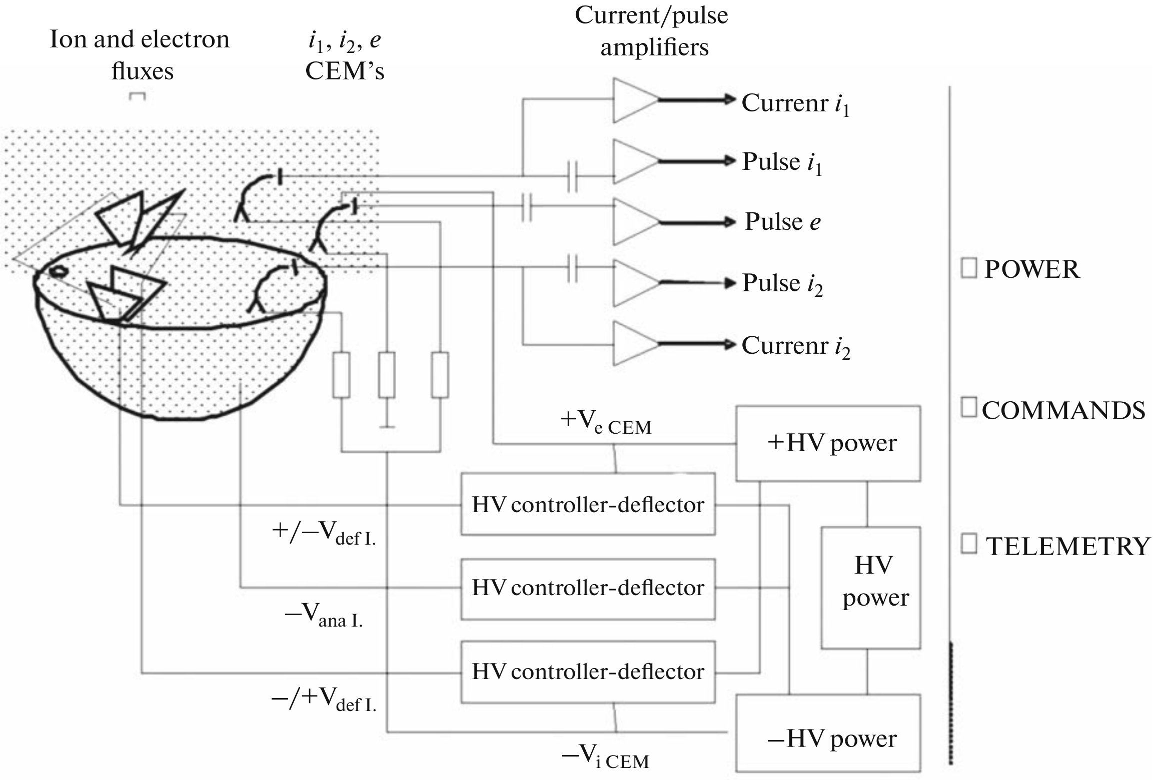

**Fig. 35.** General block diagram of HELION DPU main elements electronic box.

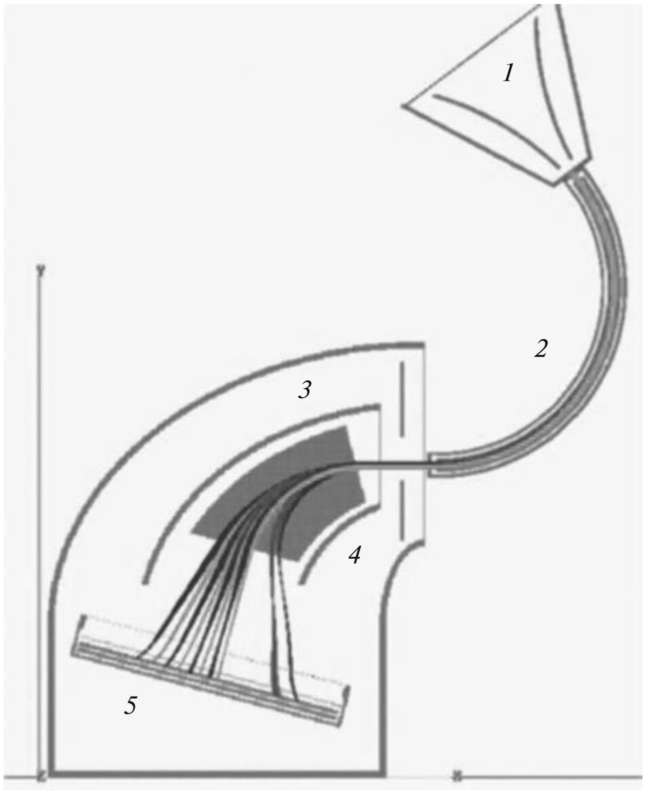

**Fig. 36.** Schematic structure of the PIPLS-B electronic optics. (*1*) Electrostatic scanner; (*2*) electrostatic analyzer; (*3*) drift tube; (*4*) magnet system; (*5*) coordinate sensitive MCP detector.

HELIOMAG (MPO/MERMAG) are given below, for details see, e.g. (Glassmeier et al., 2010). Main characteristics of the HELIOMAG experiment are summarized in Table 21.

**7.14.3. Structure of the HELIOMAG instrument.** The HELIOMAG instrument consists of two identical Outboard, Inboard sensors (Fig. 40) and Electronics box (Fig. 41).

The instrument has two identical magnetometers each with its own dedicated electronics. This two sensors the so-called "dual-magnetometer" technique will be applied in order to help determine the influence of the spacecraft magnetic field on observations. For detecting magnetic field disturbances from the spacecraft both sensors must be operable. Sensor is sensitive part of magnetometer transformed external magnetic field in electrical signal the amplitude of which is proportional to measured field.

HELIOMAG uses the digital technique for sensor output signal processing. Subsequently, the filtering, synchronous detection, and integration are perform by software, resulting in calculated value for the feedback current which is used to null the ambient field. The feedback current is controlled by a 16 bit digital-to-analog (DA) converter. The field proportional value (21 bit, resolution 2pT), which is transmitted to the instrument controller, consist of the sum of the weighted AD-and DA-converter values.

In addition to the sensors front end electronics, the instrument includes an Instrument Controller Unit (ICU), and a power supply for provision of secondary voltages to the sensor electronics and the ICU.

Functionally the HELIOMAG instrument is largely autonomous in operation, requiring a minimum of commanding only for selecting from a set of science operations modes and corresponding telemetry bit-rates.

The instrument has a number science modes which correspond to different telemetry rates. Each of the two sensors can be commanded to produce one of the following vector rates: 32, 16, 8, 4, 2, 1, 0.5 Hz. In nominal mode magnetometer will measure 16 vectors per second, with ~880 bit/sec bit-rate. The instrument is switched between science modes and calibration modes by use of a telecommand which contains the vector rate, range and calibration mode as parameter. The range can be modified by telecommand between ±2048 and ±64 nT with a corresponding digital resolution between 62.5 pT and 1.96 pT. HELIOMAG uses a packet structure with a fixed length (one packet contains 128 vectors with 3 components in 16 bit resolution), the packet rate will change with the selected vector rate.

The instrument design does not implement redundancy. Only the Spacewire telemetry interface and the power interface to the SC is redundant. These interfaces are to be used for science and houskeeping data transmission and telecommand reception.

**7.14.4. Magnetometer location on the SC and its thermal protection.** The instrument hardware comprises an electronics box, two sensor units with their associated thermal hardware and mechanical fixing, plus a harness which connects the sensors to electronics box. The sensors are mounted on a deployable boom, whilst the electronics box is located inside the spacecraft structure under multi-layer insulation (MLI). The Outboard sensor is mounted at the tip of the boom, the Inboard sensor is mounted ≈800 mm from the end of the boom.

The sensor is thermally isolated from the boom base plate by an insulating stand-off, which also serves to mount the sensor to the base plate. The sensor is further more protected by a thermal shielding. The shield is realized by mounting six optical solar reflectors (OSR) on each side of the sensor. The OSRs are glued with ELASTOSIL on the support structure made of high temperature carbon fiber reinforced plastic (HT-CFRP). Between the OSRs and the CFRP structure an aluminium foil is placed to cover the gaps between the mirrors and to support the heat transfer between the illuminated and the non-illuminated sides. High temperature multilayer insulation material, a 15-layers HT-MLI, is placed between the inner side of the thermal shielding and sensor. Figure 42 shows one sensor with stand-off, thermal shielding and indicated sensor harness. The thermal design was experimentally checked at the 10 solar unit in vacuum chamber. The result is positive.

**Table 19.** Main characteristics of the PIPLS-B instrument

| Technical characteristics | Values |
|---|---|
| Mass, kg | 2.5 |
| Dimensions, mm$^3$ | 156 × 357 × 140 |
| Power consumption, W | 10 |
| **Physical characteristics** | |
| Field-of-view, degrees | 30 × 80 |
| Energy range, keV | 1–20 |
| Mass range, m/q | 2–9 |
| Mass resolution, % | 10–40 |

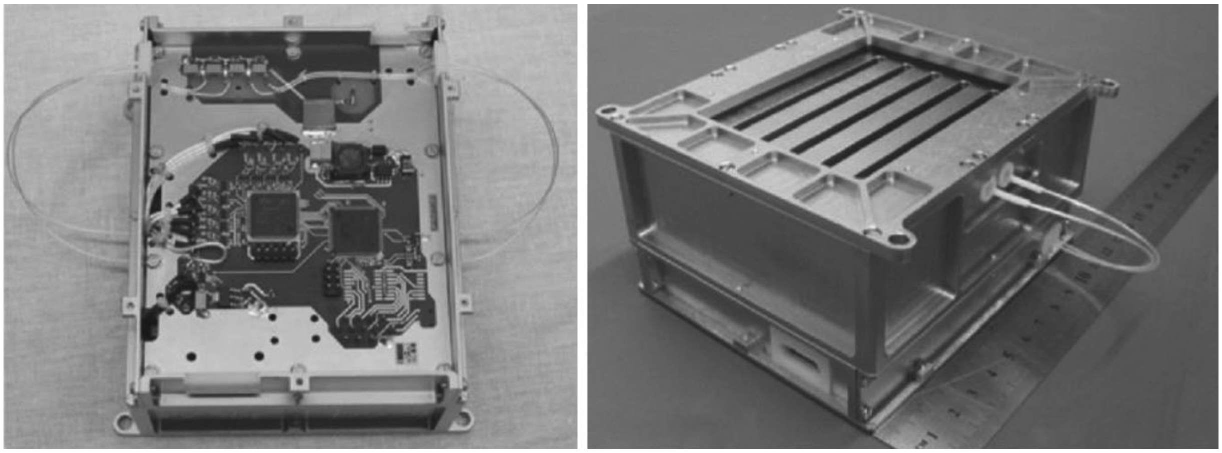

**Fig. 37.** Laboratory prototype of PIPLS-B position-sensitive MCP-detector with module of electronics.

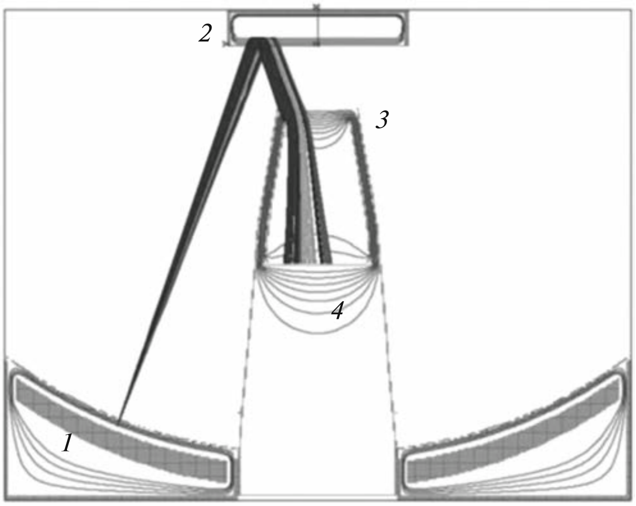

**Fig. 38.** Structure of the PIPLS-A TOF module with trajectories of ions. (*1*) Target; (*2*) reflector; (*3*) electrostatic lens; (*4*) MCP detector.

### *7.15. Integrated Magnetic Wave Experiment IMWE*

**7.15.1. Scientific objectives of IMWE.** Collisionless plasma of solar wind leads to important role of wave-particle interactions in physical processes in the interplanetary medium. Study of plasma and electromagnetic field fluctuations in wide range of frequencies is a key for understanding evolution of the solar wind when it extends out the solar corona.

General dynamics of interplanetary media is a crucial issue of the solar wind physics with a very important application to space weather. Solar wind structure depends mostly on its origin in the corona. However, the evolution of small scale phenomena occurring in the interplanetary plasma (Arghavani et al., 1985; Sperverlage et al., 2000) and their possible origin due to physical processes ongoing in the interplanetary medium is not fully studied.

Turbulence is inherent to the solar wind plasma and embedded interplanetary magnetic field (Horbury et al., 2005; Petrosyan et al., 2010). Energy exchange between different scales in plasma determines physical processes which influence the solar wind when it spreads in the heliosphere (Alexandrova et al., 2009). Measurements of the spatial and temporal scales comparable and smaller than the typical ion scales is of a prime importance for further progress in the solar wind studies.

Detection of solar radio bursts resulted from solar flares and shocks around the leading edges of CMEs is a powerful tool to investigate acceleration of plasma particles in the near-Sun environment, properties of media in the vicinity of the Sun and peculiarities of CME and plasma eruption propagation (Reiner et al., 1998; Reiner, 2001; Cairns, 2009).

The Integrate Magnetic Wave Experiment (IMWE) onboard the Interhelioprobe spacecraft is aimed on in situ investigations of solar wind fine structures, plasma turbulence at different scales and their dependence on a heliocentric distance and latitude. Dynamics of the solar wind when it propagates through the interplanetary space is important for the space weather issues related to the Earth and terrestrial-like planets, Mars and Venus.

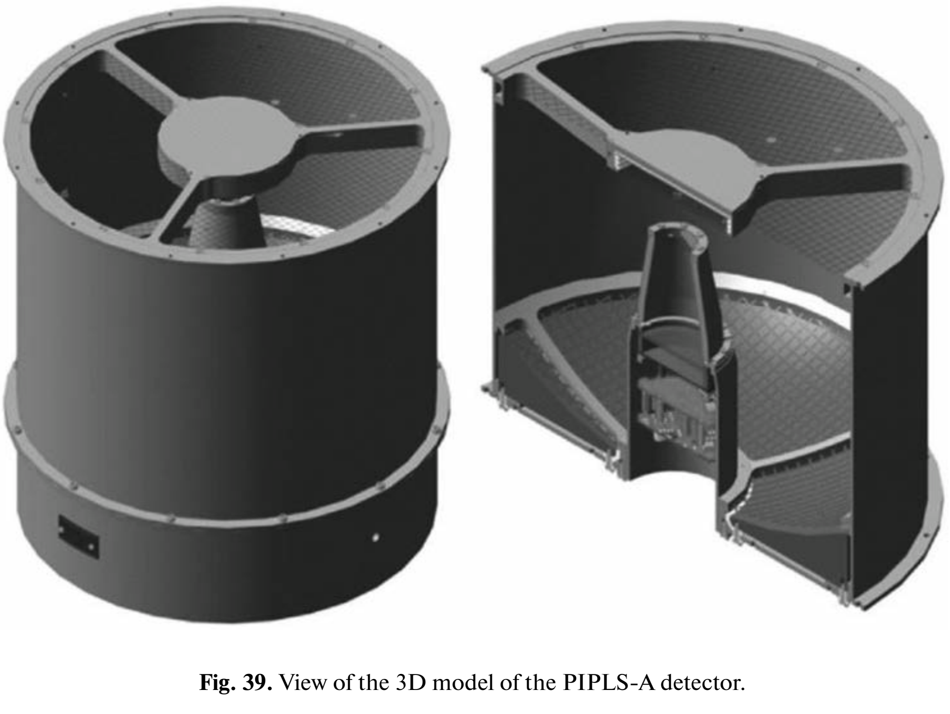

**Fig. 39.** View of the 3D model of the PIPLS-A detector.

**Table 20.** Main characteristics of the PIPLS-A instrument

| Technical characteristics | Values |
|---|---|
| Mass, kg | 2.5 |
| Dimensions, $mm^3$ | 310 × 310 × 310 |
| Power consumption , W | 9–10 |
| **Physical characteristics** | |
| Measured parameters of dust particles | Mass, velocity, elemental composition |
| Mass range, g | $10^{-16}$–$10^{-6}$ |
| Velocity range, km/sec | 3–100 |
| Time-of-flight (TOF) mass resolution | $M/\Delta M > 30$ |
| Sensitive area, $cm^2$ | 110 |
| Field-of-view | Cone, 45° |

**Table 21.** Main characteristics of the HELIOMAG experiment

| Characteristics | Values |
|---|---|
| Dynamic Range, nT | ±2048 |
| Resolution, pT | 2 |
| Noise, pT /√ Hz | 10 |
| Sensitivity, nT | 0.1 |
| Stability | <1 nT/year; <3 nT/100°C |
| Power consumption, W | 5 |
| Sample rate, vectors/sec | 128 |
| Mass sensor OB with thermal shield, g | 300 |
| Mass sensor IB with thermal shield, g | 300 |
| Mass Electronics, g | 1250 |
| Total mass (without cables), g | 1850 |
| Dimensions of sensors, mm | Ø 53, L 91 |
| Dimensions of E-box, $mm^3$ | 162 × 122 × 96.6 |
| Dimensions of thermal shield, $mm^3$ | 82.4 × 82.4 × 122.7 |

In particular, scientific objectives of the experiment are:

—inherent structures of the solar wind flow at different heliospheric distances and latitudes, their time and spatial behavior;

—discontinuities in the solar wind as boundaries related to sharp changes in interplanetary magnetic field and plasma parameters;

—morphology of short scale disturbances observed in SW; their nature, structure, propagation and evolution;

—turbulence and intermittency as a "finger prints" of solar wind origin in corona and physical processes ongoing as the solar wind propagates in interplanetary space;

—large scale phenomena (e.g., CMEs), their evolutions and particle acceleration processes associated with them.

To cover its specific scientific objectives, the IMWE experiment is designed to carry out the following measurements:

- magnetic field fluctuations in wide frequency band up to 30 MHz;
- ion flux variations at frequencies from 0 to 32 Hz;
- kinetic parameters of ion flux in the solar wind (density, 3D-velocity and temperature) with a time resolution of 0.031 s.

**7.15.2. Magnetic sensors and electronics.** All magnetic sensors of the IMWE experiment are presented in Fig. 43.

Low frequency magnetic sensor (Russian acronym – DNMP). The DNMP sensor is the flux-gate magnetometer commonly used for measuring quasi-static magnetic fields. The flux-gate magnetometer incorporated in the IMWE experiment is dedicated to mea-

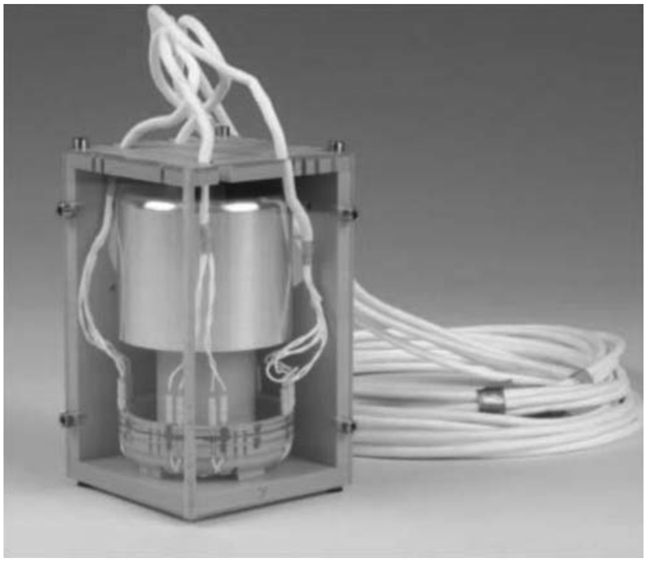

Fig. 40. The HELIOMAG sensor with harness.

sure the magnetic field vector at a rate of 64 Hz; sensitivity is 0.01 nT (Korepanov and Marusenkov, 2012).

High frequency magnetic sensor (Russian acronym – DVMP).The DVMP sensor is the three components search coil magnetometer. It measures the magnetic field fluctuation at frequencies from about 10 Hz to 20 KHz; sensitivity is $10^{-6}$ nT/Hz$^{1/2}$. Details on its design and operation can be found in (Korepanov and Pronenko, 2010).

The DNMP and DVMP are designed and developed by Lviv Center of Institute for Space Research Institute (Ukraine).

Magnetic loop antenna (Russian acronym – VChK). The High Frequency Magnetic Loop (HFML) is a magnetic sensor dedicated to measure magnetic field at frequencies from 30 kHz to few tens of MHz where it offers a better sensitivity in comparison to the search-coil. The sensor is provided by the Laboratoire de Physique et Chimie de l"Environnement et de l'Espace (LPC2E/CNRS, Orleans, France).

Low frequency analyser (Russian acronym – NchA). The NchA performs processing of data gathered by the three-axial flux gate and search coil magnetometers. It measures intensity, polarization, and coherence properties of waves in plasmas. Modern onboard data analysis methods and compression algorithms are used to reduce the volume of the transmitted data while conserving the importance of scientific information. Two three-component signals from the flux-gate and search coil magnetometers are low-pass filtered and simultaneously A/D converted at sampling frequencies of ~500 Hz and 500 kHz, respectively. The digital data are further decimated and low-pass filtered by computing algorithms implemented in an FPGA, leading to the respective maximum sampling frequencies of 50 Hz and 50 KHz. These data are sent to the IMWE control unit and, then, to spacecraft telemetry. The NChA is designed and developed by the Institute of Atmospheric Physics of the Academy of Sciences of the Czech Republic (Prague).

Control unit of IMWE (Russian acronym – BE IMWE). The BE IMWE is developed by the Space Research Institute (IKI) of the Russian Academy of Science (Moscow, Russia) contains a processor unit for sampling, pre-processing and storage of measured data before they are sent to onboard telemetry system (Fig. 44). The interface subsystem of unit allows to perform all communications with the spacecraft system. The power subsystem generates all internal voltages needed to operate sensors and subsystems of instrument.

The control unit is operated in one of the available telemetry modes – survey mode and burst mode. In the burst mode data stream intended for studying non-

Fig. 41. The HELIOMAG electronics box.

linear phenomena, conserves the continuous fluxgate magnetometer data, discrete snapshots of three axial waveform (search coil magnetometer) and one component (magnetic loop antenna) measurements. The burst mode is triggered by onboard algorithm or by telecommand. In the survey-mode data, lower-resolution continuous flux-gate magnetometer data are transmitted together with onboard analyzed and averaged spectral data from the higher-frequency wave measurements (magnetic loop antenna) and with onboard calculated wave propagation and polarization parameters (search coil magnetometer data).

The weight of magnetic sensors, NchA and control unit of IMWE experiment is 6 kg, power consumption is about 14 W.

**7.15.3. Plasma spectrometer BMSW-I.** Plasma spectrometer BMSW-I (Fast Monitor of Solar Wind, Russian acronym – BMSW-I) is a part of the IMWE wave experiment onboard the Interhelioprobe spacecraft and performs monitoring of the solar wind properties with high temporal resolution. Particular scientific objectives of the BMSW-I instrument are:

—solar wind turbulence at the ion kinetic scale;

—solar wind acceleration;

—abundance of $He^{++}$ in solar wind plasma and its temporal variations.

The principle of BMSW-I instrument function is based on simultaneous measurements of the total ion flux and ion integral energy spectrum by four nearly identical and independent Faraday cups (FC). FCs have been widely used for plasma investigations from the beginning of space exploration era till now (e.g., (Gringauz et al. 1960; Vasylinuas 1971; Vaisberg et al. 1979; Zastenker et al. 1982; Šafránková et al. 1997, 2013). The main advantages of instrument with FCs sensors are simple design, allowing under various conditions to reliably determine velocity vector and temperature of the solar wind ions, and very accurately – density of the solar wind.

A design of the FC is shown in Fig. 45. The FC is equipped with four grids: grounded grids cover outer and inner diaphragms (C4, C2), a positive control grid (C3), a suppressor grid (C1) and a collector (K), divided in two parts. The grounded grids are used for an elimination of the internal electric field outside FC. The control grid is connected to a tunable High Voltage (HV) source and thus only the ions with the velocity sufficient to overcome the grid potential can reach the collector. The HV on the control grid are swept linearly between 0.1 and 4 or 5 kV up and down. The suppressor grid is powered by a negative potential of $\approx -300$ V. This potential returns back photoelectrons emitted from the collector by a solar UV radiation as well as solar wind electrons with energies up to 300 eV. The collector divided in two parts allows the simultaneous measurement of ion fluxes in the different branches of the angular characteristics of the FC. It makes possible to determine the value and direction of the ion flux with two FCs instead of three, as it was implemented in a previous version of similar instrument, and to make simultaneous operation of the adaptive and sweeping modes with two FCs rather than four as in the previous versions.

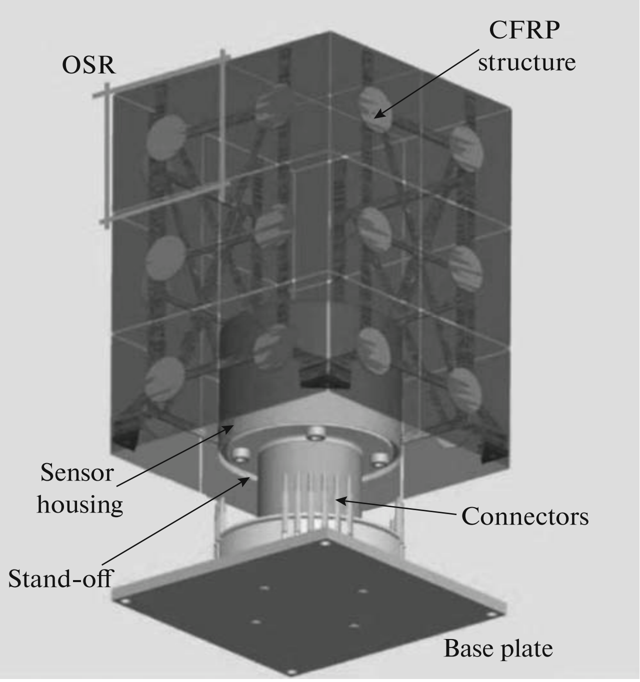

**Fig. 42.** Illustration of the HELIOMAG sensor with thermal shielding.

Figure 46 presents the mass model of BMSW-I instrument. BMSW-I has four FCs. The BMSW-I is mounted on a stand-off bracket on the side of the spacecraft. The bracket provides viewing near the edge of the heat shield umbra during solar encounters. This mounting, combined with the large aberration angles of the solar wind, allow to provide measurements of the ion distribution functions when the Interhelioprobe spacecraft will be close to the Sun. Since the BMSW-I will be cut off from the thermo stabilizing platform of the spacecraft, it has its own thermal protection shield and heat-conducting path with radiators. It allows to decrease the temperature at DPU in the worst thermal case to 95°. In the future, it is expected to introduce a more effective thermal isolation between the sensors and DPU.

The weight of BMSW-I is 3.5 kg, power consumption is not exceed 4.5 W.

The BMSW-I should be capable to measure distribution functions of protons and alpha particles over the energy/charge range of 50 eV/$q$ to 5 keV/$q$. The energy resolution ($\delta E/E$) should be ~5–7%. The sensitivity and dynamic range need to be adequate to measure ion distributions in 0.031 s at working orbits from $60R_S$ to $220R_S$.

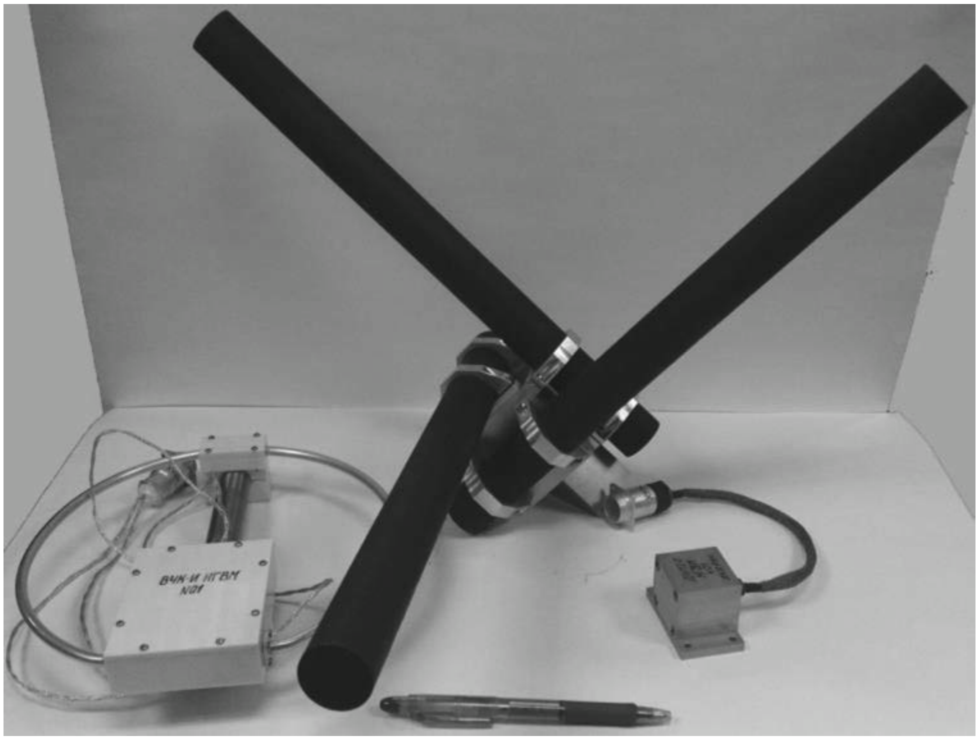

**Fig. 43.** Mass models of magnetic field sensors of the IMWE experiment (VChK, DVMP and DNMP, from left to right; see text for an explanation).

BMSW-I has two operation modes, which allow to determine the basic solar wind parameters -density, velocity, temperature and ion flux vector. In all modes two FCs serve for a determination of the solar wind direction and total ion flux with resolution ~0.031 s. The control grids of these FCs are grounded. Two others FCs are equipped with high voltage sources that supply the control grid of each FC, allowing working in sweeping or adaptive modes. Time resolution in the sweeping mode is 1–2 s for solar wind density, velocity and temperature. In the adaptive mode density, temperature, and solar wind velocity vector can be determined with a time resolution up to ~0.031 s.

**Fig. 44.** Mass model of the IMWE control unit.

BMSW-I is designed and developed in Charles University (Czech Republic) in collaboration with Space Research Institute (IKI) of Russian Academy of Sciences (Russia).

### *7.16. Radiospectrometer RSD*

**7.16.1. Scientific objectives of the RSD experiment.** Observations of solar radio bursts in the metric wavelength range provide important information on physical processes and disturbances in the solar corona, such as coronal mass ejections (CME), shock waves, and accelerated particle fluxes. These phenomena cause various effects in near-Earth space, which are known as "space weather" (change the radiation conditions, produce disturbances in the geomagnetic field, atmosphere, and ionosphere), which, in turn, can have a significant impact on technological systems and human health. Therefore, observations of solar radio bursts are of great prognostic importance, as they allow us to trace the propagation of geoeffective agents all the way from the Sun to the Earth.

Currently, a huge amount of data has been accumulated on the properties of sporadic solar radio emission in the meter wavelength range (e.g., radio bursts of type II, III, and IV), including those obtained with

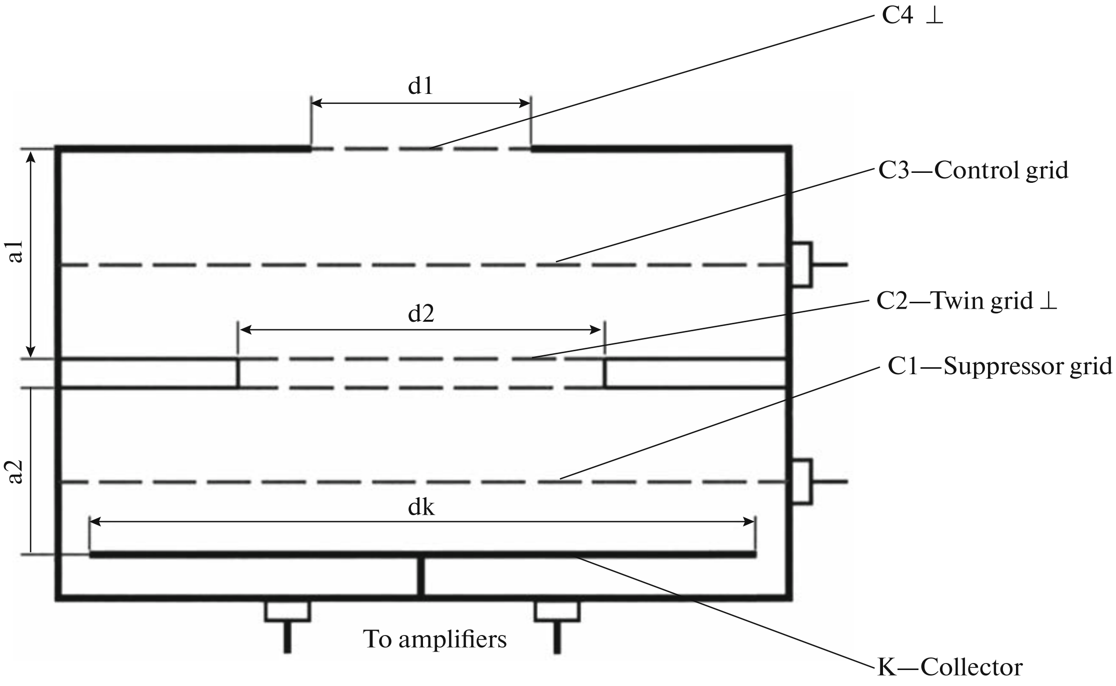

**Fig. 45.** A design of the Faraday cup: C4 and C2 are outer and inner diaphragms with grounded grids, respectively, C3 – a positive control grid, C1 – a suppressor grid, K – a collector.

space-borne facilities (Kahler et al., 1989; Bougeret et al., 1995; Reiner et al., 1998; Hoang et al., 1998; Leblanc et al., 1998; Kaiser, 2005; Reiner et al., 2006; Bougeret et al., 2008; Pick and Vilmer, 2008). However, many problems still remain unsolved, in particular, those concerning the mechanisms of particle acceleration in flares, generation of shock waves, and occurrence of coronal mass ejections. The Interhelioprobe mission gives us a unique opportunity to study the solar radio emission at different distances from the Sun, from out-of-ecliptic positions, and, sometimes, directly in the generation region. This will bring us closer to understanding the nature of active processes in the Sun.

## TYPE II RADIO BURSTS

Type II radio bursts are associated with propagation of shock waves in the solar corona and interplanetary medium. The questions that remain unclear are as follows:

1. The origin of shock waves and relation of type II radio bursts to flares and CMEs. Type II radio bursts can occur in the absence of CME or can be closely related to the latter, the radio source being located either inside the CME body or ahead of its leading edge. These data suggest the existence of different shock waves, some of which are generated during the flare explosive phase (heating and evaporation of plasma) and others (piston-shock) are excited in front of the CME leading edge. To clarify this point it is important to determine the location of the shock front relative to CME. At present, the CME position is determined in the plane of the sky, while the shock front moves toward the Earth almost perpendicular to this plane. Out-of-ecliptic observations of the location of sources of type II radio bursts can help us solve this problem.

2. Currently, the propagation velocity of shock waves is determined by the frequency drift rate of type II radio bursts using certain models of height distribution of electron density in the solar corona, which may not be applicable to each individual case. In the RSD experiment, the shock wave velocity can be measured directly without having recourse to electron density models.

3. Multiple type II radio bursts – several type II radio bursts observed in a single event. Position observations of radio sources are necessary to find out whether these bursts are associated with generation of different shock waves at a common place and their propagation along a common trajectory or the shock waves are generated at different sites in an active region.

4. It is interesting to clear up what sections of the shock front (quasi-transversal or quasi-parallel) are associated with the type II radio burst sources. For this purpose, we have to trace the location of radio sources with respect to the curved shock front (at the bow shock or flanks).

**Fig. 46.** Mass model of BMSW-I plasma spectrometer.

5. Position observations are necessary to understand the deceleration of sources of the type II coronal radio bursts. Does the frequency drift decrease as a result of the real deceleration of shock waves (e.g., when they become turbulent and begin damping rapidly as the critical Mach number is exceeded) or as a result of shock propagation along a curved trajectory or variations in electron density distribution along the trajectory?

6. We do not yet fully understand the origin of the fine structure of type II radio bursts. Is the splitting associated with one source or with different parts of the shock front or does the herring-bone pattern occur only when the shock front intersects open field lines? In the latter case, the source of type II radio bursts must drift slowly along the solar surface.

7. Important is the relationship between coronal and interplanetary shock waves. Are they independent or the interplanetary shock wave is a continuation of the coronal one? In this case, the estimates of parameters of the coronal shock waves can be extended to interplanetary shocks.

8. Is the difference in the spectral characteristics of both coronal and interplanetary type II radio bursts (broad-band, smooth or narrow-band, discontinuous spectrum) due to different types of shock waves or to the interaction of shock waves with different features, such as dense fibers, streamers, or corotating regions in the solar wind.

9. Another important issue is the mechanism of acceleration of electrons generating type II bursts. When the spacecraft enters the source region, we will have an opportunity to measure the parameters of accelerated electrons and to determine their acceleration point and relationship with the excited turbulence.

## TYPE IV RADIO BURSTS

Type IV radio bursts are closely related to CME, but many details of this relationship still remain unknown:

1. At present, the minimum frequency the type IV continuous radio emission has been traced to is 7.5 MHz, which, according to the plasma hypothesis and electron density distribution in interplanetary medium (Leblanc et al., 1998), corresponds to the source location at $\approx 3R_S$. In-situ data on the source location in space and relative to CME (inside the CME body or at its leading front) are unavailable.

2. We do not know the shape of the radio source (cloud or loop). Therefore, it is difficult to draw a conclusion about a possible distribution function of energetic particles (beam, cone, or isotropic distribution with a velocity dip). As a result, it is difficult to estimate the contribution of the plasma and synchrotron mechanisms to the observed radio emission.

3. The role of shock waves as particle accelerators in the occurrence of type IV radio bursts is unknown.

## TYPE III RADIO BURSTS

The theory of type III radio bursts is best developed compared to the other types of radio emission. Generally accepted is the plasma theory in which type III radio bursts are generated in the solar corona and interplanetary space by accelerated electron fluxes at the plasma frequency and its second harmonic. This allows us to use out-of-ecliptic observations of type III radio burst sources at different frequencies to define the trajectory of electron fluxes (which is equivalent to the shape of the interplanetary field lines) and, from the steepness of the field spiral, to determine the solar wind speed. At the same time, the location of radio sources provides us with a simple direct method of determining electron density in interplanetary space. An example of such reconstruction of magnetic field lines in interplanetary space is given in (Fitzenreiter et al., 1977).

A common question that arises when considering all types of radio bursts described above is the question of the fine structure of radio emission generated in interplanetary space. Despite their sophisticated and multi-purpose equipment, the WIND/WAVES and STEREO/S/WAVES space experiments have low temporal resolution and limited frequency range that do not allow us to trace in detail the fine structure of radio bursts when passing from the meter to the decameter and kilometer frequency range. For example, to study the zebra pattern in CME radio emission in interplanetary space it is necessary to obtain dynamic spectra with a resolution of ≈0.1–0.2 s.

Another common issue is the direction of the emission and the fine structure of radio bursts. The direction of the fiber bursts and zebra structure still remains unclear. STEREO-A and STEREO-B simultaneous observations of the dynamic spectra have shown how important it is to take into account the emission direction when analyzing the observation data.

**7.16.2. Brief description of the RSD instrument.** The lay-out of the RSD instrument is represented in Fig. 47. The instrument consists of an antenna feeder unit (AFU RSD) and RSD receiver (RCV RSD). The former comprises three RSD antennas (A1–A3) and radio-frequency cables (RFC1–RFC3) connecting the antennas to the input circuits of the RSD receiver. As seen from Fig. 47, the RSD instrument has three identical channels, which provide measurements of three components of the electromagnetic field vector.

The RSD antennas (A1, A2, A3) are identical and are placed on the SC body so as to enable the computation of three orthogonal components of the electromagnetic field intensity vector. A possible variant of the mutual position of the antennas is illustrated in Fig. 48. Each antenna comprises an antenna amplifier that provides the necessary sensitivity of the device and match of the antenna radiator output impedance with the impedance of the RF cables in a wide frequency range. The power is supplied to the antenna amplifier from the RSD receiver via the radio-frequency cable through the appropriate isolation circuits.

In our case, the orthogonal components of the vector of the electromagnetic-field intensity can be derived from the following relations:

$$a_1 = x\cos(30°) - z\sin(30°);$$

$$a_2 = -x\cos(45°) - y\cos(45°) - z\sin(30°);$$

$$a_3 = -x\cos(45°) + y\cos(45°) - z\sin(30°).$$

The block diagram of the RSD receiver is shown in Fig. 49. The receiver comprises three identical measuring channels (MC1–MC3). The digital signals processor (DSP) is considered to be part of the measuring channel, but it is placed in the control module and is used by all measuring channels in the time-sharing mode. The data acquisition module (DAM) comprises a control processor, a data pool memory, and a data transmission interface. The power supply unit forms the secondary galvanic isolated power supply for the RSD receiver components and antenna amplifiers.

The block diagram of the measuring channels is represented in Fig. 50. Each measuring channel contains a frequency splitter (FS1-FS3), which divides the frequency band of the input signal into two bands A and B. This enables independent control of the adjustable amplifiers gains (AA1A–AA1B, AA2A–AA2B, AA2A–AA2B) for better matching the dynamic range of the measuring channel with that of the input signals. The division of the input frequency band is performed at the upper boundary of the first spectral channel, i.e., at 30 MHz. Two buffer amplifiers in each measuring channel (BA1A–BA1B, BA2A–BA2B, BA2A–BA2B) ensure load matching for the outputs of the adjustable amplifiers with the inputs of the two-channel analog-digital converters (ADC1, ADC2). Each ADC has four channels for digital spectrum conversion (DSC), in which the input frequency band is divided into four parts. Each DSC channel can handle the digital data stream from any of the ADC inputs. The input signal is tentatively divided into the following frequency bands: 15 kHz – 30 MHz, 30 MHz – 75 MHz, 75 MHz – 150 MHz, and 150 MHz – 300 MHz. Each frequency band (data from each measuring channel) undergoes spectral processing in DSP (in the form of fast Fourier transformation). DSP ensures computation of the spectrum of the received signal in each measuring channel in each of the four digital frequency ranges. The number of frequencies in each spectrum is 2048.

The RSD receiver is a single unit (see Fig. 51) with the following characteristics:

1. dimension – 192 × 161 × 59 mm;
2. mass – 1.4 kg.

The antenna of each channel (see Fig. 52) consists of a skeleton boom 800 mm long, an amplifier, and a 500 mm long radiator ribbon. The radiator ribbon is a strained convex-concave ribbon of stainless steel. In the normal position, it is fixed at 30° to the boom axis. The mass of the antenna is 300 g.

The main characteristics of the RSD instrument are given in Table 22.

**7.16.3. Cooperation of the RSD experiment with other observations.** It should be noted that the Interhelioprobe mission will provide an opportunity to con-

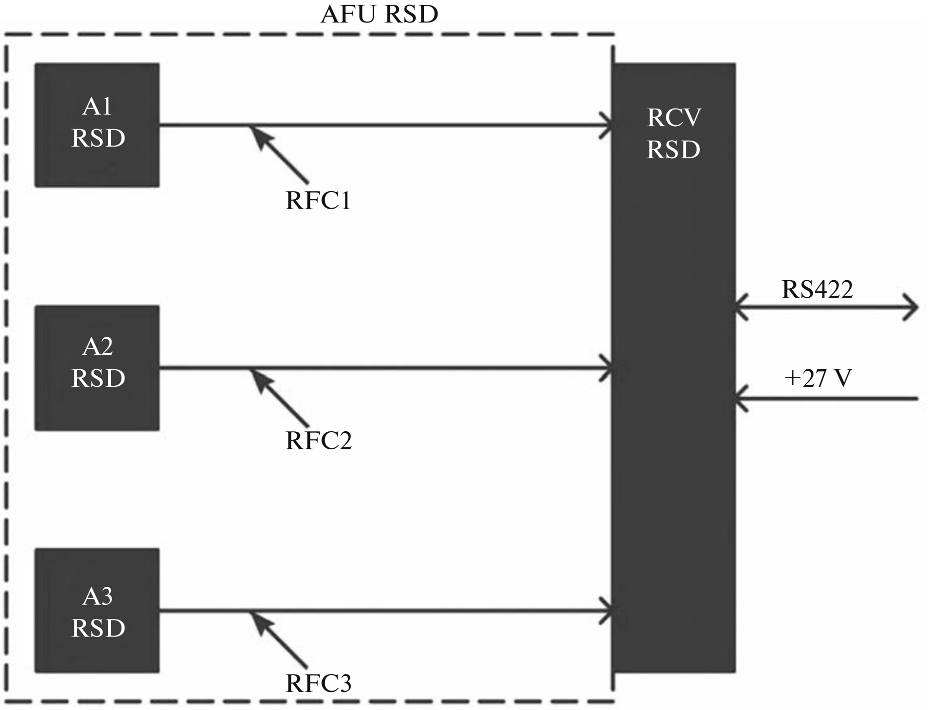

**Fig. 47.** Layout of the RSD instrument.

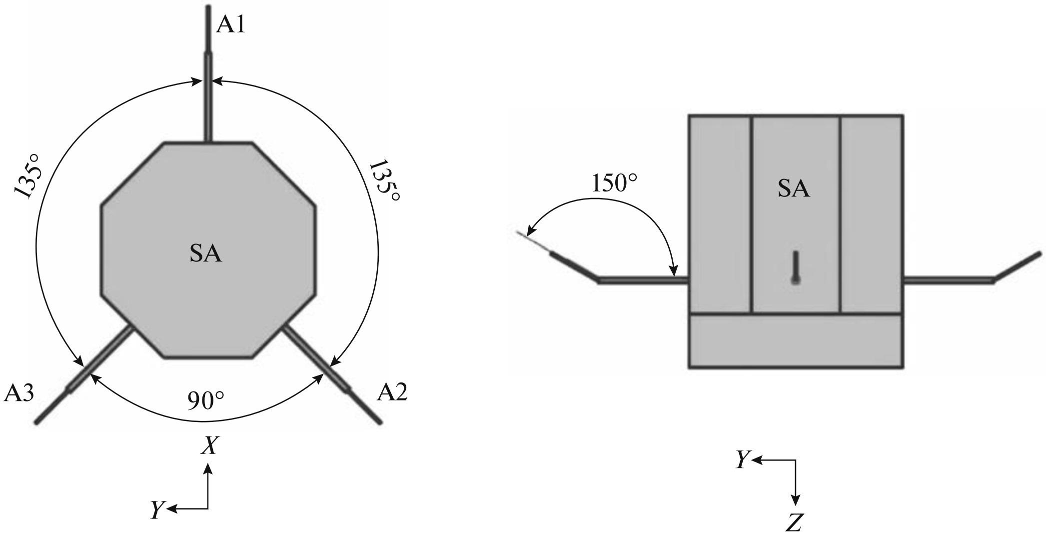

**Fig. 48.** A variant of mutual position of the RSD antennas.

duct simultaneous measurements with radio spectrometer, optical and X-ray devices, and in-situ measurements of plasma parameters at radio sources. The chosen ballistic trajectory will enable intersection of SC with CMEs, shock waves or high-energy particle fluxes in interplanetary space.

Observations of plasma density and magnetic field inside CMEs will, at last, allow us to measure plasma irregularities beyond the CME leading edge. Until now, only white-light coronagraph observations of CME structure have been available. In some events, shock waves were observed to catch up with a CME and pass through its body. In this case, one could see a unique fine structure in the form of a rope of fibers in the dynamic spectra (Chernov et al., 2007; Chernov, 2008). Observations inside CMEs will give us a better understanding of the plasma processes that occur therein, such as acceleration of fast particles in the

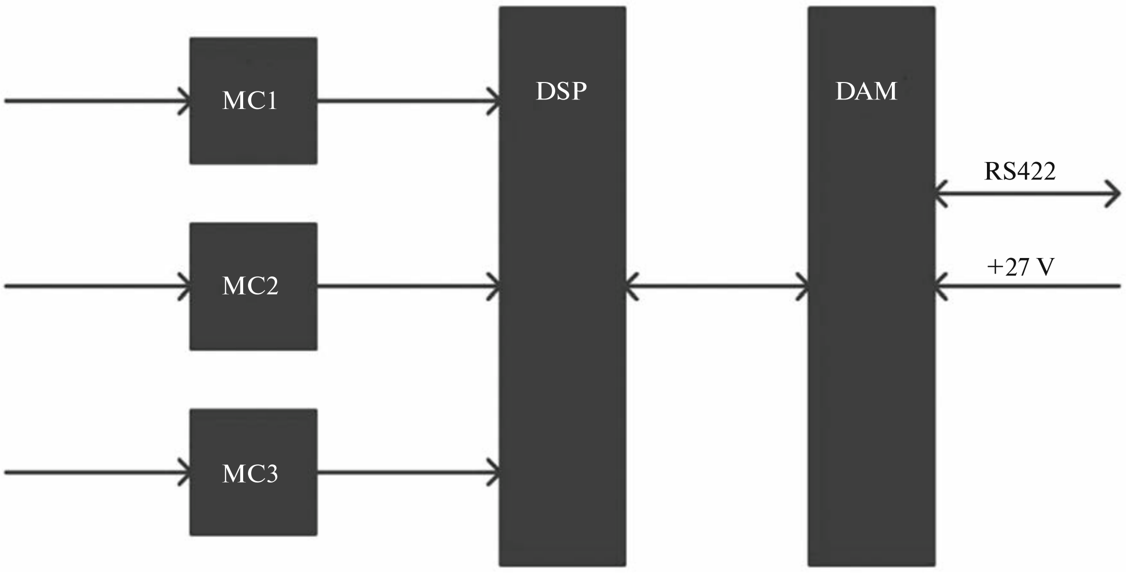

**Fig. 49.** RSD receiver block diagram.

shock front and their trapping between the CME leading edge and the shock front. Such an analysis will require simultaneous X-ray images of CME.

As for the type III radio bursts, it becomes possible to trace the entire chain of processes from accelerated particles to electrostatic and electromagnetic waves and to determine the particle spread mode (whether it is quasi-linear or a strong turbulence is present).

It is obvious that the frequency range of radio observations must be broad enough to address all problems listed above. The high-frequency limit of 300 MHz must ensure the study of coronal radio bursts and the low-frequency one – the study of radio bursts generated in the heliosphere. According to the planned trajectory of the Interhelioprobe mission, the SC will pass at a distance of $\approx 60R_S$ from the Sun, i.e., the lower limit of the frequency range must be ≈15 kHz.

The radio spectrometer allows us to investigate not only parameters of thermal plasma and solar radio emission, but also the magnetic field by recording various types of plasma resonances (gyro- and diffuse resonances of types Q and D). Moreover, in the case of recording the splitting of D resonances, the accuracy of determining the magnetic field strength may exceed the accuracy of the magnetometer. Thus, the device can also be used for measuring the magnetic field magnitude along the spacecraft trajectory.

### *7.17. Charged Particle Telescope SKI-5*

SKI-5 is a suite of scientific instruments of the Interhelioprobe mission to detect energetic charged particles of solar and interplanetary origin. SKI-5 is capable to study spectra of solar energetic charged particles (SEPs), as well as of the super-thermal part of solar wind. SKI-5 is an important contributor to the complex investigation of the solar activity. Specifically, without knowledge of spatial and temporal properties of the local characteristics of the solar wind and of energetic particles fluxes, spectra and pitch-angular distributions, it is not possible to judge on the role of the solar coronal structures, and/or of CMEs in the production of SEPs. One has to consider also a potential influence of the flare shock wave(s), and/or of magnetic discontinuities that could exist quite near and very far from the Sun on the shape of the locally registered SEPs spectra.

**7.17.1. Brief description of the SKI-5 instrument.** SKI-5 includes three different types of solar charged particle spectrometers:

1. Spectrometer SPE to separately register protons and electrons in quite wide energy range: for protons from few to hundreds MeV in 8 to 10 energy bins; and for electrons from ≈150 keV to ≈10 MeV in 6 energy intervals;
2. Spectrometer SPEA to register alpha particles, ions of the C, N, O group, and ions of the Fe group in the energy range from a few MeV/nucleon up to a few 10 MeV/nucleon, divided in several energy channels;
3. Electrostatic spectrometer (SGMTD) to register energy and angular distributions separately for electrons and protons in the energy interval 6–40 keV, subdivided into 10 energy channels.

Spectrometers SPE and SPEA consist of the telescope units that are composed of semiconductor Si-detectors of different thickness. The spectrometer SPE also includes scintillation detector CsI. Detectors that belong to the same telescope are positioned along the common axes. Type of the detected particle is determined on the base of the known relation between

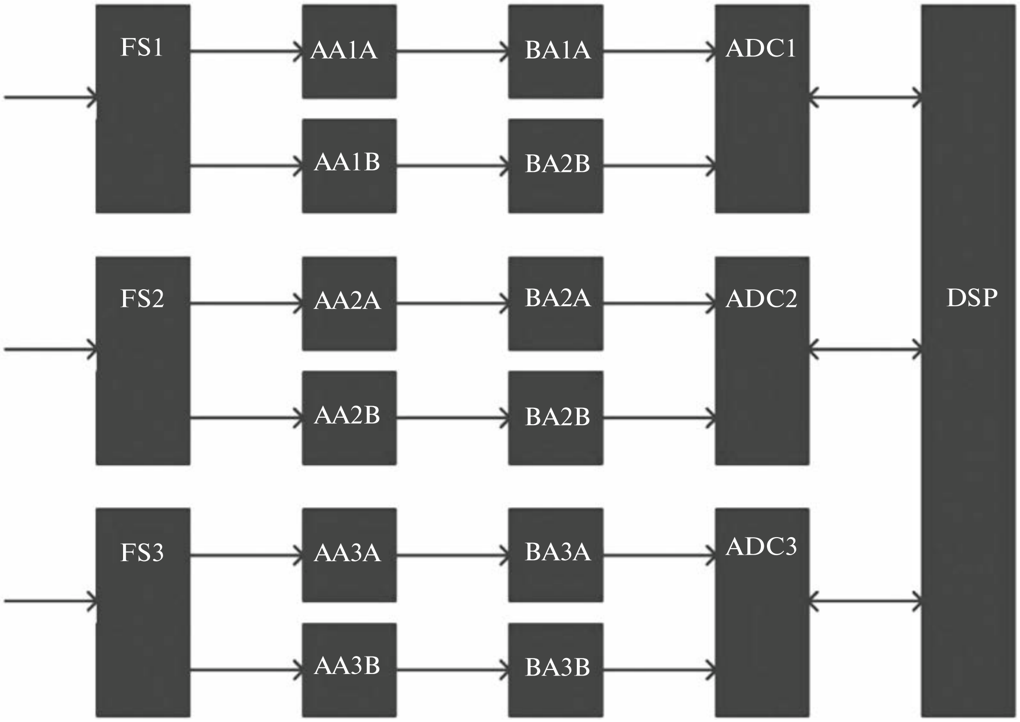

**Fig. 50.** Block diagram of the RSD receiver measuring channels.

**Fig. 51.** RSD receiver unit.

the particle energy and the ionization losses of the particle in the detector volume. Electronics unit is helping to register particles of different types by the setting different coincidence and anti-coincidence sequences for the specific type of registered particle.

Energy determination of the particle in the electrostatic spectrometer is made after the particle pass through the varying electrostatic filed.

Spectrometers SPE and SPEA are planned to have a field-of view of the conical shape with the full open angle of ≈35°. Both of each type spectrometers, SPE and SPEA, have two telescopes oriented in the opposite to each other directions. Telescope axes of SPE and SPEA are declined with respect to the line connecting satellite and the Sun by the angle of ≈30° in order to have spectrometer axes more or less coaligned with the Parker spiral of interplanetary magnetic field.

Field-of-view of SGMTD has a circular shape of 360° × 15°, where circumference of the FoV is subdi-

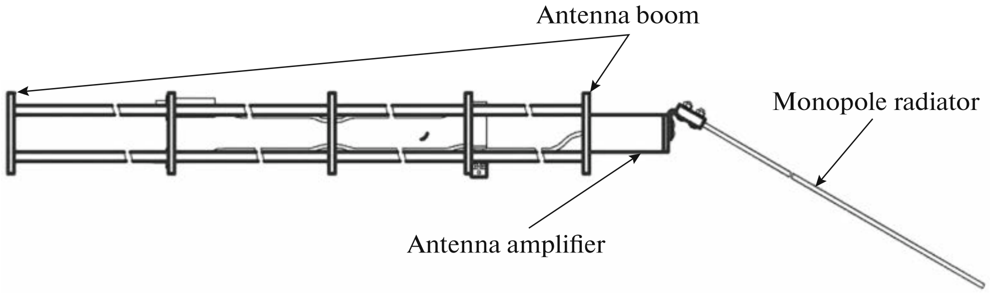

**Fig. 52.** Design of the antenna of each RSD channel.

vided into 6 equal size segments of 60°. In each of these segments independent registration of particles is planned. In a sense, one can speak about 6 independent spectrometers that independently register charged particles coming from 6 FoV segments with the 60° × 15° size.

It is planned to have two main modes of SKI-5 operation. Namely: (1) main regime, which is equivalent to monitoring of the relatively small fluxes of solar cosmic rays; and (2) regime of event, e.g. when a solar flare or CME happens. Change of the registration mode is made automatically after fluxes are exceeding preselected thresholds. After mode change the duration of the registered data collection is planned to be decreased by the order of magnitude.

### *7.18. Neutron Detector INTERSONG*

**7.18.1. Scientific objectives of the INTERSONG experiment.** Solar energetic particles (SEPs) can be accelerated in a few solar zones, like in an exploding arcs, at X-points of annihilating magnetic field lines, at shock waves, that are expanding from the corona into inner heliosphere. Large solar flares, those that can cause a radiation hazard at the Earth, or at the low earth orbits, can be a source of energetic particles accelerated in one, or many of the above mentioned

**Table 22.** Main characteristics of the RSD instrument

| Characteristics | Values |
|---|---|
| ***General*** | |
| Mass, kg | 2.5 ± 0.05 |
| Power consumption, W | 10 |
| Voltage, V | 27 ± 4 |
| Dimension, mm | 192 × 161 × 59 |
| ***Functional*** | |
| Number of channels | 3 |
| Frequency range, MHz | 0.015–300.0 |
| Threshold sensitivity, no less than, dBm/Hz | –160 |
| Spectrum resolution, kHz | 15 (from 15 kHz to 30 MHz)<br>30 (from 30 MHz to 150 MHz)<br>74 (from 150 MHz to 300 MHz) |
| Dynamic range without gain control, no less than, dB | 80 |
| Dynamic range of the gain control, no less than, dB | 120 |
| Maximum measuring frequency, Hz | 10 |
| ***Operational*** | |
| Discrete commands | None |
| TM/TC interface (RS-485), up to, Mb/sec | 1 |
| Internal memory buffer, Mb | 256 |

sites. At the same time, escape of the particles from the acceleration site can be delayed relatively to the acceleration time due to the particles capture on the closed magnetic loops, or because of the particle multiple scattering process on the turbulence produced at shock waves. Additionally, on their path to Earth, SEPs can be scattered by turbulence of interplanetary magnetic field (IMF).

Therefore, upon arriving to the Earth or LEO (low Earth orbit) SEPs, in many cases, have already lost their original time and energy distributions due to the influence of intermittent acceleration and diffusion along and perpendicular to the IMF direction. Only in situ measurements of SEPs, as close to the Sun as possible, leave us the chance to acquire original information about primary acceleration processes in the solar corona and about SEPs escape from there to the interplanetary medium.

Contrary to SEPs, transport of solar neutral emission, namely of gamma-rays and neutrons, is not dependent on the environment of the inner heliosphere. Registration time of neutral emission on the Earth orbit can be quite simply connected with the time and place of their generation during a solar flare, and consequently with the SEPs spectra and places of their generation.

This connection allows us a chance by solving the reverse problem to restore parameters of the primary solar particles as well as parameters of local solar plasma, where neutrons, or gamma-photons were generated in a solar flare. Fluxes of solar neutrons can be followed also by studying light curves (LCs) of solar gamma-ray line emission at 2.223 and 0.511 MeV (e.g., (Morrison, 1958; Lingenfelter and Ramaty, 1967; Share et al., 1982)). Solar gamma-ray line 2.223 MeV is formed in a neutron capture process on nuclei of $^3$He and H with ≈100 seconds delay due to necessity for neutrons to slow down. Because of this delay the LC-method can be used to estimate neutron spectra with some limitations. Obviously, only detection of neutrons coming directly from the solar surface can provide us with the unique information on the spectra and temporal dependence of ion fluxes with energies ≤10 MeV/nucleon and 40–300 MeV/nucleon that were accelerated in a solar flare. To achieve this goal one will need to use a neutron telescope with good spectral, time and angular resolution, and with low noise level.

Of course, neutrons and gamma-rays generated by the solar activity can be detected on-board the near-Earth satellites (Chupp, 1988). Such experiments, for example, were carried out in the past by SINP MSU group on-board the Coronas-F space observatory (experiments SONG and SPR-N; (Kuznetsov et al., 2006)). But this past experience has taught us that it is extremely difficult to separate direct solar neutrons from secondary neutrons that can be generated in the material of a satellite and an instrument itself (Share et al., 2011).

Comparing with near-Earth orbiting satellites, experiments moving to the Sun will see higher fluxes of solar neutrons, or gamma-photons. Fluxes will generally increase proportionally to the squared ratio of distance from the Sun to the Earth ($L_{Earth}$) to distance from the Sun to a satellite ($L_{Sat}$), i.e. as $\sim(L_{Earth}/L_{Sat})^2$. Apart from the distance influence on detectable solar neutrons fluxes, it is known that neutron itself decays with the life-time of ≈887 s. This life-time is comparable with the travel time of solar fast neutron to the Earth orbiting satellite. This makes practically impossible to detect 10 MeV solar neutrons at the Earth orbit, but at the distances of ~0.3 AU from the Sun a large part of 10 MeV neutrons still survive decay, thus allowing for their detection.

**7.18.2. Brief description of the INTERSONG instrument.** An unambiguous detection of solar, and not secondary neutrons implies necessity to use a neutron telescope with directional capability. Such telescope to detect solar fast neutrons at energies from a few MeV up to 100 MeV with moderate energy and angular resolution was developed at SINP MSU. Additional restriction was applied that it has to be quite light-weighted, but with sufficient effective area to be able to monitor solar activity during the whole mission.

To register solar neutrons we developed the INTERSONG telescope, that uses an elastic scattering of neutrons on the hydrogen nuclei contained abundantly in scintillating material of fibers (Fig. 53). This method was proposed by Pinkau (1966). The telescope (Fig. 54) has three major detectors, namely: (1) a hodoscope composed of scintillating fibers aligned along X- and Y-axes in alternating layers; (2) a system of scintillating plastic flat counters viewed by photo-multipliers that are forming anti-coincidence system for the telescope; and (3) a calorimeter.

Figure 55 shows efficiency of detection of neutrons by the telescope depending on the neutron initial energy for the threshold energy of the secondary protons elastically scattered by incoming neutrons set at 5 MeV, and the neutron threshold energy of 10 MeV. To make the threshold energy of neutron detection lower one needs to lower a threshold energy for the scattered protons.

In this case the detection efficiency of neutrons is getting higher. We plan to get neutron detection threshold energy as low as 3 MeV. This can be made at the expense of worsening angular resolution for the telescope. But bearing in mind that the neutron source is well known, i.e. the Sun, this is not too bad. The efficiency shown in Fig. 55 is one of the results of the telescope simulation made in order to understand typical distributions of the energy deposition in scintillating fibers, interaction type distributions, etc. From analysis of simulated events we constructed also the trigger criteria for the fast neutrons and hard X-rays and gamma-photons detection by the instrument. From simulations we have learned that two characteristic interaction types can be used to restore incoming neutron spectrum and their origin. Namely, for the neutron energy of 10 MeV we found that majority of usable events have two elastic interactions in the fibers of the hodoscope, but quite a few events were also having one point of neutron scattering in the hodoscope and the second point in the calorimeter. The latter type of event is shown in Fig. 56.

For both types of events we have two sets of data, one for each point of interaction. Namely, we have coordinates, time and energy deposition for the first interaction, like ($x_1$, $y_1$, $z_1$, $t_1$, $E_1$) and ($x_2$, $y_2$, $z_2$, $t_2$, $E_2$). From these two sets of data one can get energy ($E_0$) of the primary incoming neutron and its direction, by using kinematics of elastic scattering and time of flight (see Figs. 53 and 56).

Two major sources of secondary neutrons have to be taken into account in order to derive the minimum detectable flux of solar neutrons on the orbit of the Interhelioprobe SC. Those are, first of all, the secondary neutrons produced by the galactic and solar cosmic rays in the constructing material of the satellite and instrument itself, and the second potential background neutron source is solar atmosphere albedo neutrons. The former background is suppressed by factor of 1 : 128 due to the selection of solid angle of the acceptable directions for incoming solar neutrons, and the latter was shown to be generally much smaller than the former one. The background suppression is not a trivial task and the solution of it will depend on the relative orientation of instrument, solar active region and of a magnetic field line. Considerations of possible time delays due to SEPs transit to the satellite orbit can be useful.

**7.18.3. Characteristics of the INTERSONG instrument.** Based on the results of numerical simulations and laboratory calibrations of the detectors planned to be used for the INTERSONG experiment, as well as using known results of neutron fluxes and spectra produced in few solar flares, we state that INTERSONG has the effective area $A_{\text{eff}} \approx 8$ cm$^2$ for single scatter events; ≈2 cm$^2$ for double-scatter events, the first being elastic scatter, for neutrons with energy ≈20 MeV, i.e. we will know direction of incoming neutron for ≥25% neutron detection events. With the proposed configuration of INTERSONG we can detect:

- 360 neutrons with energy $E_n = 10 \pm 5$ MeV, 365 neutrons with energy $E_n = 20 \pm 5$ MeV, and 30 neutrons with energy $E_n = 50 \pm 5$ MeV, at the radial distance of 0.3 AU from the Sun in a solar event like the flare of October 28, 2003, if the neutron spectrum on the solar surface was $dN/dE = (3.3 \pm 0.3) \times 10^{27} (E_n/100)^{-\alpha}$ MeV$^{-1}$ ster$^{-1}$, with a power law index $\alpha = 3.5^{+0.4}_{-0.2}$.

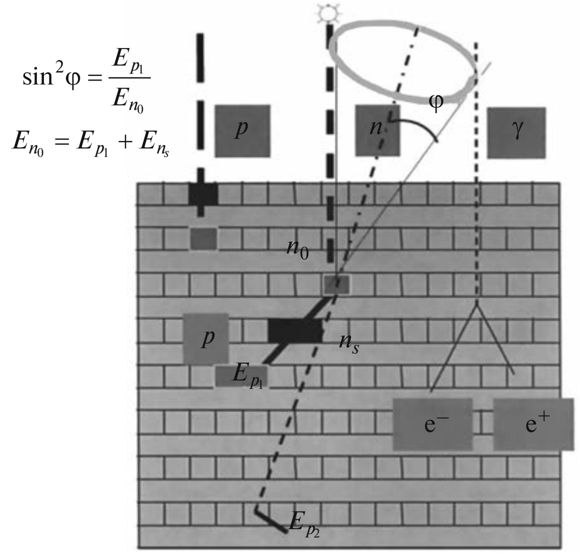

**Fig. 53.** Principle of fast neutrons registration via their elastic scattering on hydrogen.

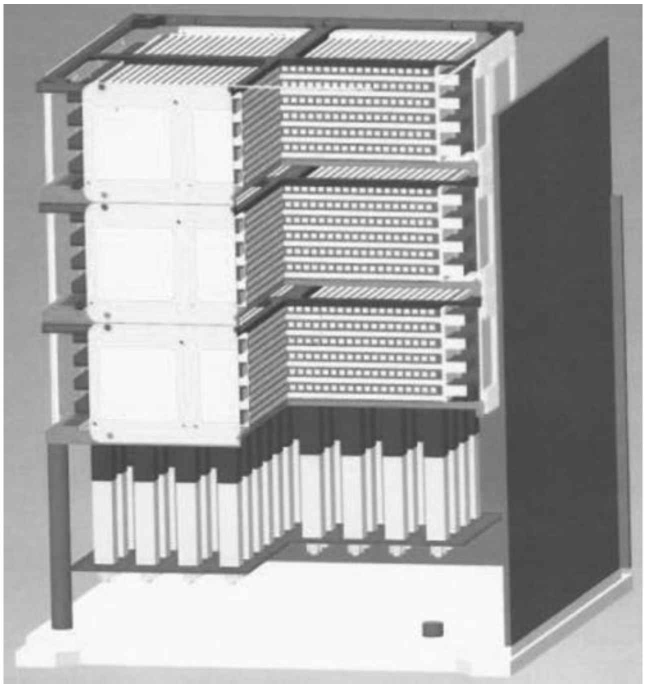

**Fig. 54.** Cross-cut view of the INTERSONG, which shows three layers of the scintillating fiber modules viewed from the side by the Si-PM arrays. Below them a calorimeter is shown with each pixel (dark grey) being viewed by the photomultiplier, shown in white. Scintillating counters of the anti-coincidence system are not shown.

- 440 neutrons with energy of $E = 20 \pm 5$ MeV, for the distance of 0.3 AU from the Sun, for the solar flare of November 04, 2003 type.

*General characteristics of the INTERSONG instrument are*: mass <10 kg, size 250 × 250 × 350 mm$^3$,

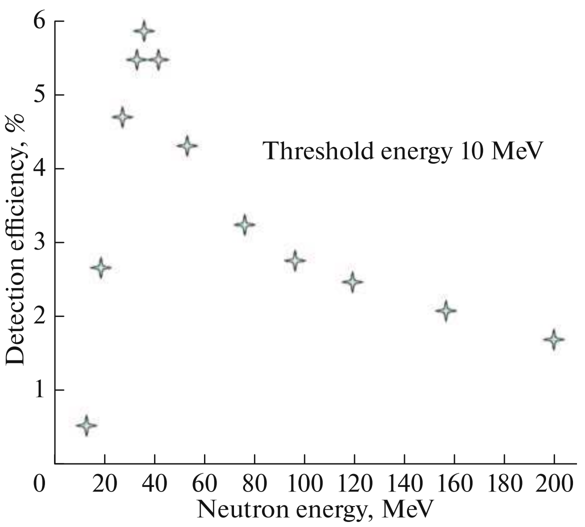

**Fig. 55.** Registration efficiency of the fast neutrons by the INTERSONG.

15 W of power consumption, and approximately 100 Mb/day of data generation.

## 8. SCIENTIFIC COOPERATION WITH OTHER SOLAR AND HELIOSPHERIC PROJECTS

Undoubtedly, scientific output of the Interhelioprobe mission will be significantly increased in case, if some special joint observational programs with other space and ground based solar observatories will be organized. Remote sense observations of the Sun and local measurements in the inner heliosphere simultaneously in several points with different heliocentric distances and helio-longitudes (latitudes) will be very useful to achieve the scientific goals of the mission (Section 3) more deeply and reliably. In particular, this will allow to:

—measure "solar constant" at different heliolongitudes and latitudes;

—produce detailed photospheric magnetograms for more reliable reconstructions of magnetic field in the entire corona;

—make stereoscopic observations of quasi-stationary coronal magnetic structures in the white-light, EUV and soft X-ray ranges;

—make stereoscopic observations of solar flare hard X-ray sources;

—investigate directivity of solar flare hard X-ray emission;

—make 3D reconstructions of CMEs in the EUV and white-light wave ranges;

—investigate 3D structure of interplanetary magnetic clouds and shock waves;

—implement radio direction-finding capabilities for studying acceleration and propagation of electrons in the inner heliosphere;

—measure energetic charged particles in different points for studying their acceleration and transport processes in the solar corona and inner heliosphere.

It is expected that Interhelioprobe will start to perform its scientific program after 2026. During this time at least a few space solar observatories will probably operate at the Earth's orbit. Also, there will be several

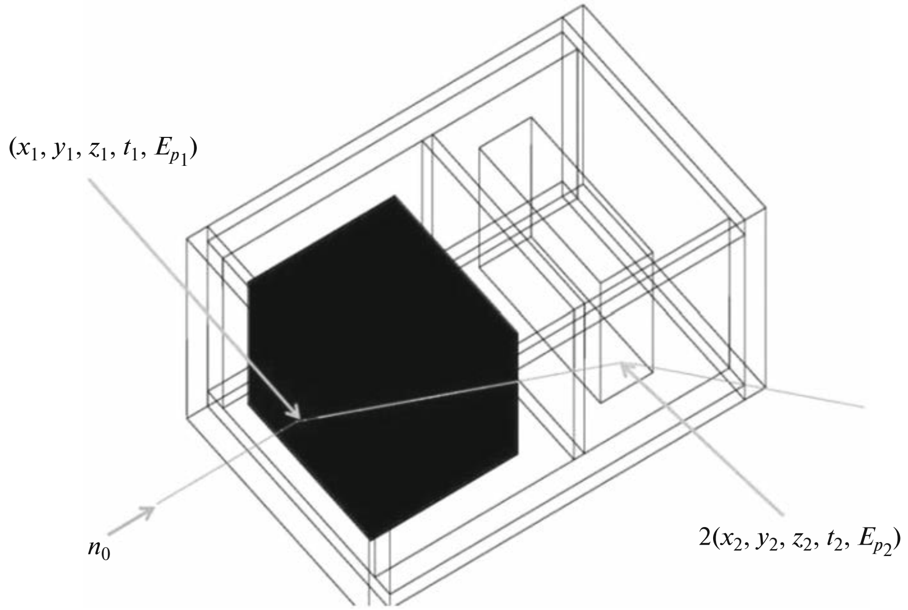

**Fig. 56.** One of the types of neutron interaction events with the matter of telescope, where first (elastic) interaction takes place in the hodoscope, and the second interaction in the calorimeter.

new or upgraded optical and radio solar facilities on the ground. This will be good opportunity to make joint observations mentioned above and even more. However, planning of concrete scientific observational programs, in particular, in the framework of the International Living With a Star (ILWS) program, can be made after the final orbits of the Interhelioprobe mission will be fixed.

## ACKNOWLEDGMENTS

In 2009–2015 the Interhelioprobe project works have been done in frames of the Federal Space Program 2006–2015 of the Russian Federation. In 2016–2025 the Interhelioprobe project works are carried on in frames of the Federal Space Program 2016–2025 of the Russian Federation.

We acknowledge support from the Polish National Science Centre grants: 2011/01/M/ST9/05878, 2011/01/B/ST9/05861, 4 T12E 045 29, 2011/01/M/ST9/06096, 2314/7.PR/2012/2 and the European Commission grant FP7/2007-2013: eHEROES, Project No. 284461. The CHIANTI atomic database and code is a collaborative project involving George Mason University, University of Michigan (USA) and University of Cambridge.

## REFERENCES

Acton, L.W., Finch, M.L., Gilbreth, C.W., et al., The soft X-ray polychromator for the Solar Maximum Mission, *Sol. Phys.*, 1980, vol. 65, pp. 53–71.

Akita, K., Tanaka, K., Watanabe, T., et al., Solar flare soft X-ray spectra from the Hinotori. 1: Iron line spectra and their time variations of seven X-class flares, *Ann. Tokyo Astron. Obs.*, 1982, vol. 18, no. 4, pp. 237–338.

Alexandrova, O., Saur, J., Lacombe, C., et al., Universality of solar-wind turbulent spectrum from MHD to electron scales, *Phys. Rev. Lett.*, 2009, vol. 103, no. 16, id 165003.

Antia, H.M. and Basu, S., Determining solar abundances using helioseismology, *Astrophys. J.*, 2006, vol. 644, no. 2, pp. 1292–1298.

Aptekar, R.L., Frederiks, D.D., Golenetskii, S.V., et al., Konus-W gamma-ray burst experiment for the GGS wind spacecraft, *Space Sci. Rev.*, 1995, vol. 71, nos. 1–4, pp. 265–272.

Aptekar, R.L., Golenetskii, S.V., Mazets, E.P., et al., Cosmic gamma-ray bursts and gamma repeaters studies with Ioffe institute Konus experiments, *Phys.-Usp.*, 2010, vol. 53, no. 4, pp. 401–405.

Arghavani, M.R., Russell, C.T., Luhmann, J.G., et al., Interplanetary magnetic field enhancements in the solar wind: Statistical properties at 1 AU, *Icarus*, 1985, vol. 62, pp. 230–243.

Auster, H.U., Apathy, I., Berghofer, G., et al., ROMAP: Rosetta magnetometer and plasma monitor onboard the Rosetta lander, in *ROSETTA: ESA's Mission to the Origin of the Solar System*, Schulz, R., Alexander, C., Boehnhardt, H., and Glaßmeier, K.-H., Eds., New York: Springer, 2009, pp. 701–719. doi 10.1007/978-0-387-77518-0_19_8

Bougeret, J.-L., Kaiser, M.L., Kellogg, P.J., et al., Waves: The radio and plasma wave investigation on the wind spacecraft, *Space Sci. Rev.*, 1995, vol. 71, nos. 1–4, pp. 231–263.

Bougeret, J.-L., Goetz, K., Kaiser, M.L., et al., S/WAVES: The radio and plasma wave investigation on the stereo mission, *Space Sci. Rev.*, 2008, vol. 136, nos. 1–4, pp. 487–527.

Brueckner, G.E., Howard, R.A., Koomen, M.J., et al., The large angle spectroscopic coronagraph (LASCO), *Sol. Phys.*, 1995, vol. 162, nos. 1–2, pp. 357–402.

Cairns, I.H., Coherent radio emissions associated with solar system shocks, in *The Sun, the Solar Wind, and the Heliosphere,* Miralles, M.P. and Sánchez Almeida, J., Eds., Berlin: Springer, 2009, pp. 267–338.

Carlson, C.W. and McFadden, J.P., Design and application of imaging plasma instruments, in *Measurements Techniques in Space Plasmas: Particles*, Pfaff, R.F., Borovsky, J.E., and Young, D.S., Eds., Washington, DC: AGU, 1998, pp. 125–140.

Chernov, G.P., Unusual absorption and emission bands in solar radio bursts: Ropes of fiber in the metric range, *Astron. Lett.*, 2008, vol. 34, no. 7, pp. 486–499.

Chernov, G.P., Kaiser, M.L., Bougeret, J.-L., et al., Fine structure of solar radio bursts observed at decametric and hectometric waves, *Sol. Phys.*, 2007, vol. 241, no. 1, pp. 145–169.

Chupp, E.L., Solar neutron observations and their relation to solar flare acceleration problems, *Sol. Phys.*, 1988, vol. 118, no. 1, pp. 137–154.

Culhane, J.L., Hiei, E., Doschek, G.A., et al., The Bragg crystal spectrometer for Solar-A, *Sol. Phys.*, 1991, vol. 136, no. 1, pp. 89–104.

Doschek, G.A., Solar instruments on the P78-1 spacecraft, *Sol. Phys.*, 1983, vol. 86, no. 1, pp. 9–17.

Elokhin, A.P., Safonenko, V.A., Ulin, S.E., et al., The use of unmanned dose of the complex to determine the concentration pa-radionuclides in the atmosphere in terms of radiation accidents, *Nucl. Meas. Inf. Technol.*, 2007, no. 3, pp. 42–59.

Ermolli, I. and Matthes, K., Dudok de Wit, T., et al., Recent variability of the solar spectral irradiance and its impact on climate modeling, *Atmos. Chem. Phys. Discuss.*, 2012, vol. 12, pp. 24557–24642.

Eyles, C.J., Harrison, R.A., Davis, C.J., et al., The heliospheric imagers onboard the stereo mission, *Sol. Phys.*, 2009, vol. 254, no. 2, pp. 387–445.

Fitzenreiter, R.J., Fainberg, J., Weber, R.R., et al., Radio observations of interplanetary magnetic field structures out of the ecliptic, *Sol. Phys.*, 1977, vol. 52, pp. 477–484.

Fröhlich, C., Andersen, B.N., Appourchaux, T., et al., First results from VIRGO the experiment for helioseismology and solar irradiance monitoring on SOHO, *Sol. Phys.*, 1997, vol. 170, no. 1, pp. 1–25.

Glassmeier, K.-H., Auster, H.-U., Heyner, D., et al., The fluxgate magnetometer of the BepiColombo Mercury Planetary Orbiter, *Planet. Space Sci.*, 2010, vol. 58, nos. 1–2, pp. 287–299.

Gringauz, K.I., Bezrukikh, V.V., Ozerov, V.D., et al., A Study of the interplanetary ionized gas, high-energy electrons and corpuscular radiation from the Sun by means of the three-electrode trap for charged particles on the second Soviet cosmic rocket, *Sov. Phys.-Dokl.*, 1960, vol. 5, pp. 361–364.

Grün, E., Krüger, H., and Landgraf, M., Cosmic dust, in *The Heliosphere Near Solar Minimum. The Ulysses Perspective*, Balogh, A., Marsden, R.G., and Smith, E.J., Eds., London: Springer, 2001, pp. 373–404.

Horbury, T.S., Forman, M.A., Oughton, S., Spacecraft observations of solar wind turbulence: An overview, *Plasma Phys. Controlled Fusion*, 2005, vol. 47, no. 12B, pp. B703–B717.

Howard, R.A., Moses, J.D., Vourlidas, A., et al., Sun Earth Connection Coronal and Heliospheric Investigation (SECCHI), *Space Sci. Rev.*, 2008, vol. 136, nos. 1–4, pp. 67–115.

Hurford, G.J., Schmahl, E.J., Schwartz, R.A., et al., The RHESSI imaging concept, *Sol. Phys.*, 2002, vol. 210, pp. 61–86.

Kahler, S.W., Cliver, E.W., and Cane, H.V., Shock-associated kilometric radio emission and solar metric type II bursts, *Sol. Phys.*, 1989, vol. 120, no. 2, pp. 393–405.

Kaiser, M.L., The STEREO mission: An overview, *Adv. Space Res.*, 2005, vol. 36, no. 8, pp. 1483–1488.

Korepanov, V. and Marusenkov, A., Flux-gate magnetometers design peculiarities, *Surv. Geophys.*, 2012, vol. 33, no. 5, pp. 1059–1079.

Korepanov, V. and Pronenko, V., Induction magnetometers-design peculiarities, *Sens. Transducers J.*, 2010, vol. 120, no. 9, pp. 92–106.

Kosugi, T., Makishima, K., Murakami, T., et al., The hard X-ray telescope (HXT) for the SOLAR-A mission, *Sol. Phys.*, 1991, vol. 136, pp. 17–36.

Kotov, Yu.D., High-energy solar flare processes and their investigation onboard Russian satellite missions CORONAS, *Phys.-Usp.*, 2010, vol. 53, no. 6, pp. 619–631.

Kuznetsov, V.D., Solar and heliophysics space missions, *Adv. Space Res.*, 2015, vol. 55, no. 3, pp. 879–885.

Kuznetsov, S.N., Kurt, V.G., Myagkova, I.N., et al., Gamma-ray emission and neutrons from solar flares detected by the SONG instrument in 2001–2004, *Sol. Syst. Res.*, 2006, vol. 40, no. 2, pp. 104–110.

Laming, J.M., Non-WKB models of the First Ionization Potential effect: Implications for solar coronal heating and the coronal helium and neon abundances, *Astrophys. J.*, 2009, vol. 695, no. 2, pp. 954–969.

Leamon, R.J., Smith, C.W., Ness, N.F., et al., Observational constraints on the dynamics of the interplanetary magnetic field dissipation range, *J. Geophys. Res.*, 1998, vol. 103, no. A3, pp. 4775–4787.

Leblanc, Y., Dulk, G.A., and Bougeret, J.-L., Tracing the electron density from the corona to 1au, *Sol. Phys.*, 1998, vol. 183, no. 1, pp. 165–180.

Limousin, O., Lugiez, F., Gevin, O., et al., Caliste 256: A CdTe imaging spectrometer for space science with a 580 μm pixel pitch, *Nucl. Instrum. Methods Phys. Res., Sect. A*, 2011, vol. 647, no. 1, pp. 46–54.

Lin, R.P., Dennis, B.R., Hurford, G.J., et al., The Reuven Ramaty High-Energy Solar Spectroscopic Imager (RHESSI), *Sol. Phys.*, 2002, vol. 210, pp 3–32.

Lingenfelter, R.E. and Ramaty, R., High energy nuclear reactions in solar flares, in *High-Energy Nuclear Reactions in Astrophysics—A Collection of Articles*, Shen, B.S.P., Ed., New York: Benjamin, 1967, p. 99.

Mazets, E.P., Aptekar, R.L., Golenetskii, S.V., et al., Studies of cosmic gamma-ray bursts and soft gamma repeaters in the Russian–American Konus-Wind experiment, *JETP Lett.*, 2012, vol. 96, no. 8, pp. 544–553.

Mazets, E.P., Aptekar, R.L., Golenetskii, S.V., et al., Study of solar flares and gamma-ray bursts in the Helicon experiment, in *The Coronas-F Space Mission*, Kuznetsov, V., Ed., Springer, 2014, pp. 393–403.

Michalowska, A., Gevin, O., Lemaire, O., et al., IDeF-X HD: A low power multi-gain CMOS ASIC for the readout of Cd(Zn)Te detectors, in *IEEE Nuclear Science Symposium and Medical Imaging Conference*, 2010, pp. 1556–1559.

Morrison, P., On gamma-ray astronomy, *Nuovo Cim.*, 1958, vol. 7, no. 6, pp. 858–865.

Mueller, D., Marsden, R.G., St. Cyr, O.C., Gilbert, H.R., and the Solar Orbiter Team, Solar orbiter: Exploring the Sun–Heliosphere connections, *Sol. Phys.*, 2013, vol. 285, nos. 1–2, pp. 25–70.

Oraevsky, V.N., Galeev, A.A., Kuznetsov, V.D., and Zelenyi, L.M., Solar Orbiter and Russian Aviation and Space Agency Interhelioprobe, in *Solar Encounter. Proceedings of the First Solar Orbiter Workshop, 14–18 May 2001, Puerto de la Cruz, Tenerife, Spain*, Battrick, B. and Sawaya-Lacoste, H., Eds., Noordwijk: ESA, 2001, pp. 95–108.

Owocki, S.P., Holzer, T.E., and Hundhausen, A.J., The solar wind ionization state as a coronal temperature diagnostic, *Astrophys. J.*, 1983, vol. 275, pp. 354–366.

Petrosyan, A., Balogh, A., Goldstein, M.L., et al., Turbulence in the solar atmosphere and solar wind, *Space. Sci. Rev.*, 2010, vol. 156, nos. 1–4, pp. 135–238.

Pick, M. and Vilmer, N., Sixty-five years of solar radioastronomy: Flares, coronal mass ejections and Sun–Earth connection, *Astron. Astrophys. Rev*, 2008, vol. 16, pp. 1–153.

Pinkau, K., Die Messung solarer und atmosphärischer Neutronen, *Z. Naturforsch., A: Phys. Sci.*, 1966, vol. 21, no. 12, pp. 2100–2101.

Reiner, M., Kilometric type III radio bursts, electron beams, and interplanetary density structures, *Space Sci. Rev.*, 2001, vol. 97, no. 1, pp. 129–139.

Reiner, M.J., Kaiser, M.L., Fainberg, J., and Stone, R.G., A new method for studying remote type II radio emissions from coronal mass ejection-driven shocks, *J. Geophys. Res.*, 1998, vol. 103, no. A12, pp. 29651–29664.

Reiner, M.J., Fainberg, J., Kaiser, M.L., and Bougeret, J.-L., A highly circularly polarized solar radio emission component observed at hectometric wavelengths, *Sol. Phys.*, 2006, vol. 234, no. 2, pp. 301–324.

Rème, H., Aoustin, C., Bosqued, J.M., et al., First multispacecraft ion measurements in and near the Earth's magnetosphere with the identical Cluster Ion Spectrometry (CIS) experiment, *Ann. Geophys.*, 2001, vol. 19, no. 10, pp. 1303–1354.

Reva, A., Ulyanov, A., Bogachev, S., and Kuzin, S., Initiation and early evolution of the coronal mass ejection on 2009 May 13 from extreme-ultraviolet and white-light observations, *Astrophys. J.*, 2014, vol. 793, no. 2, id 140.

Rice, J.E., Reinke, M.L., Ashbourn, J.M.A., et al., X-ray observations of Ca19$^+$, Ca18$^+$ and satellites from Alcator C-Mod tokamak plasmas, *J. Phys. B: At., Mol. Opt. Phys.*, 2014, vol. 47, no. 7, id 075701.

Russell, C.T. and Jian, L., Flows and obstacles in the solar wind, *Adv. Space Res.*, 2008, vol. 41, no. 8, 1177–1187.

Sauvaud, J.-A., Koperski, P., Beutier, T., et al., The INTERBALL-Tail ELECTRON experiment: Initial results on the low-latitude boundary layer of the dawn magnetosphere, *Ann. Geophys.*, 1997, vol. 15, no. 5, pp. 587–595.

Sauvaud, J.-A., Larson, D., Aoustin, C., et al., The IMPACT solar wind electron analyzer (SWEA), *Space Sci. Rev.*, 2008, vol. 136, pp. 227–239.

Schwenn, R. and Marsch, E., *Physics of the Inner Heliosphere. 1. Large-Scale Phenomena, Series: Physics and Chemistry in Space*, Vol. 20, Berlin: Springer, 1990.

Schwenn, R. and Marsch, E., *Physics of the Inner Heliosphere. 2. Particles, Waves and Turbulence, Series: Physics and Chemistry in Space*, Vol. 21, Berlin: Springer, 1991.

Serenelli, A.M., Basu, S., Ferguson, J.W., and Asplund, M., New solar composition: The problem with solar models revisited, *Astrophys. J.*, 2009, vol. 705, no. 2, pp. L123–L127.

Share, G.H., Nolan, P.L., Forrest, D.J., et al., Measurements of the 2.223 MeV neutron capture line in solar flares, *Bull. Am. Astron. Soc.*, 1982, vol. 14, p. 875.

Share, G.H., Murphy, R.J., Tylka, A.J., et al., Physics of solar neutron production: Questionable detection of neutrons from the 31 December 2007 flare, *J. Geophys. Res.*, 2011, vol. 116, A03102.

Siarkowski, M., Sylwester, J., Bakala, J., et al., ChemiX: A Bragg crystal spectrometer for the Interhelioprobe interplanetary mission, *Exp. Astron.*, 2016, vol. 41, no. 3, pp. 327–350.

Smirnov, V., Vaisberg, O., and Anisimov, S., An attempt to evaluate the structure of cometary dust particles, *Astron. Astrophys.*, 1987, vol. 187, pp. 774–778.

Sperverlage, K., Neubauer, F.M., Baumgärtel, K., et al., Magnetic holes in the solar wind between 0.34 AU and 17 AU, *Nonlinear Processes Geophys.*, 2000, vol. 7, pp. 191–200.

Srama, R., Altobelli, N., de Kam, J., et al., DUNE-eXpress dust astronomy with ConeXpress, *Adv. Space Res.*, 2006, vol. 38, no. 9, pp. 2093–2101.

Sylwester, J., Gaicki, I., Kowalinski, M., et al., Resik: A bent crystal X-ray spectrometer for studies of solar coronal plasma composition, *Sol. Phys.*, 2005, vol. 226, no. 1, pp. 45–72.

Sylwester, J., Kordylewski, Z., Plocieniak, S., et al., X-ray flare spectra from the DIOGENESS spectrometer and its concept applied to ChemiX on the Interhelioprobe spacecraft, *Sol. Phys.*, 2015, vol. 290, no. 12, pp. 3683–3697.

Šafránková, J., Zastenker, G., Němeček, Z., et al., Small scale observation of magnetopause motion: Preliminary results of the INTERBALL project, *Ann. Geophys.*, 1997, vol. 15, no. 5, pp. 562–569.

Šafránková, J., Němeček, Z., Přech, L., et al., Fast Solar Wind Monitor (BMSW): Description and first results, *Space Sci. Rev.*, 2013, vol. 175, no. 1, pp. 165–182.

Testa, P., Element abundances in X-ray emitting plasmas in stars, *Space Sci. Rev.*, 2010, vol. 157, nos. 1–4, pp. 37–55.

Tsuneta, S., Ichimoto, K., Katsukawa, Y., et al., The solar optical telescope for the Hinode mission: An overview, *Sol. Phys.*, 2008, vol. 249, pp. 167–196.

Ulin, S.E., Dmitrenko, V.V., Grachev, V.M., et al., Gamma detectors based on high pressure xenon: Their development and application, in *Hard X-Ray and Gamma-Ray Detectors Physics VI. Proc. SPIE*-5540, 2004, pp. 248–256.

Vaisberg, O.L., Gorn L.S., Ermolaev, Yu.I., et al., Experiment on the diagnostics of interplanetary and magnetospheric plasmas via the *Venera 11* and *Venera 12* probes and the *Prognoz 7* satellite, *Kosm. Issled.*, 1979, vol. 17, no. 5, pp. 780–792.

Vaisberg, O., Smirnov, V., Omelchenko, A., et al., Spatial and mass distribution of low-mass dust particles ($m < 10^{-10}$ g) in comet P/Halley's coma, *Astron. Astrophys.*, 1987, vol. 187, pp. 753–760.

Vasylinuas, V.M., Deep space plasma measurements, in *Methods of Experimental Physics*, Griem, H.R. and Lovberg, R.H., Eds., New York: Academic, 1971, vol. 9, part B, pp. 49–88.

Verigin, M.I., Remizov, A.P., Kotova, G.A., et al., Exploration of the solar wind by HELION experiment of Interhelioprobe mission, in *Interhelioprobe Project, Workshop Proceedings, Tarusa, 11–13 May 2011*, Kuznetsov, V.D., Ed., Moscow, 2012, pp. 132–138.

Vlasik, K.F., Grachev, V.M., Dmitrenko, V.V., et al., The automated system based on xenon gamma-spectrometers for monitoring of gaseous radioactive emissions of a nuclear reactor, *Nucl. Meas. Inf. Technol.*, 2004, vol. 2, pp. 45–53.

Zastenker, G.N., Ermolaev, Yu.I., Pintér, Š., et al., Observations of the solar wind with high temporal resolution, *Kosm. Issled.*, 1982, vol. 20, no. 6, pp. 900–906.

Zertsalov, A.A., Vaisberg, O.L., and Temnyi, V.V., Characteristics of the proton and alpha-particle components of the solar wind following the passage of interplanetary shock waves from observations on the *Prognoz* satellite on May 15 and 30, 1972, *Kosm. Issled.*, 1976, vol. 14, no. 2, pp. 234–240.

Zhang, J., Dere, K.P., Howard, R.A., Kundu, M.R., and White, S.M., On the temporal relationship between coronal mass ejections and flares, *Astrophys. J.*, 2001, vol. 559, no. 1, pp. 452–462.

Zhugzhda, Yu.D., Analytical signal as a tool for studying solar p-modes, *Astron. Lett.*, 2006, vol. 32, no. 5, pp. 329–343.

Zhugzhda, Yu.D. and Lebedev, N.I., Darkening and visibility functions for the global five-minute oscillations, *Astron. Lett.*, 2009, vol. 35, no. 7, pp. 547–560.

Zhugzhda, Yu.D., Kuznetsov, V.D., and Lebedev, N.I., Brightness fluctuations and global oscillations of the Sun (DIFOS experiment), in *The CORONAS-F Space Mission*, Kuznetsov, V., Ed., Springer, 2014, pp. 27–54.